Summer 8-15-2022

Soft Electronics and Sensors for Wearable Healthcare Applications

Li-Wei Lo
Washington University in St. Louis

WASHINGTON UNIVERSITY IN ST. LOUIS

McKelvey School of Engineering
The Institute of Materials Science & Engineering

Dissertation Examination Committee:
Chuan Wang, Chair
Shantanu Chakrabartty
Julio M. D'Arcy
Srikanth Singamaneni
Yong Wang

Soft Electronics and Sensors for Wearable Healthcare Applications

by
Li-Wei Lo

A dissertation presented to
the McKelvey School of Engineering of
Washington University in
partial fulfillment of the
requirements for the degree
of Doctor of Philosophy

August 2022
St. Louis, Missouri

Table of Contents

List of Figures

List of Tables

Acknowledgments

A heartfelt thanks to the many people who contributed and helped along this journey. Studying for a doctorate in the United States is not an easy task for foreigners. I still remember the drive from upstate New York to St. Louis, it was exciting but nervous. It's hard to believe how quickly the past few years have passed. Throughout this journey, I would like to thank my advisor Dr. Chuan Wang for his support and mentorship. His kindness, wisdom and diligent have influenced me to become a better scientist. And, I want to acknowledge the research committee members Dr. Shantanu Chakrabartty, Dr. Julio D'Arcy, Dr. Srikanth Singamaneni and Dr. Yong Wang (in alphabetical order of last name) for their guidance, feedback and supports.

Besides, I would like to thank all the collaborators including Dr. Shantanu Chakrabartty, Dr. Yong Wang, Dr. Xiaobo Tan, Dr. Kenji Aono, Dr. Zichao Wen, Hongyang Shi, Weilun Li, and Stephanie Pizzella for their guidance and funding supports. Thank all the staff from IMSE and MEMS Shared Instrument Group including Dr. Tyrone L. Daulton, Beth Gartin, Dr. Huafang Li and Barbara Semar.

Also, thanks to all the labmates including Dr. Haochuan Wan, Zhihao Xu, Junyi Zhao for their idea sharing and discussion. Special thanks to all the friends I met here at WashU including

Huifeng Zhu, Igor Luzhansky, Kaitlyn Broz and StLucas Vasileiou for their supportive friendship.

Last but not least, I would like to thank my parents for their endless love and my girlfriend for her support and encouragement throughout my years at WashU. I will face all the challenges of the future life with their unconditional love and encouragement.

Li-Wei Lo

Washington University in St. Louis
August 2022

Dedicated to my family and friends.

ABSTRACT OF THE DISSERTATION

Soft Electronics and Sensors for Wearable Healthcare Applications

by

Li-Wei Lo

Doctor of Philosophy in Materials Science and Engineering

Washington University in St. Louis, 2022

Professor Chuan Wang, Chair

Wearable electronics are becoming increasingly essential to personalized medicine by collecting and analyzing massive amounts of biological signals from internal organs, muscles, and blood vessels. Conventional rigid electronics may lead to motion artifacts and errors in collected data due to the mismatches in mechanical properties between human skin. Instead, soft wearable electronics provide a better platform and interface that can form intimate contact and conformably adapt to human skin. In this respect, this thesis focuses on new materials formulation, fabrication, characterization of low-cost, high sensitivity and reliable sensors for wearable health monitoring applications.

More specifically, we have studied the silver nanoparticles (AgNPs) inkjet-printed on a polydimethylsiloxane (PDMS) substrate that offers great pressure sensitivity for aterial pulse monitoring. In addition, we have investigated the conducting polymer poly(3,4-ethylenedioxythiophene) polystyrene sulfonate (PEDOT:PSS) and poly(ethylene oxide) PEO polymer blends that exhibit low sheet resistance and can resist up to 50% of tensile strain. The highly stretchable thin film can serve as interconnects between electronic components and dry electrodes for photoplethysmography (PPG) and electrocardiography (ECG) recordings. Based on the developed PEDOT:PSS solution with high conductivity, we fabricated a porous PDMS sponge coated with conductive PEDOT:PSS to make electrodes with reduced

electrode-skin contact impedance, improved signal-to-noise ratio and is suited for long-term and motion-artifact-tolerant recording of high quality biopotential signals including ECG and electromyography (EMG). Finally, we demonstrated a multimodal sensor based on the porous PEDOT:PSS/PDMS sponge for sensing and distinguishing of pressure, strain and temperature from different trends in resistance and capacitance response. Applications including object detection, gesture recognition and temperature sensing have all been demonstrated. In this thesis, the proposed materials, sensor design, low-cost inkjet printing and dip-coating fabrication process open the possibility for more complex epidermal wearable health monitoring electronic systems.

Chapter 1

Background

1.1 Introduction to Stretchable Electronics

In the past decade, stretchable electronics such as display, batteries, sensors for variety of human health monitoring have been explored extensively.[1–5] Stretchable electronics can not only bend, but also conform to human skin or be mechanically compatible with curved objects without device failure. With its superior mechanical properties, it has a wider range of applications than conventional rigid electronics, especially in creating better interfaces between the human body and machines. The main challenges in developing stretchable electronics involve new material synthesis, device design, mechanical design, system integration and fabrication, which are often different from conventional silicon-based electronics on the market. In this chapter, we detail strategies for developing stretchable materials, one of which is to synthesize functional or composite materials with intrinsic stretchability, and the other is to engineer materials into different structural shapes that can withstand strain. The following subsection then details the fabrication process for making stretchable electronics in low-cost

manufacturing processes and the practical applications of stretchable electronics. In this chapter, we detail strategies for developing stretchable materials, discuss the fabrication of stretchable sensors, and applications in stretchable electronics.

1.2 Materials and Structure Design for Stretchable Electronics

Two successful strategies for making materials elastic are to synthesize functional or composite materials with intrinsic stretchability and to engineer materials into different structural shapes that can withstand strain. Routes to synthesize new materials offer possibilities based on molecular design but face more challenges in large-scale fabrication processes, while structural design focuses on material mechanics that can be applied to rigid metals without much modification on the established fabrication processes. The following sections detail the methodology for developing stretchable materials.

1.2.1 Materials Design for Stretchable Electronics

The development of intrinsically stretchable electronics can be accomplished by molecular engineering, synthesizing stretchable materials, or formulating stretchable composites. For example, liquid metals exhibit infinite stretchability and high electrical conductivity ($\sigma = 3.4 \times 10^4$ S/cm) at room temperature.[6] Low-toxicity liquid metal eutectic gallium indium (EGaIn) alloy is a liquid at room temperature which can flow freely and retain the properties of a metal when stretched. Injecting liquid metal into thermoplastic elastomer poly(styrene-b-(ethylene-co-butene)-b-styrene) (SEBS) hollow fibers can maintain electrical continuity greater than 700% of strain.[7] Various liquid metal patterning techniques have been demonstrated in high

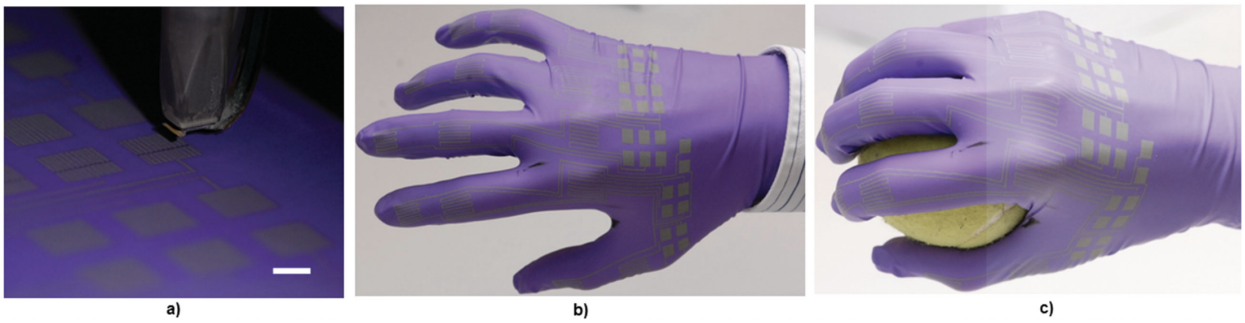

Figure 1.1: Inkjet printing of EGaIn nanoparticles (EGaInNPs). (a) Photograph of inkjet system printing EGaInNP dispersion. Scale bar is 5 mm in length. (b) Human hand wearing inkjet functionalized nitrile glove with arrays of strain gauges, intricate wiring, and contact pads comprised of EGaInNPs. (c) Same hand holding a tennis ball, demonstrating stretchability of the electronics. Reprinted from Ref.[8].

resolution inkjet-printing[8](Figure 1.1) and 3D-printing[9], allowing large scale fabrication for stretchable interconnects.

Metal nanowires offers stretchability due to their high aspect ratio and the percolation network maintaining electrical continuity under strain. Taking silver nanowires (AgNWs) as an example, silver is one of the ductile metals that can accommodate tensile stress, and its percolation network can also adapt to deformation, maintaining the conduction path of electrons under large strain. The researchers also showed that the long AgNWs network has superior electrical and mechanical properties than the short AgNWs network, in which the long AgNWs network with nanowires over 500 μm in length and 100-150 nm in diameter could be stretched to more than 460% without a significant increase in resistance as shown in Figure 1.2.[10]

Stretchable composites are the most actively researched approach today, incorporating additives into the conductive polymer poly(3,4-ethylenedioxythiophene)polystyrenesulfonate (PEDOT:PSS). Although intrinsic PEDOT and PSS are semi-crystalline structures with limited stretchability, the addition of plasticizers, ionic salt or soft polymers can improve their mechanical properties. As an example, the incorporation of Zonyl fluorosurfactant (FS-300)

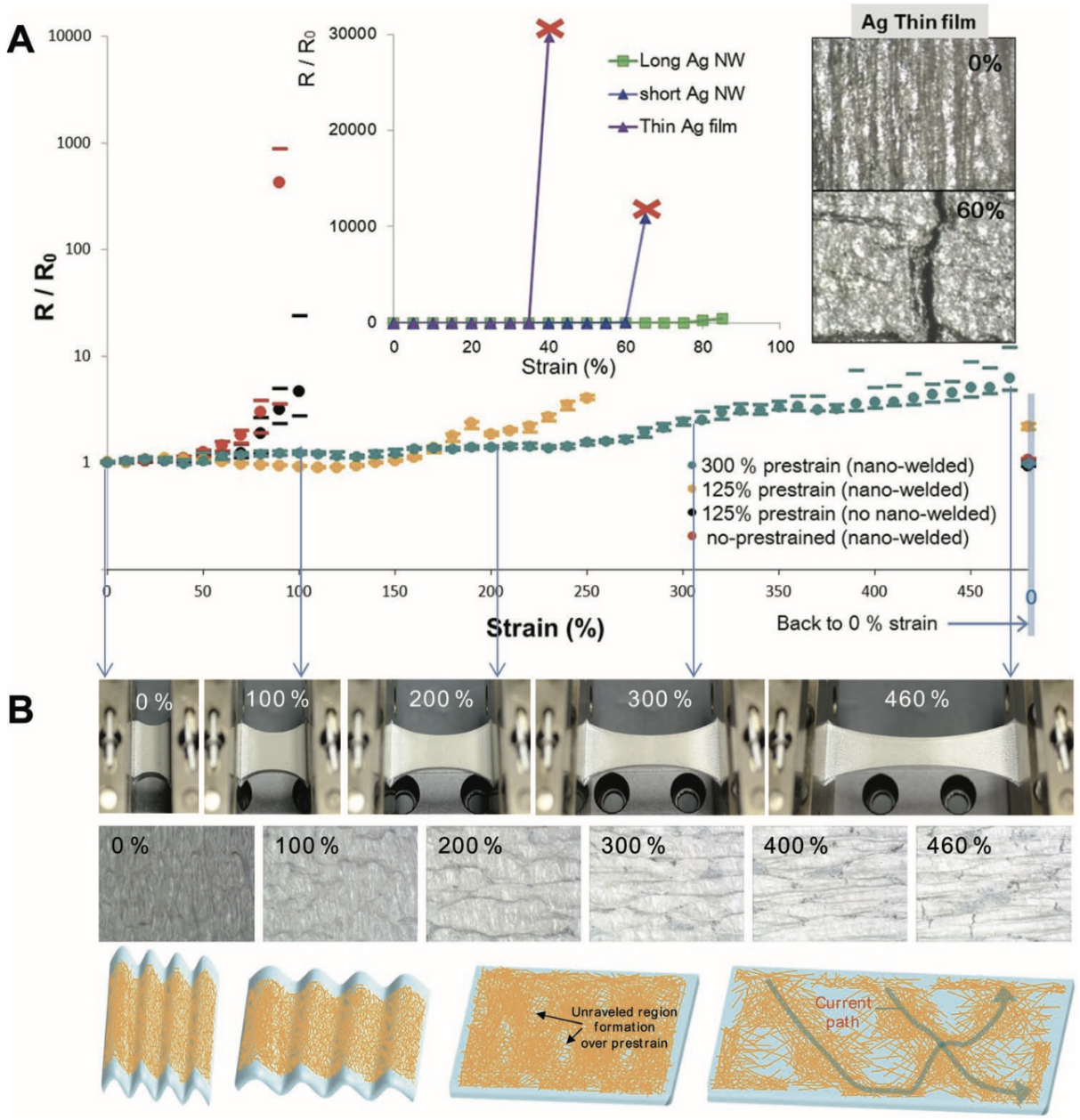

Figure 1.2: (a) Relative resistance change measurement under various strains for a highly stretchable electrode on pre-strained Ecoflex substrates. Inset graph shows the relative resistance change for a Ag thin film (purple), a short AgNW percolation network electrode (blue), and an electrode (green) during stretching on 50% pre-strained Ecoflex substrates. (b) Digital pictures of macroscopic (top row) and microscopic (middle row) surface morphology of an electrode on a pre-strained Ecoflex during a 460% stretching process in Figure 1.2A (green circle symbols). Schematic behavior of the very long AgNW percolation network (VAgNPN) electrode and an Ecoflex substrate during stretching (bottom row). Reprinted from Ref.[10].

into PEDOT:PSS promotes phase separation, and the assembly of PEDOT:PSS:Zonyl fibrils increases the stretchability of the composite. The thin film can retain conductivity up to 188% strain and are reversibly stretchable up to 30% strain without noticeable change in sheet resistance.[11, 12] The ionic salt, lithium bis(trifluoromethane)sulfonimide (LiTFSi), offers several benefits for PEDOT:PSS films, inducing phase separation between PEDOT-rich and PSS-rich domains and enhancing PEDOT domains crystallinity, resulting in high electrical conductivity. Figure 1.3 shows the thin film with ionic salt additives can maintained high conductivity of 3600 S/cm even after 1000 cycles of 100% strain.[13] Blending soft polymers into conducting polymers may soften the polymer chains, thereby reducing the modulus of the material. Poly(ethylene glycol) (PEG), polyurethane (PU), poly(vinyl alcohol) (PVA) are representative examples of soft polymers with good miscibility and bonding with PEDOT:PSS. For example, the mixture of PEDOT:PSS solution and PVA showed elongation at break at 50% of tensile strain with the conductivity of 172 S/cm.[14]

1.2.2 Structure Design for Stretchable Electronics

Another strategy to fabricating stretchable electronics is to simply deposit thin film materials on elastomers with designed geometric patterns that can withstand in-plane strain and bending without affecting electrical performance. This method can produce low-resistance metal films due to the use of conventional clean-room processes, including thermal evaporation, photolithography, and etching. The serpentine structure is one of the design approaches to absorb the external strain, which is accommodated by the in-plane rotation or buckle of the line segment, thus greatly reduces the direct strain on the film. Serpentine-patterned gold (Au) films integrated with transistors, light-emitting diodes, and electrophysiological sensors can be repeatedly stretched by up to 30%, a strain that matches that of human skin.[15] Silver nanoparticles (AgNPs) printed on polyurethane acrylate substrates can achieve gauge

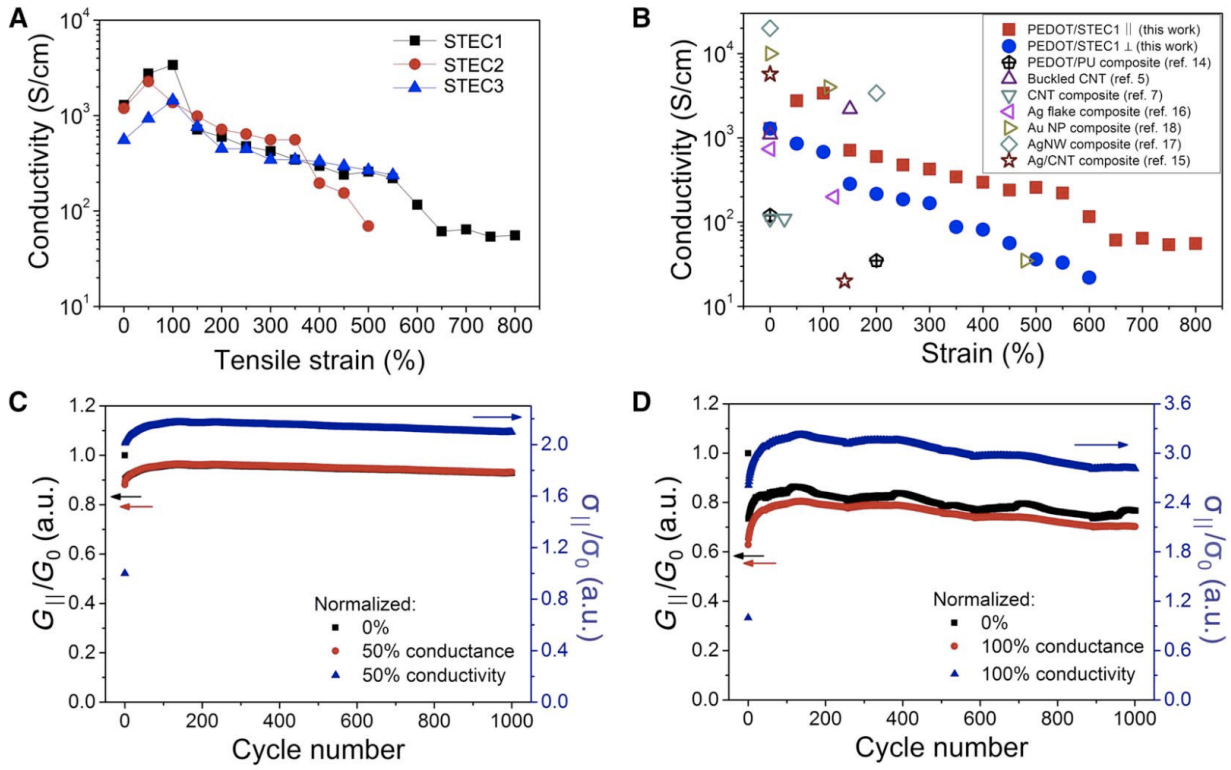

Figure 1.3: Electrical and optical properties of stretchable PEDOT under strain. (a)Conductivity under various strains for PEDOT with different stretchability and electrical conductivity (STEC) enhancers. Film thicknesses are around 600 to 800 nm. (b) Conductivities under various strain presented in this work compared to representative stretchable conductors reported in literature. (c and d) Cycling stability of PEDOT/STEC1 under 50% strain (c) and 100% strain (d). Reprinted from Ref.[14].

factors by tuning the radius curvature, where a small radius of curvature (r = 200 μm) shows higher gauge factor and a large radius of curvature (r = 1600 μm) exhibit a relatively small resistance change upon stretching.[16] More details of the geometric design are shown in Figure 1.4. The choice of size and layout structure (such as von Koch, Peano, Hibert or Moore curves) provides the opportunity to tune the mechanical properties of the film, especially for materials that cannot withstand mechanical stretching. Both simulation and experimental studies have shown that the shape and radius of curvature of the serpentine including the ribbon width, the arc radius, the arc angle, and the arm length are heavily influence the stretchability.[17]

Besides the serpentine structure, the wavy structure can be reversibly stretched and released in response to external strain without sacrificing electrical properties. The external tensile strain can be accommodated by changes in the wavelength and amplitude of the wave structures formed on the elastic substrate. In practice, wavy structures are formed by pre-straining an elastic substrate followed by thin film deposition. After releasing the pre-strain, the thin film is wrinkled due to compressive strain, resulting in a stretchable thin film. For example, reduced graphene oxide (rGO) microribbons become buckling in the stretching directing on a piece of pre-stain PDMS which can be stretch up to 100% with no noticeable damages or defects through the entire film.[19] Figure 1.5 is an example of showing that the thin film with wavy structure has smaller peak strain compared to the in-plane structure. The elasticity of the wave-like structure is related to the amplitude and the spacing between two adjacent tips (or peaks), where the maximum strain concentrated in the thin film is positively related to the amplitude of the wave and inversely related to the spacing between two adjacent tips of the wave.[20]

Nanomesh structures with spring-like traces can demonstrate the stretchability of the metal thin films due to the sliding properties of the nanomesh bundles that can redirect external

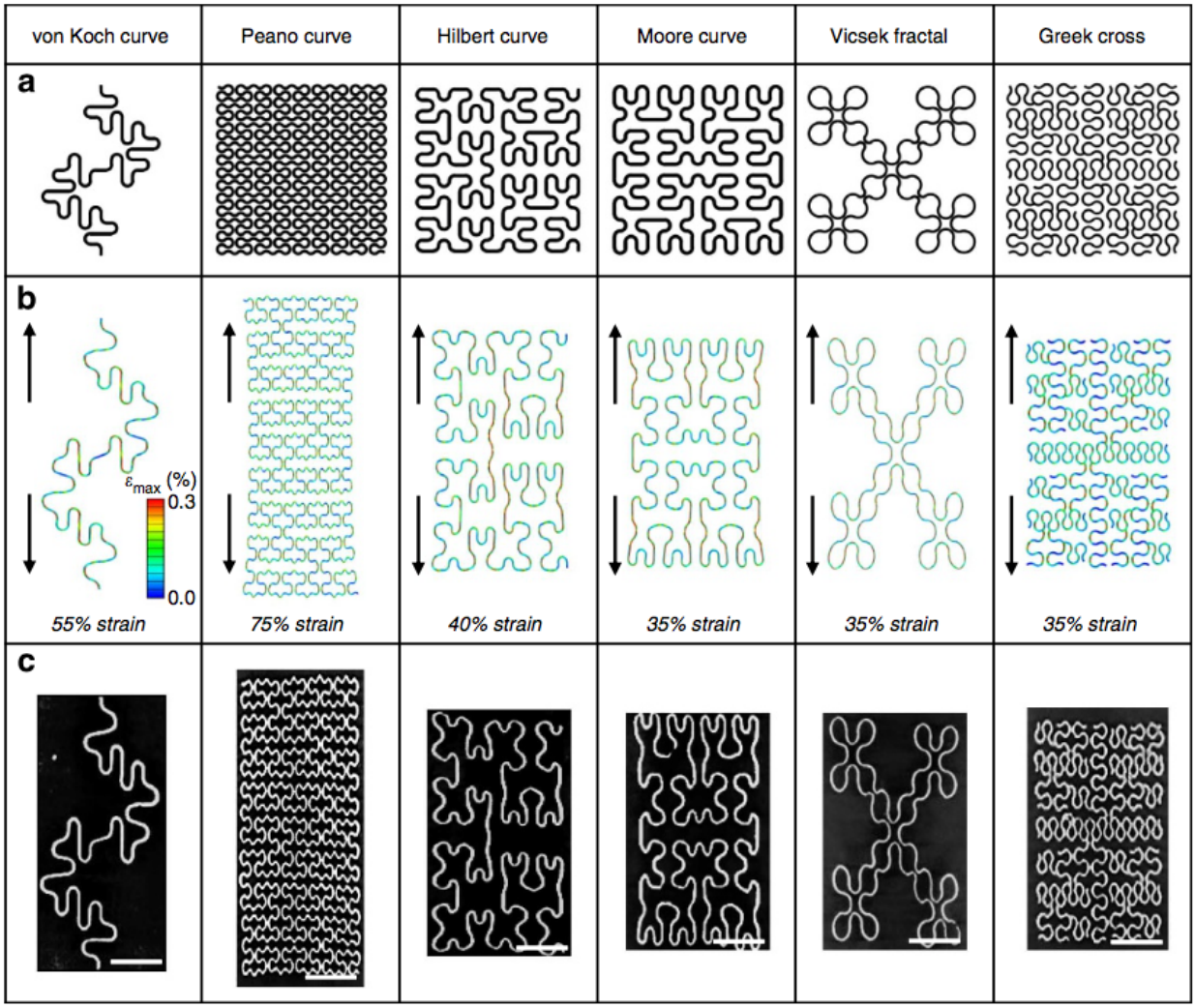

Figure 1.4: (a) Six different patterns of metal wires fully bonded to elastomer substrates demonstrate the application of deterministic fractal designs as general layouts for stretchable electronics. These patterns include line, loop and branch-like geometries, and they are applicable to a broad range of active and passive electronic components. In all cases, arc sections replace the sharp corners from the mathematically defined fractal layouts to improve the elastic mechanics. (b) FEM images of each structure under elastic tensile strain and (c) their corresponding experimental MicroXCT images demonstrate the elastic mechanics. The wires consist of layers of gold (300 nm) sandwiched by polyimide (1.2 mm) and mounted on an elastomeric substrate (0.5 mm). Scale bars, 2 mm. Reprinted from Ref.[18].

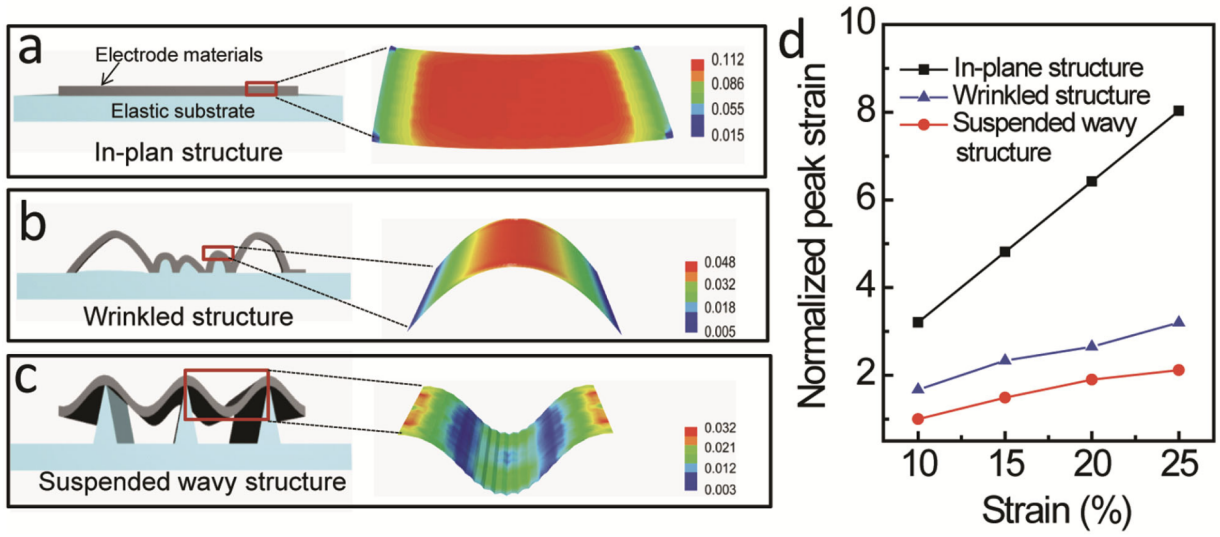

Figure 1.5: Schematic drawing of the different electrode arrays and their relevant strain distribution by the finite element modeling analysis for a) in- plane structure, b) wrinkled structure, and c) suspended wavy structure. d) The peak strain comparison of in-plane structure, wrinkled structure, and suspended wavy structure, respectively. Reprinted from Ref.[19].

stresses. After the stress is released, the metal nanomesh will return to its original state without mechanical and electrical failures. There are two common strategies to form nanomesh structures, one is electrospinning nanofibers to randomly form nanomesh, and the other is designing nanomesh configurations, such as mesh line width and mesh size, leading to different maximum elongation rates before failure as shown in Figure 1.6.[21] The randomized Au nanomesh can be deposited on a water-soluble polyvinyl alcohol (PVA) electrospun polymer, in which the PVA nanofibers can be easily dissolved in an aqueous environment and form Au nanomesh conductors. This substrate-free Au nanomesh exhibits excellent electrical and mechanical stability with tensile strain up to 40% after 10,000 cycles, and the nanomesh provides gas permeability and conformability to the human skin, which can be used as on-skin sensors.[22] The optimization of the Au nanomesh design can be achieved by photolithography and etching processes,[23] where a mesh with a line width of 70 nm, a thickness of 40 nm, and a mesh size of 1 μm exhibits a low sheet resistance of 28 $\Omega/\square$ at 300% of tensile strain

and the mesh shows no electrical and mechanical failure after 50000 stretches up to 150% of tensile strain.[21]

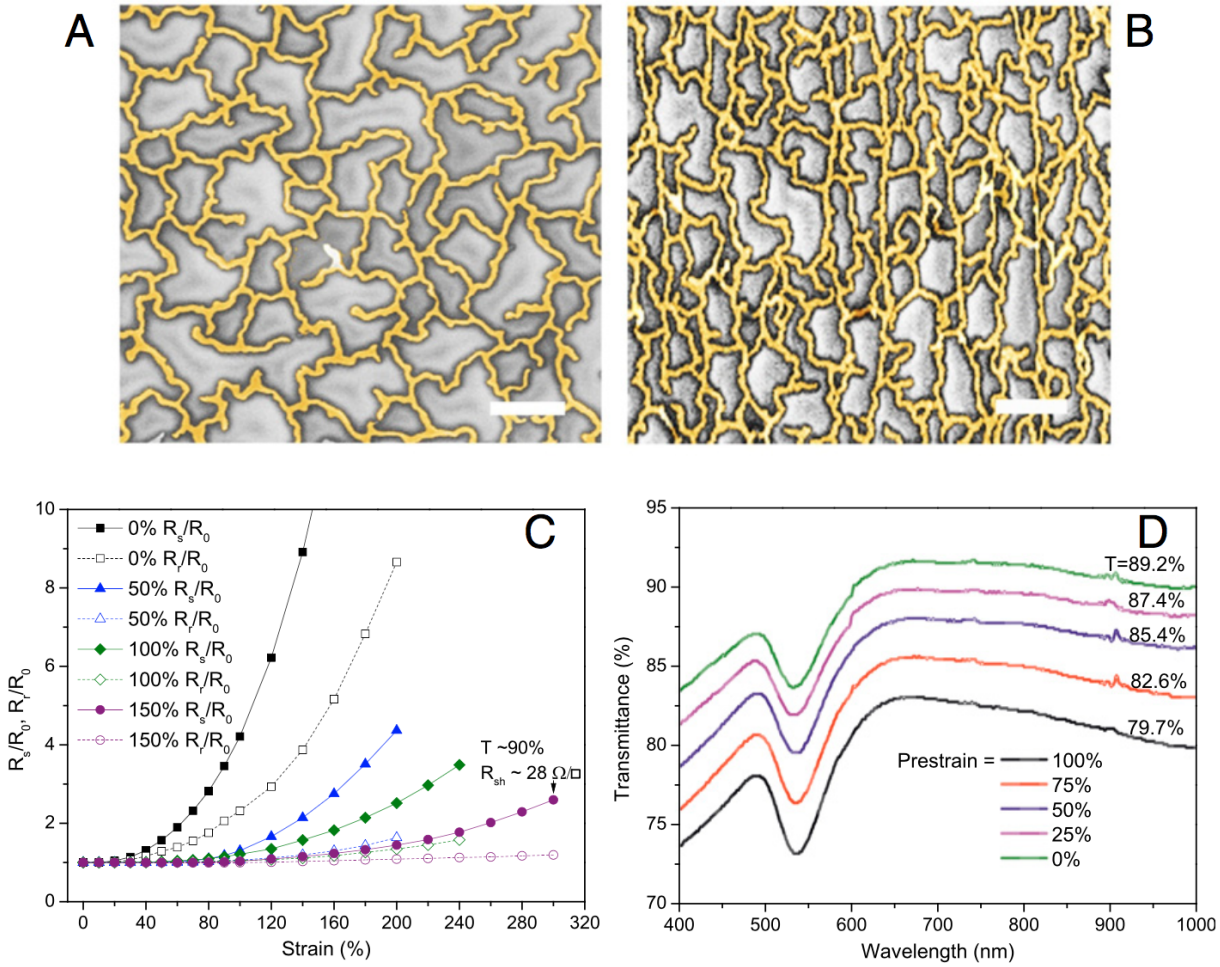

Figure 1.6: Stretchability, transmittance, and strain fatigue of prestrained Au nanomeshes on as-cured PDMS. (A and B) SEM images of as-made and prestrained Au nanomeshes on PDMS, respectively. (Scale bars, 1 μm.) (C) R_s/R_0 and R_r/R_0 as a function of strain for Au nanomeshes with different prestrains of 0, 50, 100, and 150%. Both R_s/R_0 and R_r/R_0 for each nanomesh are shown. The sample with a 150% prestrain has a T ~90% and an R_sh ~28 Ω/□ when stretched to 300%. (D) Transmittance of an Au nanomesh under different prestrains of 0, 25, 50, 75, and 100%, indicating that T slightly decreases with the increasing of prestrain. Reprinted from Ref.[21].

1.3 Scalable Fabrication by Printing

Printed electronics is an electronic product that is manufactured by printing equipment such as screen, gravure or inkjet printers and is considered low-cost manufacturing. The functional materials used in such technologies are often solution-based, which are then deposited on various types of substrates to create transistors, sensors, antennas and circuits. There are several advantages for printing electronics, (1) the size of the substrate is not limited by size of the wafer; (2) the extreme low-cost fabrication enables various applications; (3) flexible and stretchable substrates such as paper and elastomers are permitted. The following subsection will introduce screen printing and inkjet printing methods.

1.3.1 Screen Printing

Screen printing is one of the high-volume printing methods consisting of squeegees, mesh, functional inks and substrates. The manufacturing process begins with the placement of functional ink on the stencil/screen mesh. The squeegee then applies force to the ink, squeezing it through the mesh openings and transferring it to the substrate. The resolution and the printing quality of the pattern strongly depends on the mesh size, printing speed, substrate properties, angle of the squeegee, emulsion thickness and ink composition.[24] High-viscosity inks (3 - 10 Pa-s at a sheer rate of 230 s^{-1})[25] are typically used for screen printing, while low-viscosity inks flow easily through the substrate after ink transfer. In order to produce high-resolution patterns, it is crucial to change the surface energy of the substrate, where a decrease in the surface energy of the substrate leads to a decrease in the wettability of the functional ink, thereby increasing the resolution. However, if the surface energy is too low, the material may not deposit uniformly. Therefore, the study of ink viscosity and substrate surface energy is the key to ensure printing quality. The feasibility of the screen

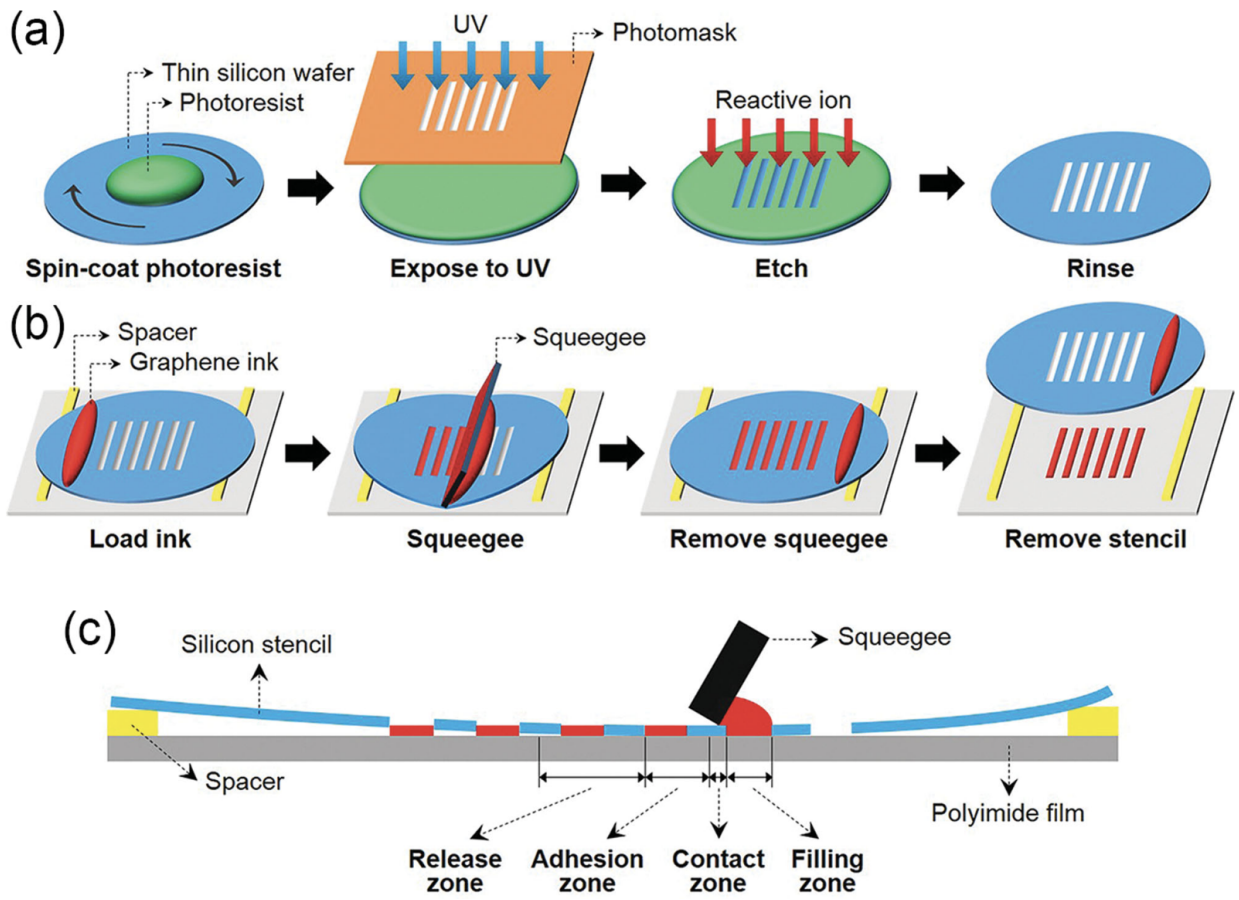

Figure 1.7: (a) Fabrication steps for a thin silicon stencil using conventional lithography techniques. (b) Schematic process of screen printing using the silicon stencil and a pristine graphene ink. (c) Cross-sectional illustration of the screen printing method with the flexible silicon stencil during printing. Reprinted from Ref.[29].

printing has been demonstrated in the following areas including displays, sensors and flexible circuits.[26–28] For example, Figure 1.7 demonstrates screen printing processes of the high resolution of 40μm graphene patterns through a 5μm mesh opening and 90μm thickness stencil on polyimide substrate for electrolyte-gated transistors.[29]

1.3.2 Inkjet Printing

Inkjet printing is an emerging printing method for developing complex device structures and high-resolution patterns of solution-based nanomaterials.[30, 31] The advantages of inkjet printing include ease of operation, the system does not require masks, and the design can be easily adjusted via software. Additionally, the amount of ink used is typically within a few milliliters, as the ink only needs to be deposited on the desired pattern, which is ideal for rapid prototyping. The functional inks typically have low-viscosity for filling into inkjet nozzles where the high-viscosity fluid may cause nozzle clogging. The mechanism of the inkjet printing is due to the actuation of an actuator adjacent to the nozzle head, which then induced a pressure pulse to form a droplet. There are several types of mechanisms for actuating inkjet nozzles, including thermal and piezoelectric inkjet systems as shown in Figure 1.8. Thermal inkjet systems use a heating element where the heating element vaporizes the surrounding ink, causing air bubbles within the nozzle, which then increases pressure to eject the ink.[32, 33] However, one limitation of thermal inkjet systems may be the evaporation of high-boiling functional inks, which makes bubble formation difficult at relatively low temperatures. On the other hand, if the ink is exposed to high heating temperatures, it may cause the ink to decompose, thereby changing the composition of the ink. The other approach is the piezoelectric inkjet system, which takes advantage of piezoelectric crystals, where the material deforms when a voltage is applied. This piezoelectric crystal usually surrounds the nozzle tip, and when the piezoelectric crystal deforms, the nozzle tip generates a pressure pulse that squeeze the droplets to eject.[34] The resolution of inkjet printing is largely dependent on the size of the nozzle head, which can be in the tens of microns, and this high-resolution capability is useful for transistors and light-emitting diodes. For example, a feature size of 2 μm was achieved in the study of the oxide semiconductor thin film transistors.[35]

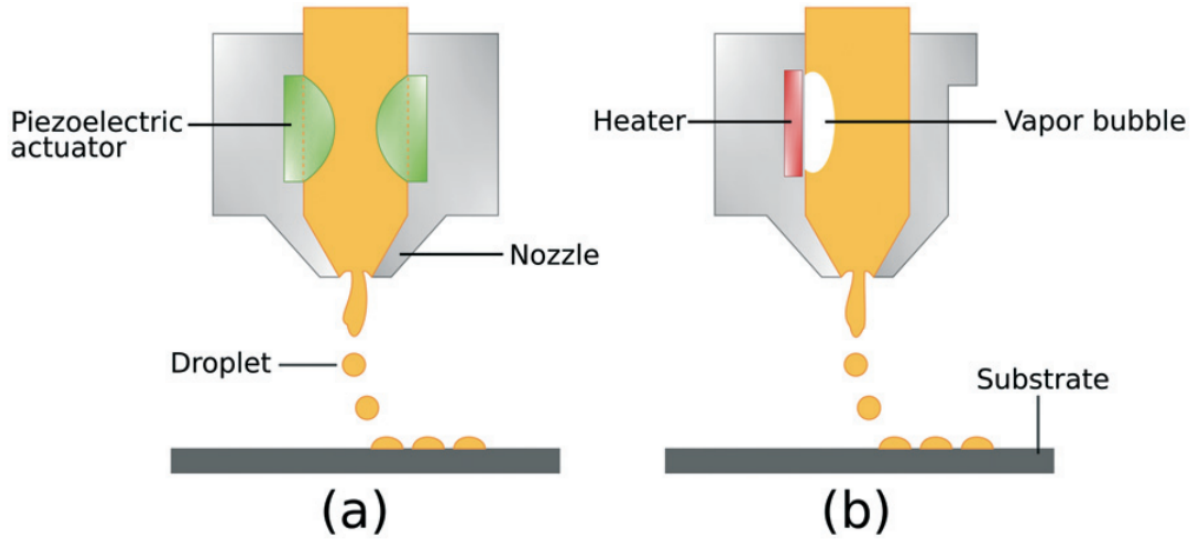

Figure 1.8: Schematic illustration of drop-on-demand (DOD) inkjet printing process: (a) piezoelectric DOD mode and (b) thermal DOD mode. Reprinted from Ref.[36].

1.4 Stretchable Electronics for Wearable Applications

1.4.1 Wearable Health Monitoring Devices

Skin is the largest organ of the human body that consists of the epidermis, dermis, hypodermis and muscle layers from outside to inside. It protects bacteria from the external environment, enables sense of touch, and acts as a layer that generates and transmits biological signals. Over the past decade, researchers have been developing several types of wearable sensors, focusing on information provided by the skin. For example, the biopotential signals (electrocardiogram (ECG or EKG), electroencephalogram (EEG), electromyogram (EMG)) from the muscle layer, body temperature from the hypodermis and dermis layers, and sweat from the epidermis, are the useful biological information available on the skin. More details are shown in Figure 1.9. We can monitor these biosignals to detect early-stage disease or track chronic diseases and personal health conditions. To start with, the ECG signal produced by muscle contractions

in the heart chambers tells the heart rate and rhythm. A cycle of the signal includes a P wave representing arterial depolarization, a QRS complex corresponding to ventricular depolarization, and a T wave representing ventricular repolarization. The analysis of these waveforms can be utilized as indicators of heart disease, heart attack, and arrhythmias.[37, 38] In order to collect strong ECG signals, electrodes are typically placed on the patient's chest and shoulder. EMG signals generated from muscle fiber contractions indicate the activity of muscle cells and nerve cells. The waveforms serve as an important tool for diagnosing neuromuscular disorders.[39] In practical clinical settings, electrodes for monitoring EMG signals are placed over the desired muscle group. EEG signals produced by the ionic current flows through neurons in the cerebral cortex serve as detectors for seizure and sleep disorder.[40] The signals are generally classified into delta, theta, alpha, beta and gamma waves according to the signal frequency range which various symptoms can be assessed. Since EEG signals come from neurons in the human brain, recording is done by covering electrodes on the scalp.[41] Electrodes used in today's clinical settings are essentially rigid, which results in a mismatch in the properties of the electrode-skin interface, leading to the motion artifact and discomfort. Many research groups have come up with strategies to develop elastic electrodes, including stretchable conducting polymer and electronic tattoos with mechanical properties that match human skin.[22, 42–44]

Besides the biopotential signals generated by the muscle layer, the hypodermis and dermis layer also provide essential information related to cardiovascular health where the subcutaneous blood vessels provide blood pressure and arterial pulse waves, the hypodermis layer regulates the body temperature. For example, pressure sensors can monitor blood pressure to spot high blood pressure, while epidermal thermal sensors can track body temperature to provide overall health condition.[45–48] Lastly, sweat collected from the epidermal layer contains various biomarkers that reflect human physiological state. These biomarkers include ions

and molecules which can be used for drug detection and disease diagnosis. For example, sodium and potassium ions are important in determining an athlete's hydration status. Glucose concentration is associated with diabetes, while urea levels in sweat are related to kidney failure. Scientists have reported various electrochemical sweat sensors made on elastomeric substrate integrated with flexible printed conductive board (FPCB) providing real-time clinical investigation.[49–51] Considering the complexity of the human body, the electronic-skin interface, and the robustness and stability of wearable sensors, there are still many areas that can be further explored from the novel materials development, low-cost fabrication processes, sensor packaging and system integration to the clinical testing and validation.

1.4.2 Wearable Human–Machine Interface

With the advancement of various sensors, human-machine interfaces have transformed from traditional keyboards, controller controls to wearable gloves and sensors.[4, 53] Humans can communicate with equipment or robots not only through speech and vision, but also through finger movements. However, traditional rigid and bulky devices hinder user wearability and comfort. To overcome this limitations, a soft wearable sensor system with excellent electrical properties and mechanical stretchability may be able to addresses the discomfort and mechanical mismatch problems. Soft electronics can be attached to curvilinear skin surfaces to monitor human movement and physiological signals. The device can also be made lightweight, ultra-thin, and attach completely to the human body, thereby greatly reducing motion artifacts between the sensor and the skin and improving the signal-to-noise ratio. Moreover, the system can integrates various types of motion sensors for high precision multisensory control when bending or stretching.

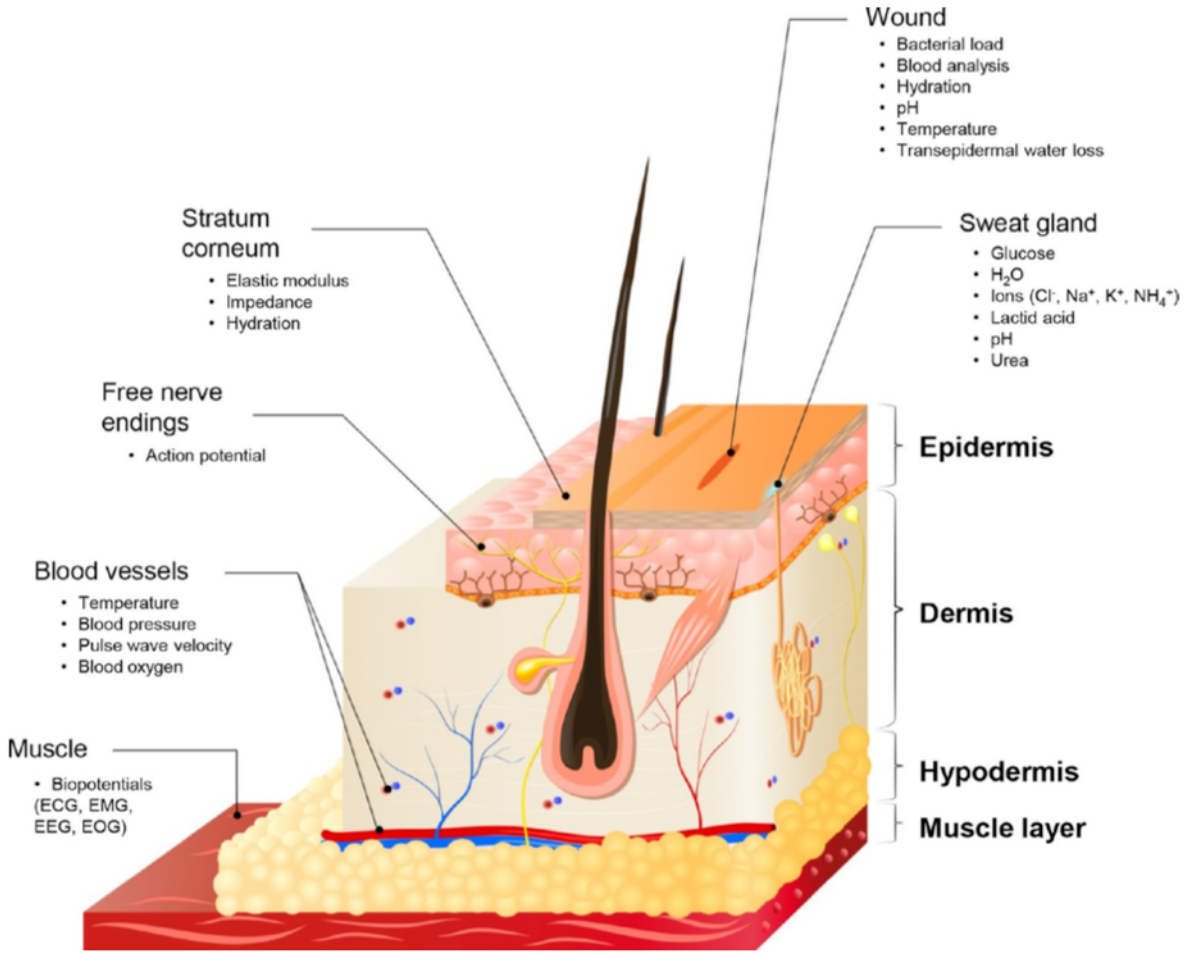

Figure 1.9: Diagnostic signals from muscles, blood vessels, free nerve endings, stratum corneum, wounds, and sweat glands.Reprinted from Ref.[52].

To capture human motion, pressure and strain sensors are the most commonly used. According to the working mechanism, pressure sensors can be divided into resistive, capacitive, piezoelectric and triboelectric.[54–57] Resistive pressure sensors usually consist of a conductive thin film sandwiched between two elastomers, and their sensing mechanism is to measure resistance changes due to external forces. The sensor requires only a simple readout circuit with high sensitivity. In general, elastomers can be PDMS or Ecoflex and the conducting thin film can be nanowires and nanoparticles.[58, 59] Capacitive pressure sensors typically have high sensitivity and fast response, with a dielectric layer sandwiched between two electrodes. The sensing mechanism mainly comes from the measurement of capacitance changes caused by changes in the distance between electrodes. Sensitivity and pressure detection limits can be further adjusted by using different dielectric layer structure designs or selecting different dielectric materials.[60, 61] Besides pressure sensor, strain sensor is also a key component in human motion detection, mainly used to monitor finger motion from the bending angle of each joint. The sensing mechanism is also divided into two types, resistive and capacitive. The resistive strain sensor utilized the disconnection or the microcracks of conductive thin film under external tensile strain,[62, 63] while the capacitive strain sensor is governed by the geometrical changes.[64–66]

Figure 1.10 shows an example of a human-machine interface wearable device using porous pressure-sensitive rubber as pressure sensors and strain gauges. Porous sensitive rubbers are made by mixing multi-walled carbon nanotubes (MWNTs), PDMS and reverse micelle solutions. In this device, pressure sensing is accomplished by the deformation of the PDMS that changes the position of the MWNTs, where the resistance increases with increasing pressure. And, strain sensing is performed through destruction of conduction MWNTs network, where the resistance also increases with the increasing tensile strain. By combining

both sensor on an elastic patch, the wearable sensor array can be used to control a tank-like robot, demonstrating a human-machine interface.[67]

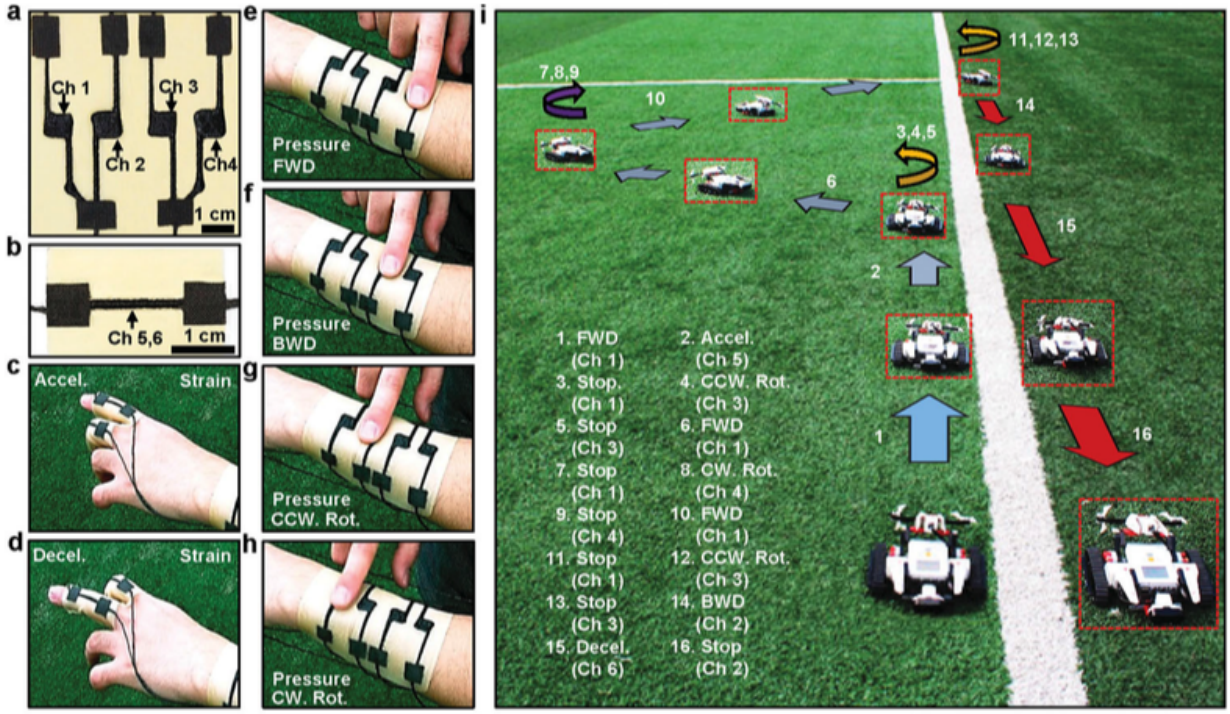

Figure 1.10: a) Image of porous pressure-sensitive rubber (PPSR) pressure sensor printed on the commercial elastomeric patch. The sensor array is composed of four channels of pressure sensors. b) Image of PPSR strain gauge. c,d) Image of triggering commands via PPSR strain gauges for the acceleration of the robot (Ch 5; c) and for the deceleration of the robot (Ch 6; d). e–h) Image of triggering commands via PPSR pressure sensors for moving forward (Ch 1; e), moving backward (Ch 2; f), rotating counterclockwise (Ch 3; g), and rotating clockwise (Ch 4; h). i) Image of robot movement traces. A series of commands were triggered. Each command is numbered on the figure. The numbers and corresponding commands are explained on the left bottom corner of the figure. The robot images in red dotted boxes are captured from the images of each event in Figure S10 in the Supporting Information. Reprinted from Ref.[67].

1.5 Motivation, Challenges and Contribution

There is an increasing need for real-time health monitoring for chronic illnesses management to aid in diagnosis and assist with treatment. Some chronic illness can be lethal such as heart disease, high blood pressure and stroke if not treated properly immediately.[68, 69] In practical clinical settings, equipment for recording biophysiological signals are normally bulky and wired, which is inconvenient for the patients. Instead, wearable electronics have great potential to record various forms of biophysiological signals in a miniaturized device, which can easily attach to the human body and provide rapid assist with disease. However, commercialized wearable electronics are often made of inorganic silicon-based materials, which are considered rigid, while biological livings have irregular shapes with various structures, such as skin surfaces and tissues. This mismatch between the mechanical properties of inorganic materials and soft substrates is problematic and causes several issues, including wearing comfort, motion artifacts, and signal quality. Therefore, the ability to freely deform and bend features on consumer electronics that can form intimate contact with curvilinear surfaces is critical for high precision biosignal measurements. Rapid development of flexible electronics has enabled the smart phone and display to fold and bend,[70, 71] while stretchable electronics remains challenges in various aspects such as materials, biocompatibility, fabrication processes, and cost.

Unlike rigid silicon-based materials, organic materials provide the opportunities to accommodate tensile strain while maintaining their electrical properties. Several stretchable conductors have been developed including liquid metals, carbon nanotubes and silver nanowires[72–74] that connect between the electronic components on a piece of elastic substrate such as PDMS, Ecoflex or poly(styrene-butadiene-styrene)(SBS).[75–77] The silver nanoparticle and stretchable PEDOT:PSS composite are demonstrated in this thesis. For some applications,

the electronics need fully contact with the biological livings such as ECG and EMG patches as well as implantable devices that wrap around blood vessels or cover irregularly shaped organisms. In such scenario, the biocompatibility of the material becomes critical, i.e. chemically inert and compatible with living cells.[78–80] In this work, the porous PEDOT:PSS electrode is presented to be biocompatible with the ability to record high quality physiological signals. Fabrication step and the cost is another challenge that is highly correlated to the commercialization of the devices, where most conventional electronic devices utilize the operation of high-temperature and high-pressure cleanroom processes, which can be destructive for organic-based stretchable materials. Thus, a new type of fabrication processes enables low temperature and ambient pressure should be established. Researchers have investigated printing techniques that can develop electronic devices on soft substrates at low cost and high volume. In addition, lower manufacturing costs have the potential to make these devices single-use or disposable in certain clinical settings. Lastly, the stability and durability of stretchable electronics remains a challenge because some stretchable polymer composites are hygroscopic, absorbing moisture in the surrounding environment and affecting their thermal, mechanical and electrical properties. The encapsulation and integration of these materials is critical for long-term applications without failure.

This thesis focuses on low-cost sensor design, fabrication, and characterization for wearable health monitoring applications to address challenges mentioned above. More specifically, we demonstrated different types of sensors to improve user wearing comfort, obtain signal accuracy in real clinical settings, and reduce manufacturing costs. They are listed as follows:

Sphygmomanometer is most commonly used to measure blood pressure to properly diagnose and manage hypertension. Some patients feel uncomfortable during the measurement because sphygmomanometer squeezes your arm until the pressure in your veins is cut off. To address this issue, we demonstrated a low-cost and light-weighted soft silver nanoparticle-based

pressure sensor for monitoring arterial pulse to diagnose the stiffness and health of blood vessels. In addition, arterial pulses can be translated into blood pressure.[81] Therefore, the developed pressure sensor may replace the sphygmomanometer. Commercially available Ag/AgCl ECG electrodes do not conform well to human skin and may cause noticeable motion artifacts during signal recording. Moreover, it usually has a small active area and is surrounded by a large area of adhesive or packaging materials that do not contribute to signal collection. Additionally, the short drying time of conductive hydrogels is not suitable for long-term recording. We developed a porous PEDOT:PSS electrode that exhibits low electrode-skin contact impedance, less motion artifacts, and the ability for long-term ECG recording aim to address the above challenges. Stretchable conductors are key components connect each sensor unit, although metal conductors are widely used in commercial electronic products, whose insufficient mechanical strength prevents them from being compatible with soft electronic devices. In order to address this issue, we developed an intrinsically stretchable PEDOT:PSS-based conductors that can withstand up to 50% of tensile strain. Lastly, a single modality sensor is not enough to capture and evaluate a variety of physical or chemical stimuli. To develop multimodal sensors, it is most common to integrate them side-by-side or stack them layer-by-layer, which requires a more complex fabrication process. Instead, we demonstrated a structurally simple porous PEDOT:PSS/PDMS sensor that can respond and differentiate to pressure, tensile strain, and temperature by simultaneously measuring the resistance and capacitance of the sensor. With its low cost and multimodal sensing, it can be widely used for object detection and gesture recognition. The developed materials, fabrication techniques and integration of sensors have demonstrated its feasibility and potential for low-cost clinical applications and provides a new entry point for more complex stretchable electronic systems.

1.6 Thesis Overview

The chapters are organized as follows:

Chapter 2 mainly focuses on the development of a new sensing mechanism for pressure-induced strain in printed silver nanoparticle films, which can measure pressure through the resistance change of the film. The sensor is composed of simple structure with three layers, a PDMS substrate, a silver nanoparticle thin film, and a VHB encapsulation layer. This simple structure sensor fabricated by inkjet printing shows high pressure sensitivity for arterial pulse monitoring and the ability to detect various sound pressure levels.

Chapter 3 dedicated to the formulation of stretchable PEDOT:PSS composite that can be patterned using inkjet printing process while exhibiting low sheet resistance and accommodating external mechanical deformation. We systematically studied the effect of various types of polar solvent additives that can help induce phase separation of PEDOT and PSS grains and change the conformation of a PEDOT chain, thereby improving the electrical property of the film by facilitating charge hopping along the percolating PEDOT network. Elasticity can also be achieved by blending the above solution with the soft polymer poly(ethylene oxide) (PEO). Thin films of PEDOT:PSS/PEO polymer blends patterned by inkjet printing exhibits a low sheet resistance of 84 $\Omega/\square$ and can resist up to 50% tensile strain with minimal changes in electrical performance. With its good conductivity and elasticity, we have further demonstrated the use of the polymer blend as stretchable interconnects and stretchable dry electrodes on a thin PDMS substrate for photoplethysmography and electrocardiography recording applications.

Chapter 4 discusses an elastomeric sponge electrode that offers reduced electrode-skin contact impedance, improved signal-to-noise ratio, and is ideally suited for long-term and motion-artifact-tolerant recording of high-quality biopotential signals. The sponge electrode utilizes porous PDMS sponge made from a sacrificial template of sugar cubes, and it is subsequently coated with a PEDOT: PSS conductive polymer using a simple dip-coating process. The sponge electrode contains numerous micropores that greatly increase the skin-electrode contact area and help lower the contact impedance by a factor of 5.25 or 6.7 compared to planar PEDOT:PSS electrodes or gold-standard Ag/AgCl electrodes, respectively. The lowering of contact impedance resulted in high-quality ECG and EMG recordings with improved signal-to-noise ratio. Furthermore, the porous structure also allows the sponge electrode to hold significantly more conductive gel compared to conventional planar electrodes, thereby allowing them to be used for long recording sessions with minimal signal degradation. The conductive gel absorbed into the micropores also serves as a buffer layer to help mitigate motion artifacts, which is crucial for recording ambulatory patients. We have further demonstrated its feasibility and potential for clinical usage that the sponge electrode can be used to monitor the uterine contraction activities of a patient in labor.

Chapter 5 shows an elastomeric sponge-based sensor that can respond to and distinguish three different kinds of stimuli: pressure, strain, and temperature. Again, the sensor utilizes a porous PDMS sponge fabricated from a sugar cube sacrificial template, which was subsequently coated with a PEDOT:PSS conductive polymer through a low-cost dip-coating process. Responses to different types of stimuli can be distinguished by simultaneously recording resistance and capacitance changes. Because pressure, tensile strain, and temperature change result in different trends in resistance and capacitance change, those stimuli can be clearly distinguished from each other by simultaneously measuring the resistance and capacitance of the sensor. As a proof-of-concept, we have demonstrated the use of the porous sponge

sensor on an artificial hand for object detection, gesture recognition, and temperature sensing applications.

Chapter 6 summarized the work in this thesis and provide an outlook of the future work.

Chapter 2

Fully Inkjet-Printed Soft Resistive Pressure Sensor Patch

2.1 Introduction

Recent development on smart wearables, health monitoring devices, and soft robotics has attracted a great amount of interest in flexible or stretchable physical and chemical sensors.[51, 82–90] Among the various types of flexible sensors, pressure sensor is one that has been extensively studied, and there is an increasing demand for lightweight, skin-conformable, and disposable soft pressure sensors with high sensitivity.[91–94] There are a number of pressure sensing mechanisms available, including resistive,[95, 96] capacitive,[97, 98] and piezoelectric.[99, 100] Capacitive pressure sensors are typically composed of an elastomeric dielectric layer sandwiched between two parallel-plate electrodes, whose capacitance changes under pressure due to the deformation of the dielectric layer. Although capacitive pressure sensors have some advantages including simple device structure and easy fabrication, they

typically exhibit low sensitivity and also require more sophisticated readout circuits that can measure very small capacitance change (typically in the range of hundreds of femtofarad). Moreover, parasitic capacitance and cross- talk between the pixels could also lead to reduced sensitivity and spatial resolution. Piezoelectric materials such as polyvinylidene difluoride that can generate electrical charges from mechanical impact can also be used for pressure sensing.[99] However, such piezoelectric sensors are not suitable for measuring static pressure as they only respond to dynamic changes in pressure. Considering the above, resistive pressure sensors are more promising as they typically offer great sensitivity and only require very basic readout circuit that can measure resistance change. The resistive pressure sensors are typically made using thin films of conductors, such as nanocomposites[95] or nanowires,[96] whose electrical resistance changes under mechanical strain due to microscopic change in morphology or increase in distance between the conductive fillers.[101–103]

For sensor fabrication, inkjet printing[16, 104–112] has been widely used and the advantages are multifold. First, the printing process greatly simplifies the fabrication by completely eliminating the need for masks (used in photolithography), as well as high temperature or high vacuum processes commonly used in semiconductor microfabrication. Moreover, it is an additive and highly scalable process that can greatly reduce materials waste. For these reasons, the inkjet printing process could allow the sensors to be low-cost and potentially disposable. Many types of printed sensors including strain sensor,[16, 109, 110] temperature sensor,[104, 111] and humidity sensor[107, 108] have already been demonstrated.

We have recently demonstrated the use of inkjet-printed silver nanoparticle (AgNP) pattern on an elastomer substrate as an ultrasensitive strain sensor.[16] Inspired by the capability of using printed AgNP thin film for strain sensing and its very high sensitivity, in this work, we demonstrate a printed resistive pressure sensor whose sensing mechanism is based on pressure-induced strain. The sensor consists of a conductive AgNP layer that is directly

printed onto a polydimethylsiloxane (PDMS) substrate and subsequently encapsulated by a VHB tape. When a pressure is applied perpendicular to the sensor surface, small amount of tensile strain is induced in the AgNP layer, which generates microcracks and leads to a change in electrical resistance. We have systematically studied the influence of substrate stiffness and thickness on the characteristics of the sensor using finite element simulations and achieved an optimized configuration with a pressure sensitivity of up to 0.48 kPa^{-1}. Due to the high sensitivity and low fabrication cost, our printed resistive pressure sensor is particularly suitable for disposable wearable sensor applications. As proof- of-concept, we have demonstrated the use of the printed sensor for detecting acoustic vibration and measuring arterial pulse waveforms.

2.2 Fabrication Process, Measurement Setup and Sensor Design Concept

2.2.1 Fabrication Process

To prepare the substrate, PDMS prepolymer was first mixed with the curing agent (Sylgard 184, Dow Corning, USA) with mixing ratios of either 10:1 or 20:1 w/w. The PDMS was then casted onto a 1 in. $\times$ 1 in. glass slide pretreated with Rain-X (ITW Global Brands) and isopropanol. The 1 mm thick substrate was prepared by sandwiching the PDMS in between two glass slides with a 1 mm spacer and the 0.15 mm thick substrate was prepared by spin coating (500 rpm, 30 s). The PDMS substrate was then cured on a hotplate for 3 h at 80 °C. Silver nanoparticle ink (PG-007AA from Paru Corporation, South Korea) with particle size of 100–200 nm was diluted in ethylene glycol and then printed onto the PDMS substrate using a GIX Microplotter (Sonoplot Inc.) with nozzle openings of 50–200 μm. To aid the

wetting of the ink, the PDMS substrate was treated by oxygen plasma (Plasma Etch PE25, Plasma Etch Inc.) at 30 W for 5 s. After printing the AgNP feature, the sample was placed on a hotplate and annealed for 20 min at 55 °C to remove the polymer binders and then for another 60 min at 150 °C remove the solvent and sinter the silver nanoparticles. As a last step, flexible ribbon cables were used to form electrical connection with the printed sensor and the entire device was packaged by VHB tape (VHB-4905, 3M) to serve as an encapsulation layer. The VHB tape made with acrylic foam is viscoelastic which is desirable for stretchable sensor applications and it also bonds strongly with the low surface energy PDMS substrate.

2.2.2 Measurement Setup

A modified syringe pump with 3D-printed loading rod and loading platform was used for the pressure measurement. A commercially available force sensor (FSR 402, Interlink Electronics, Inc.) was attached to the bottom of the loading platform as a reference sensor to measure the actual pressure exerted by the loading rod. During the experiment, the pressure was applied to both the printed AgNP sensor and the FSR reference sensor and the data from both sensors were record by a Semiconductor Device Analyzer (Keysight B1500A). Before placing the AgNP sensor, the response curve (resistance-pressure) of the FSR sensor was characterized by placing different amount of standard weight on the loading platform.

Both optical microscope (Olympus BX53M) and field-emission scanning electron microscope (JEOL JSM-7001LVF) were used to capture the surface morphology of the printed AgNP thin film. Semiconductor Device Analyzer (Keysight B1500A) was used to measure the electrical properties of AgNP sensor. For each measurement, a constant voltage of 1 V was applied the current through the sensor was measured by the analyzer, from which the resistance value was deduced. The experiment involving human subject has been performed with the full, informed consent of the volunteer, who is also the first author of the manuscript.

2.2.3 Sensor Design Concept

The concept and structure of the printed resistive pressure sensor are schematically illustrated in Figure 2.1a. The device is composed of three layers: the elastic PDMS substrate, printed AgNP thin film, and VHB tape encapsulation. The thickness of the VHB tape is 0.5 mm, while the thickness of the PDMS substrate varies from 1 to 0.15 mm. As will be discussed later, both the thickness and stiffness of the PDMS have great impact on the sensitivity of the sensor. Due to the hydrophobicity of PDMS, pretreating the PDMS substrate with oxygen plasma prior to printing is crucial as it greatly improves the wetting of the ink on the surface and consequently the uniformity of the printed AgNP thin film. As shown in Figure 2.1a, the active sensing region of the device is comprised of a serpentine-shaped printed AgNP pattern, and the whole device is encapsulated by a VHB tape which is stretchable and also offers strong bonding to low surface energy surfaces, such as PDMS. The printing process allows the sensors to be easily fabricated in large quantity and at low cost. A photograph of a roll of PDMS substrate with multiple printed sensors is shown in Figure 2.1b.

The sensing mechanism of the printed resistive pressure sensor can be attributed to the formation of microcracks inside the AgNP thin film under pressure. As illustrated in the left schematic in Figure 2.1a, pressure applied perpendicular to the surface of the sensor causes deformation of the substrate, which induces a tensile strain in the printed AgNP thin film and leads to the formation of microcracks. The microcracks will result in an increase in the film resistance and the change can be measured electrically. In order to understand the relation between the microcracks and tensile strain, a PDMS substrate with printed AgNP thin film was mounted on a linear stretching stage and examined by scanning electron microscope (SEM). Figure 2.1c shows the SEM images taken from the printed AgNP thin film when the sample was stretched under various levels of tensile strain from 0%, 15% to 30% then

released to its relaxed state of 0%. The AgNPs are 100–200 nm in diameter and they are mostly bonded together in relaxed state. From both low magnification (top row) and high magnification (bottom row) images, one can clearly see that an increase in strain leads to increase in both the amount and size of the microcracks and such micro- cracks propagate uniformly through the entire printed AgNP pattern. On the other hand, when the strain is released, the size of the microcracks becomes smaller and the film morphology is recovered to almost the same as the relaxed state. The crack formation and recovery processes are reversible, and it is the reason for the highly repeatable electrical response from the sensor.

Because the response of the sensor depends on the strain induced by the substrate deformation, it is important to under- stand the effect of substrate stiffness and thickness on the induced strain. Finite element simulations were conducted using COMSOL to investigate four different types of sensors with different PDMS stiffness and thickness and the results are presented in Figure 2.2. The variation in PDMS stiffness was achieved by mixing PDMS prepolymer and curing agent at a mixing ratio of either 10:1 (stiffer) or 20:1 (softer), and two different PDMS substrate thicknesses of either 1 or 0.15 mm were prepared. Figure 2.2a displays the simulated deformation under 10 kPa pressure in two samples with 1 mm thick PDMS and mixing ratios of 10:1 or 20:1. The PDMS with a 20:1 mixing ratio results in a softer substrate with a Young's modulus of 2.8×10^5 Pa and the 10:1 mixing ratio results in a stiffer substrate with a Young's modulus of 5.8×10^5 Pa.[113] Simulation results show the softer sample with 20:1 mixing ratio deforms significantly more than the stiffer 10:1 sample. The larger deformation will translate to higher sensitivity as will be discussed later. Furthermore, we have also simulated the maximum principal strain profile for each sample and the results are presented in Figure 2.2b. By comparing the results, one can see that under the same pressure, the samples with thinner (0.15 mm) or softer (20:1) substrate experience greater maximum principal strain compared to the samples with thicker (1 mm) or stiffer (10:1) substrates,

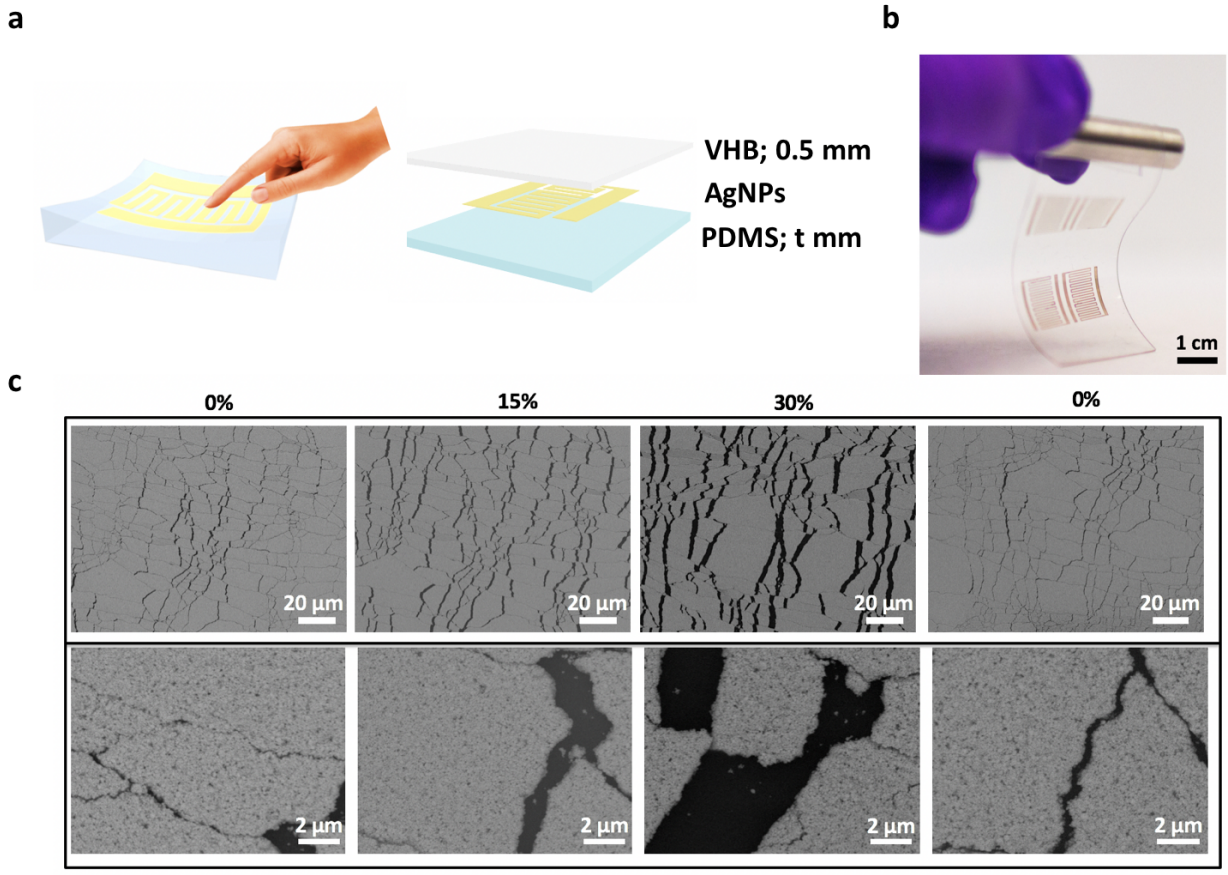

Figure 2.1: Concept and working principle of the printed resistive pressure sensor. (a) Left: schematic illustration of printed resistive pressure sensor. An applied pressure causes deformation in the elastic PDMS substrate, which induces tensile strain in the printed AgNP thin film. Right: Schematic showing the three layers in the pressure sensor. (b) Photo of a representative sample with multiple printed pressure sensors. (c) SEM images of the printed AgNP thin film under different levels of tensile strain from 0% to 30% and then back to 0% showing the increase in amount and size of microcracks in the film under stretching and the recovery when the strain is released.

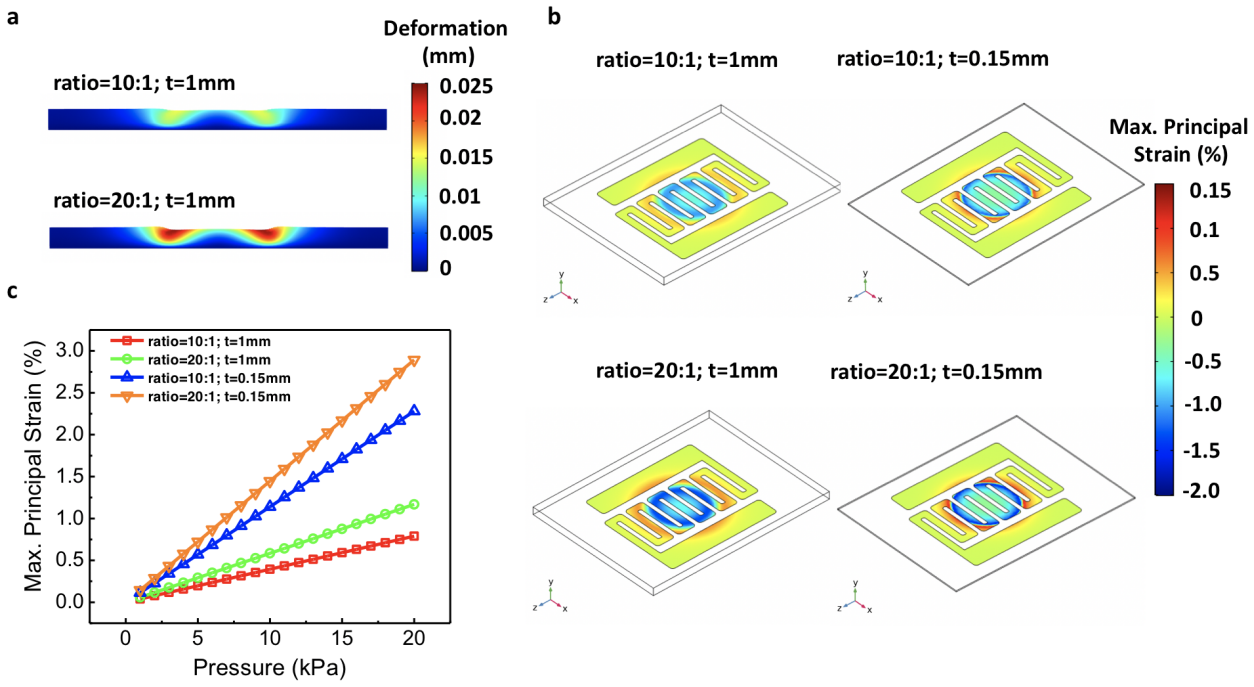

Figure 2.2: Finite element simulation showing the pressure-induced deformation and strain in four types of sensors with different PDMS mixing ratio (10:1 and 20:1) and substrate thickness (1 and 0.15 mm). (a) Deformation in two 1 mm thick sensors with mixing ratio of 10:1 and 20:1 when a pres- sure of 10 kPa was applied. (b) Prfile of the maximum principal strain in four types of sensors when a pressure of 10 kPa was applied perpendicular to the sensor surface. (c) Maximum principal strain plotted as a function of pressure for four types of sensors.

respectively. The simulation results also indicate that the greater the substrate deformation, the larger the maximum principal strain induced. Figure 2.2c summarizes the simulation results of maximum principal strain in all four types of sensors under various pressure levels up to 20 kPa. The results indicate that the maximum strain varies linearly with the applied pressure, and among all samples, the one with a PDMS thickness of 0.15 mm and 20:1 mixing ratio exhibits the largest maximum principal strain under all the conditions.

2.3 Electromechanical Characterization

From the simulation results above, one can expect that the printed sensors with thinner and softer substrate will have more and larger microcracks formed under the same pressure level, which will result in greater change in electrical resistance and better sensitivity. To understand and experimentally test the relation between the pressure/strain and the electrical properties of the printed AgNP thin film, the relative changes in resistance of the sensor ($\Delta R/R_0$, where ΔR is the change in resistance and R_0 is the resistance in relaxed state) were measured as a function of pressure or tensile strain and the results are presented in Figure 2.3. The details about the electro-mechanical property measurement setup are described in the Experimental Section and the pressure applied onto the printed sensor was precisely determined using a commercially avail- able force sensor as a reference. Figure 2.3a shows the sensor response curve ($\Delta R/R_0$ vs P) for all four types of printed sensors described in Figure 2.2. All of them responded similar to the applied pressure and exhibited a linear relationship with increasing pressure from 0 to about 15 kPa. The sensitivity of the sensor can be extracted from the slope of the $\Delta R/R_0$ vs P curve and the results are plotted in Figure 2.3b. The sample with the softest and thinnest PDMS substrate (20:1 mixing ratio and 0.15 mm thickness) exhibits the highest sensitivity of 0.48 kPa^{-1}. The rest of the samples with mixing ratio of 10:1 and thickness of 0.15 mm, mixing ratio of 20:1 and thickness of 1 mm, and mixing ratio of 10:1 and thickness of 1 mm all exhibit lower sensitivity of 0.22, 0.13, and 0.07 kPa^{-1}, respectively. The experimental results again indicate that better sensitivity can be achieved by using thinner and softer PDMS substrate, which is in good agreement with the simulation results above in Figure 2.3c. Furthermore, the sensitivity of 0.48 kPa^{-1} is higher than widely reported capacitive pressure sensors, whose sensitivity typically range from as low as $\sim$ 0.002[18] to 0.15 kPa^{-1} with texturized dielectric layer prepared using sophisticated microfabrication process.[114] The sensitivity is also comparable with many

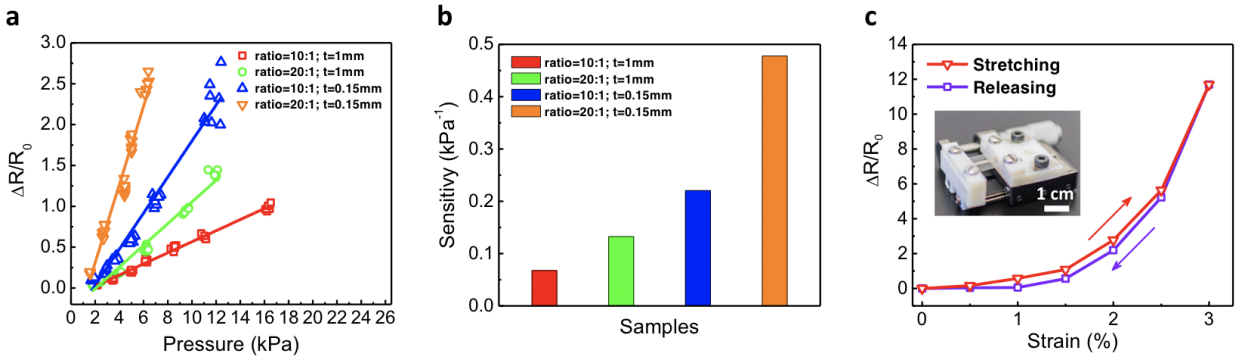

Figure 2.3: Electromechanical characterization of the printed resistive pressure sensor. (a) Relative change in resistance in response to applied pressure for four types of sensors. (b) The sensitivity of each type of sensor extracted from the data in panel (a). (c) Relative change in resistance plotted as a function of tensile strain, where the printed AgNP thin film is manually stretched and released by a linear stretching stage.

previously reported resistive pressure sensors based on various types of sensing materials. In addition, unlike most pressure sensors that exhibit nonlinear response to pressure with the highest sensitivity happening at low pressure range, our printed pressure sensor exhibits a linear pressure response curve throughout its detecting range. In order to con rm that the observed resistance change under pressure is indeed caused by pressure-induced tensile strain, a straight line of AgNP was printed onto PDMS and the sample was mounted on a linear stage for stretching test as shown in Figure 2.3c. The sample was first stretched from 0% to 3% and an increase in $\Delta R/R_0$ of up to 12 (1200%) was observed. Then the sample was gradually released to its relaxed state and the $\Delta R/R_0$ fully recovered to around 0 with almost hysteresis-free resistance-strain characteristic. The stretching test result links the experiment results in Figure 2.3a to the simulation results in Figure 2.2c and explains the working principle of the printed resistive pressure sensor—pressure induces strain, which leads to formation of microcracks in the printed AgNP thin film and consequently increase in its electrical resistance.

The dynamic response and stability of the printed resistive pressure sensor were also studied and the results are presented in Figure 2.4a,b. The pressure was applied automatically using a modified syringe pump shown in Figure 2.4c. Various pressure levels can be applied by controlling the infuse rate, withdraw rate, and target volume in the syringe pump. In this setup, the printed sensor was placed on top of a commercially available force sensor (FSR 402 Interlink Electronics, Inc.) which precisely measures the pressure applied by the loading rod. The device with the best sensitivity (20:1 mixing ratio and 0.15 mm thickness) was used for the dynamic response measurement. Pressure was applied at a frequency of 0.2 Hz and repeated for five times at each pressure level from $\sim$ 1.5 to 6.5 kPa and the corresponding resistance of the sensor was recorded as a function of time. As shown in Figure 2.4a, the $\Delta R/R_0$ exhibits highly reproducible sensing response of about 0.24, 0.6, 1.2, 1.6, and 2.25 at pressure levels of 1.5, 2.8, 4.5, 5.1, and 6.5 kPa, respectively. Figure 2.4b plots one cycle of the dynamic response data, from which the response and recovery times are estimated to be both at around 0.25 s. It is worth noting that our printed sensor exhibits slightly slower response than the commercial force sensor, which is due to the slow recovery characteristics of the PDMS substrate. Except for the longer response time, the data measured from our printed pressure sensor (red trace) closely tracks the data from the reference force sensor indicating the reliability of our device for practical applications. We have also tested the cyclic durability of the sensor by repeatedly applying a pressure of 1.5 kPa at a frequency of 0.1 Hz for up to 1000 cycles and long-term stability of the sensor by measuring the response curve of same device after 5 months. In both cases, the sensor response remained almost unchanged.

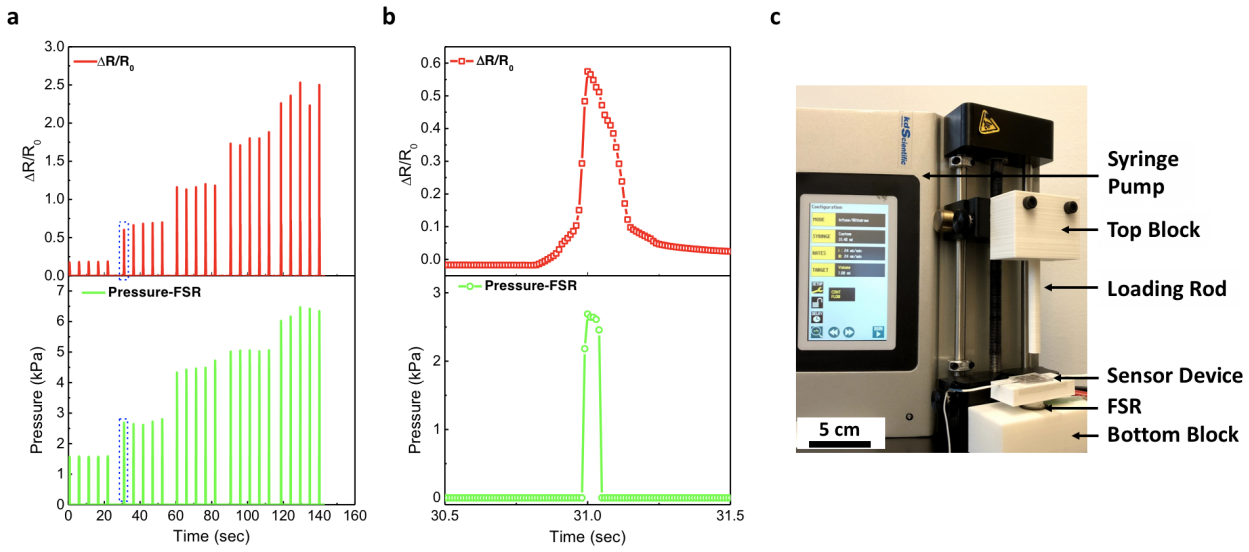

Figure 2.4: Dynamic response test of the sensor under different pressure. (a,b) Plots showing the relative changes in resistance for the pressure sensor with 20:1 mixing ratio and 0.15 mm thickness under dynamic pressure test in a range from 1.5 to 6.5 kPa at a frequency of 0.2 Hz. The red trace shows the resistance change of the sensor and the green trace corresponds to the applied pressure. The data in (b) are a zoomed-in view of the data inside the blue dashed box in panel (a). (c) Photograph showing the experimental setup used for testing the dynamic response of the sensor.

2.4 Applications of Soft Resistive Pressure Sensor Patch

Due to its stretchability, small thickness, and the extremely high pressure sensitivity, our printed resistive pressure sensor is suitable for a wide range of applications such as wearable health monitoring device or sensory system for soft robots. As a proof of concept, we demonstrate two different applications using the printed sensor—a soft microphone patch (Figure 2.5a,c) and a wearable patch for arterial pulse monitoring (Figure 2.5d,f). For the microphone application, a sensor (20:1, 0.15 mm thickness) was placed on a laptop speaker as shown in Figure 2.5c. A prerecorded audio file of a person speaking "Washington University in St. Louis, Electrical and Systems Engineering" was played though the speaker at three different volume set- tings, corresponding to sound pressure levels (SPL) of 95, 80, and 65 dB, respectively. The acoustic response from the sensor ($\Delta R/R_0$) was recorded and plotted in Figure 2.5a. Notably, as the volume increases, the magnitude of the response recorded by the sensor also increases, but the signal waveform remains almost identical as indicated in Figure 2.5b. The signal measured from the printed sensor also closely resembles the waveform from the source file, albeit the sampling rate was much lower at 20 Hz (compared to 44.1 kHz of the source file), which is limited by the step size of 50 ms from the Semiconductor Device Analyzer used during the measurements. The demonstration above indicates the potential of our printed sensor for wearable audio recording device or sounds recognition applications.

Moreover, the high sensitivity and stretchability of the sensor make it also suitable for application as a wearable health monitoring device. The stretchability ensures its ability to conformably attach to human skin and its extremely high sensitivity enables it to record weak signals from the body. Here, we demonstrate that our printed sensor can be used as a noninvasive, real-time arterial pulse measurement patch as shown in Figure 2.5d,c. In order to record the arterial pulse waveform accurately, the sensor was placed on top of the wrist

artery as shown in Figure 2.5f and a wrist band was used to tightly wrap the sensor around the wrist. The recorded pulse waveform shown in Figure 2.5d is periodic and corresponds to a heart rate of 81 bpm. The peripheral artery pressure waves include three waves, the incident wave generated from the ejection of the blood from the heart, the reflected waveform from the upper body region and the reflected wave from the lower body. In Figure 2.5e, the waveform clearly shows the incident peak (P1) and two reflected peaks (P2 and P3). From these peaks, one can determine the arterial stiffness by radial artery augmentation index $\mathrm{AI}_r = \mathrm{P2/P1}$, and the time difference between the first two peaks, $\Delta \mathrm{T}_{vap}$. The measured value from a 25-year-old test person shows $\mathrm{AI}_r \sim 0.45$ and $\Delta \mathrm{T}_{vap} \sim 0.16$, both of which are expected values according to the literature.[115] The ability to accurately measure the arterial pulse waveform makes it possible to further implement our sensor into a real-time blood pressure monitoring device in the future.

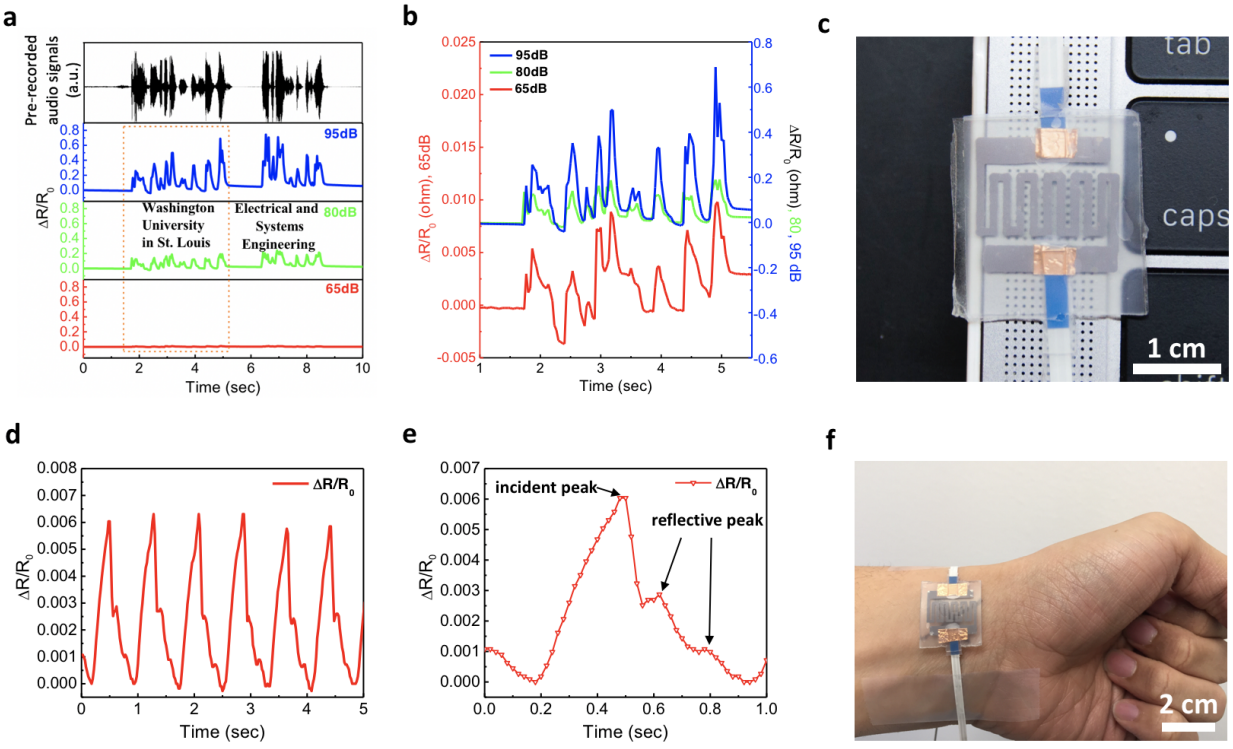

Figure 2.5: Representative applications of the printed resistive pressure sensor. (a,b) Relative change in resistance of the printed pressure sensor in response to acoustic vibrations under various sound pressure levels (SPL) played through a speaker with prerecorded voice (Washington University in St. Louis, Electrical and System Engineering). (c) Photograph showing the experiment setup with the sensor placed directly on a laptop speaker. (d) Arterial pulse waveforms measured from the printed sensor. (e) One cycle of the data in (d) showing the incident peak and re ective peak of the arterial pulse waveform. (f) Photograph of the printed pressure sensor attached on the wrist above the artery for the experiment.

2.5 Summary

In summary, we have demonstrated a printed resistive pressure sensor that is easy to fabricate, soft, lightweight, and with high sensitivity. The sensing mechanism of the sensor including pressure-induced strain, microcrack formation, and effect of substrate stiffness and thickness on the sensor performance has been systematically studied by both simulation and experiments. Due to its high sensitivity, the pressure sensor is able to measure both sound wave and arterial pulse waveform. The sensor platform developed in this work may lead to disposable sensor patches that can be used in future smart wearables and biomedical devices for applications such as real-time blood pressure monitoring.

Chapter 3

Fully Inkjet-Printed Stretchable Conductors

3.1 Introduction

Over the past decade, flexible electronics such as displays, solar cells, and various types of sensors that can retain their performance and functionality while being bent have been explored extensively.[51, 116–121] Flexible sensors for continuous vital sign monitoring and other health care application have also been developed, but these devices are not ideal because the human skin surface is not only flexible but also soft and stretchable.[82, 83, 122–124] Without being able to form intimate contact and conformably adapt to the human skin, the sensors may detach or slide on the skin, resulting in motion artifact and inaccurate or fluctuating readings. To achieve wearable sensors with more stable signal recording and better wearing comfort, soft electronic devices that are stretchable and have the ability to accommodate large strain and deformations while maintaining their electrical performance

have attracted significant attention. Progress has been made in demonstrating soft electronics for applications in artificial electronic skin, soft robotics, and wearable sensors.[16, 98, 106, 125–129]

A stretchable conductor is one of the key components for implementing soft electronics, and there are a few approaches to achieve stretchable conductors. The first is to use conventional metal thin films but pattern them into buckling, wavy, or serpentine-shaped patterns that are structurally stretchable.[130–132] This approach utilizes conventional micro- fabrication processes that are highly reliable and typically results in great electrical performance, although the sample is sometimes limited to small or medium sizes due to the constraints in microfabrication tools. The second approach is to develop intrinsically stretchable composite materials by adding conductive fillers such as carbon nanotubes (CNT),[42, 133] metal nanoparticles, or metal nanowires[134–137] into elastomers such as polydimethylsiloxane (PDMS). Such composite materials generally offer good stretchability, but the use of an insulating polymer matrix could result in either low conductivity or significant conductivity change under mechanical deformation. An alternative method for achieving an intrinsically stretchable polymer is to blend a soft polymer or plasticizer into conducting polymers that may soften the polymer chain and thus increase the free volume, resulting in a low modulus material. For example, it has been reported that the widely used conducting polymer poly(3,4-ethylenedioxythiophene) polystyrene sulfonate (PEDOT:PSS) can be made stretchable by blending in poly(ethylene glycol) (PEG), poly(vinyl alcohol) (PVA), polyurethane (PU), or Zonyl.[12, 14, 46, 138–141] Such polymer blends are solution processable and can be made into large-area conductive thin films for stretchable electrode applications using low-cost processes such as spin coating.[14, 138]

To achieve high-resolution patterning of the solution-based stretchable conducting polymer, printing methods such as inkjet printing can be used.[142–146] However, one challenge is that

most of the soft polymer additives with high molecular weights are often too viscous. To make the ink suitable for inkjet printing, the viscosity needs to be lowered and its surface tension needs to be adjusted for optimal wetting on elastomer substrates. The above can be achieved by diluting the polymer with appropriate organic solvents.[147, 148] In this work, we have systematically studied the effect of adding polar solvents on the most commonly used water-soluble conducting polymer PEDOT:PSS, where PEDOT with positive charges and insulating PSS with negative charges stabilized the PEDOT configuration by columbic attractions.[149] Our study on the electrical properties of PEDOT:PSS mixed with various type of polar solvents have shown that the best conductivity can be achieved by adding ~ 5 wt % ethylene glycol (EG).

To achieve stretchability, we have formulated an ink recipe by dissolving the polymer poly(ethylene oxide) (PEO) in N,N-dimethylformamide (DMF) to reduce its viscosity and then mixing with the PEDOT:PSS solution that can decrease the interaction between polymer chains and increase the free volume between PEDOT and PSS grains to make a highly stretchable ink with low sheet resistance.16 After being patterned using inkjet printing, thin films of an intrinsically stretchable PEDOT:PSS/PEO polymer blend exhibit a low sheet resistance of 84 $\Omega/\square$ and a high stretchability of up to 50%. In addition to its high stretchability and conductivity, the PEDOT:PSS/PEO polymer blend is also biocompatible and can be made into wearable sensor patches for health monitoring applications.[150–153] As an example, we have demonstrated an inkjet-printed sensor patch on a PDMS substrate for recording vital signs including electrocardiography (ECG) and photoplethysmography (PPG). Unlike traditional Ag/AgCl electrodes with a conducting hydrogel between the skin and electrodes, the printed PEDOT:PSS/PEO polymer blend not only is stretchable but also can be used as dry electrodes that can be directly placed on the skin surface without the use of a conducting hydrogel. In the PPG monitoring application, the printed PEDOT:PSS/PEO

is used as stretchable interconnects for connecting a surface-mounted light-emitting diode and a photodetector. The printed sensor patch can simultaneously and continuously record ECG and PPG waveforms for monitoring the heart rate, blood oxygen, and cardiac cycles. It serves as a proof-of-concept demonstration to show the potential of using a printed stretchable conducting polymer in low-cost wearable sensor patches for smart health applications.

3.2 Materials, Fabrication Process and Characterization

3.2.1 Materials

Poly(3,4-ethylenedioxythiophene)-poly-(styrenesulfonate) (1.1% in H_2O, surfactant-free, high-conductivity grade), ethylene glycol (EG) (anhydrous, 99.8%), dimethyl sulfoxide (DMSO) (anhydrous, $\geq$ 99.9%), N,N-dimethylformamide (DMF) (anhydrous, 99.8%), glycerol (99.5%), poly(ethylene oxide) (PEO) (powder, average $M_v \sim$ 5,000,000), and Triton-X 100 (laboratory grade) were purchased from Sigma-Aldrich. Eutectic gallium-indium (EGaIn) was purchased from RotoMetals, and the silver conductive epoxy was purchased from MG Chemicals. Polydimethylsiloxane (PDMS) (Sylgard 184) was purchased from Dow Corning.

3.2.2 Preparation of the PEDOT:PSS/PEO Ink Solution

Polar solvents (EG, DMSO, DMF, and glycerol) from 1, 5, or 10 wt % incorporated with 1 wt % Triton-X 100 as surfactant were added into a surfactant-free PEDOT:PSS aqueous solution. The prepared solution was then stirred at room temperature for 2 h. PEO was first dissolved in DMF to give a concentration of 10 mg/mL. Afterward, 5 wt % ethylene glycol, 1 wt % Triton-X 100, and the desired weight ratio of the PEO solution were then added into the surfactant-free PEDOT:PSS aqueous solution. The solution was then stirred at room

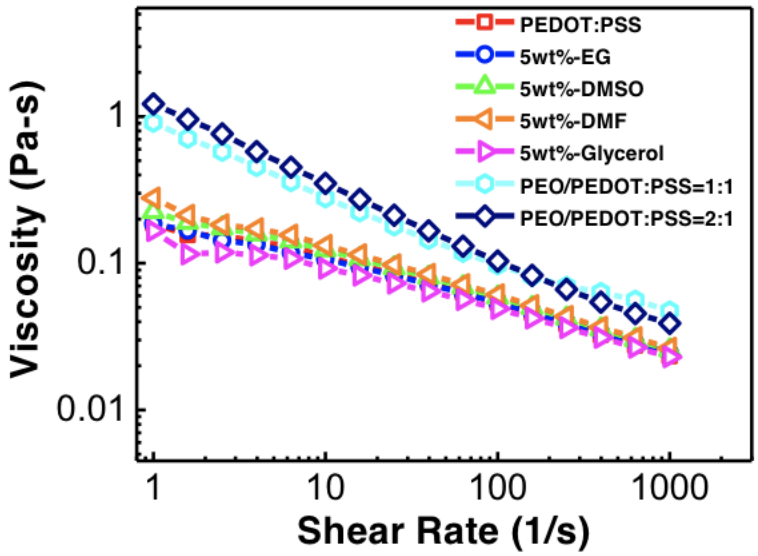

Figure 3.1: Measured viscosity as a function of shear rate for the PEDOT:PSS-based conducting polymer inks with various types of additives.

temperature for 3 h. The weight fraction of each solvent or additive was calculated from the additive weight divided by the total weight of the solution.

3.2.3 Fabrication Process of the PEDOT:PSS Thin Film on PDMS via Inkjet Printing

The PDMS substrate was pretreated by oxygen plasma at 30 W for 15 s. The as-prepared PEDOT:PSS or PEDOT:PSS/PEO solution was then printed onto the treated PDMS substrate using a GIX Microplotter (Sonoplot Inc.) with nozzle openings of 50−400 μm. After printing, the samples were placed on a hot plate and annealed at 120 °C for 15 min. Due to the high boiling point of glycerol, the sample of PEDOT:PSS with 5 wt % glycerol additive was annealed at 150 °C for 60 min. To investigate the printability and optimize the printing results, we have systematically studied the rheological properties and surface tension of various ink formulations, and the results are shown in Figure 3.1.

3.2.4 Characterization of the Printed PEDOT:PSS Thin Films

The width (W) and length (L) of the inkjet-printed PEDOT:PSS thin films were measured by an optical microscope (Olympus BX53M). A semiconductor device analyzer (Keysight B1500A) was used to measure the electrical resistance (R) of the printed feature. The sheet resistance (Rs) was calculated with Rs = R/(L/W). The thickness and microstructure of the thin films were measured and captured by an environmental scanning electron microscope (Thermofisher Quattro S ESEM) and an atomic force microscope (Bruker Dimensions ICO AFM). The cyclic stretching test of the thin films was performed on a modified syringe pump with 3D-printed clamps. Eutectic gallium-indium (EGaIn) was placed on both ends of the thin film and connected with copper wires to the semiconductor device analyzer (Keysight B1500A) to acquire the sheet resistance (R_s).

Figure 3.1 shows the viscosity as a function of shear rate for the PEDOT:PSS-based conducting polymer inks with various types of additives. The viscosity was measured (Rheometer, TA Instruments AR G2) at the shear rate from 1 to 1000 s^{-1}. The results show typical non-Newtonian behavior of the PEDOT:PSS solution with decreasing viscosity for increasing shear rates.[144, 154] For the pristine PEDOT:PSS ink, the viscosity is 0.1863 Pa-s at a shear rate 1 s^{-1} and the viscosity drop to 0.02327 Pa-s at a shear rate 1000 s^{-1}. The PEDOT:PSS solution mixed with 5 wt % of EG, DMSO DMF and glycerol all exhibit similar behavior compare with pristine PEDOT:PSS ink. Moreover, the PEDOT:PSS mixed with 5 wt % EG and 50 wt % PEO (PEO/PEDOT:PSS = 1:1) or 5 wt % EG and 66 wt % PEO (PEO/PEDOT:PSS = 2:1) exhibit higher viscosity compared to the one without PEO under all shear rates tested. The result may be attributed to the high molecular weight of PEO. At a shear rate of 1000 s^1, the viscosity of the PEO/PEDOT:PSS mixture exhibit a fairly low viscosity of 0.041 and 0.039 Pa-s for 50 wt % of PEO and 66 wt % of PEO, respectively. Our ink exhibit similar

Table 3.1: Summary of ink formulations and measured properties.

Ink Composition	**Density (kg/m3)**	**Surface Tension (J/m^2)**	**Nozzle Diameter (m)**	**Viscosity (Pa-s) at shear rate = 1000 (1/s)**	**Ohnesorge Number**
PEDOT:PSS	1020	0.0725	0.0004	0.02327	0.135
PEDOT:PSS + 5wt% EG	1040	0.0706	0.0004	0.02456	0.143
PEDOT:PSS + 5wt% DMSO	1065.33	0.0687	0.0004	0.0256	0.149
PEDOT:PSS + 5wt% DMF	1002.67	0.0653	0.0004	0.02636	0.162
PEDOT:PSS + 5wt% Glycerol	1091.67	0.076	0.0004	0.02294	0.125
PEO/PEDOT:PSS = 1:1	1012	0.054	0.0004	0.04736	0.32
PEO/PEDOT:PSS = 2:1	1030.38	0.0543	0.0004	0.03894	0.26

rheological behavior compared to the viscosity of PEDOT:PSS solution reported previously in the literature.[155, 156] Typically, the inkjet printer has a shear rate greater than 1000 s^{-1} and the printability of the ink is defined by the Ohnesorge number whose value typically lies between 0.1 to 10.[157–160] In Table 3.1, we have systematically measured and provided the detailed information about the ink properties including the ink density, surface tension and the calculated Ohnesorge number. The inkjet printer used in this experiment (The GIX Microplotter, Sonoplot Inc.) is capable of printing inks with viscosity up to 0.450 Pa-s and the calculated Ohnesorge number for all types of PEDOT:PSS solution fall in the range between 0.1 to 10. Therefore, all types of PEDOT:PSS solution in this work are printable by inkjet printing process.

Figure 3.2 presents the UV-vis spectra of inkjet-printed PEDOT:PSS thin film with 5, 10 and 20 print passes. The spectra show the transmittance decreases gradually for increasing number

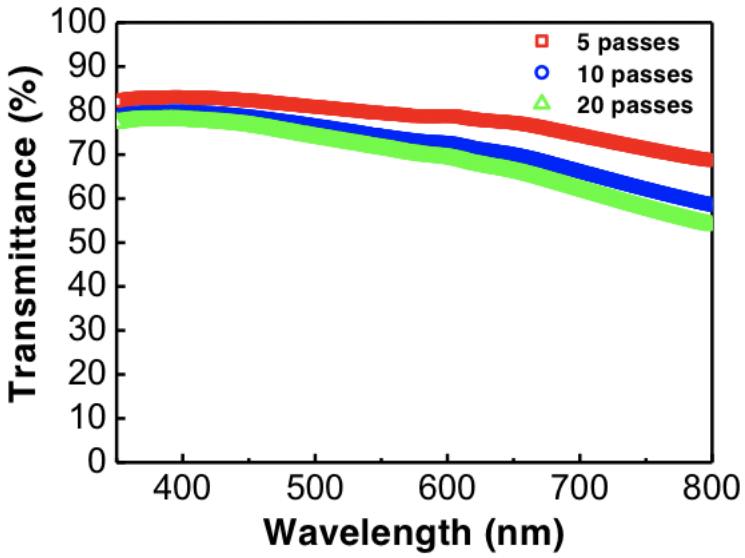

Figure 3.2: UV-Vis spectra of printed PEDOT:PSS thin film with different numbers of printing passes.

of printing passes. The result agree with the photo in Figure 3.4b where the PEDOT:PSS pattern with 20 print passes is the least transparent.

3.2.5 Fabrication and Characterization of the Sensor Patch with ECG and PPG Sensors

The stretchable conductors were prepared using the PEDOT:PSS/PEO solution containing the 50 wt % as-prepared PEO solution (10 mg/mL), 5 wt % ethylene glycol, and 1 wt% Triton-X 100. The solution was then inkjet-printed onto a 0.5 mm thick PDMS substrate pretreated by oxygen plasma (30 W for 15 s) followed by annealing at 120 °C for 15 min. A 3D-printed plastic stencil mask was used for patterning conductive silver epoxy as the binder between stretchable PEDOT:PSS/PEO conductors and other electronic components including light-emitting diode, photodiode, and copper wires. The electrocardiogram was captured by placing three separate PEDOT:PSS/PEO electrodes on the human body (wrist,

finger, and thigh) and connected to a commercial heart rate monitor IC (AD8232, SparkFun). The photoplethysmography was achieved by pairing a red light-emitting diode (625 nm, XPEBRD-L1-0000-00501, Cree Inc.) and a photodiode (PDB-C152SMCT-ND, Advanced Photonix). A 5 V reverse bias was applied to the photodiode, and the photocurrent was recorded using a semiconductor device analyzer (Keysight B1500A). The experiment involving a human subject has been performed with the full, informed consent of the volunteer, who is also the first author of the manuscript.

3.3 Highly Conductive PEDOT:PSS Thin Film Formulation and Characterization

The chemical structures of the conducting polymer PEDOT:PSS; the polar solvents EG, dimethyl sulfoxide (DMSO), DMF, and glycerol; and the soft PEO are shown in Figure 3.3a. PEDOT is the most widely used conducting polymer in the past decade due to its high conductivity, transparency, and stability. The most commonly used commercially available product of PEDOT comes with PEDOT doped with PSS. This aqueous dispersion consisting of PEDOT-rich particles is surrounded by PSS-rich shells, with the negatively charged polyanion (PSS-) stabilizing the positively charged polycation (PEDOT+). The polyanion (PSS-) is an insulator that hampers the charge transport pathway through polycation (PEDOT+) and results in a low electrical conductivity of less than 1 S cm^{-1} in pristine PEDOT:PSS. One of the solutions to improve its conductivity is by adding polar solvents into the pristine PEDOT:PSS aqueous solution to achieve phase separation between PEDOT and PSS grains and the conformational change of the PEDOT chain.[161, 162] The detailed mechanism and experimental results will be discussed later. Despite the increase of conductivity after the addition of a polar solvent, the mechanical properties of the PEDOT:PSS thin film are too

brittle to resist any large deformations. To address the challenge, here we report a method for achieving a printable and stretchable conducting polymer by blending a soft polymer poly(ethylene oxide) (PEO) and EG solvent with PEDOT:PSS. The rearranged microstructure of rigid PEDOT grains and soft PSS/PEO domains would remove the brittleness of PEDOT:PSS and yield a stretchable PEDOT:PSS/PEO polymer blend. As schematically illustrated in Figure 3.3b, such polymer ink can be formulated to the appropriate viscosity to allow it to be directly patterned using the inkjet printing process. To facilitate the wetting of the ink on hydrophobic surfaces such as PDMS, the elastomeric substrate can be pretreated with oxygen plasma. After treatment, the PEDOT:PSS/PEO composite ink can be patterned onto the pretreated PDMS substrate with a feature size as small as 400 μm. More details about the ink formulation and printing process can be found in the experimental section. Figure 3.3c shows a sample with the composite PEDOT:PSS/PEO ink printed on a 0.5 mm thick PDMS substrate. The composite polymer thin film exhibits high stretchability without any crack formation after multiple stretching cycles with tensile strain up to 50%.

While the polar solvent additives can address the low conductivity of pristine PEDOT:PSS, the number of printing passes and consequently the film thickness also play an important role in both the optical and electrical properties of the printed PEDOT:PSS thin film. As shown in Figure 3.4, we have systematically studied the effect of printing passes on the film thickness and the sheet resistance of the printed thin films with various types of solvent additives. The cross-sectional scanning electron microscope (SEM) images taken from the inkjet-printed PEDOT:PSS thin films with 5 wt % EG are shown in Figure 3.4a. With 1, 5, 10, and 20 printing processes, the printed PEDOT:PSS film thickness increases monotonically, which also causes the transparency of the PEDOT:PSS thin film to decrease as shown in Figure 3.4b. The relationship between the film thickness with respect to the printing passes is presented in Figure 3.4c. The thicknesses of 1, 5, 10, and 20 printing passes are measured

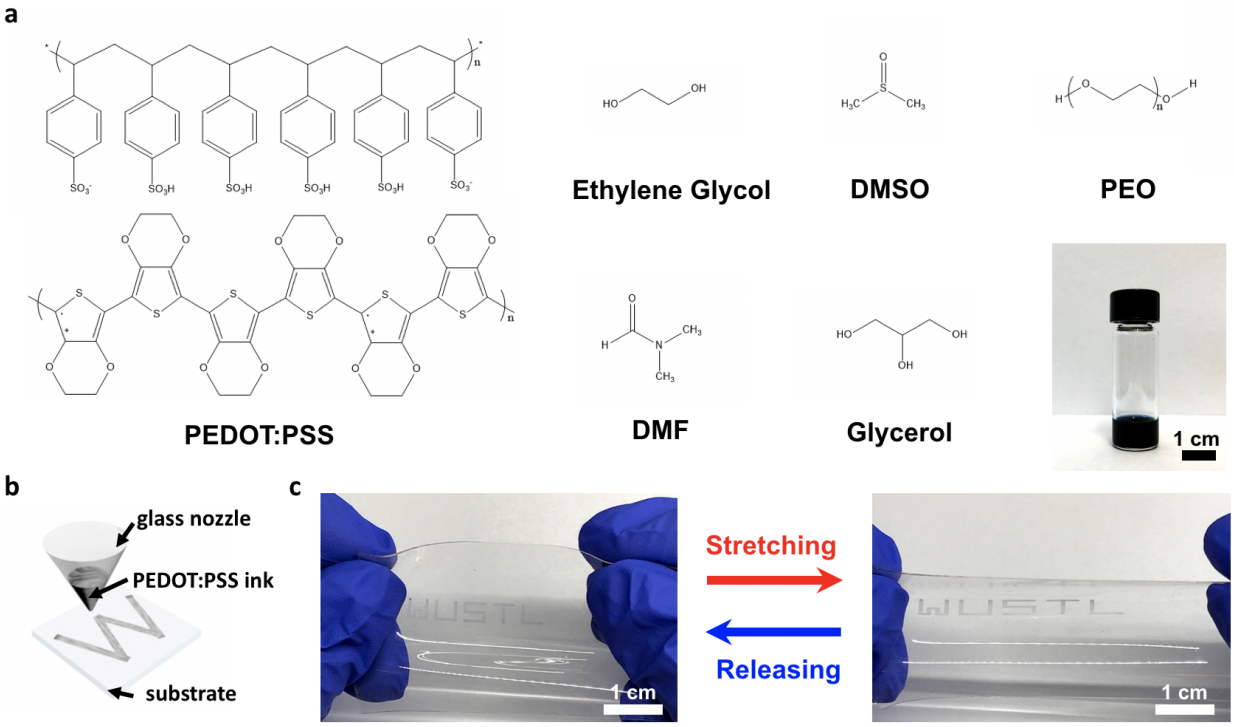

Figure 3.3: (a) Chemical structures of the conducting polymer PEDOT:PSS; the solvents EG, DMSO, DMF, and glycerol; and the soft polymer PEO and a photo of the optimized ink solution containing the composite of PEDOT:PSS, ethylene glycol, and PEO. (b) Schematic diagram showing the inkjet printing process on the elastomer substrate. (c) Photos showing a PDMS substrate with five layers of printed patterns of the conducting polymer in relaxed and stretched states.

to be 0.51, 1.68, 2.84, and 3.9 μm, respectively. The corresponding UV-vis spectra of the inkjet-printed PEDOT:PSS thin film is presented in Figure 3.2.

To determine the best polar solvent additive, we have systematically studied the electrical properties of printed PEDOT:PSS thin films with EG, DMSO, DMF, and glycerol. An amount of 5 wt % of each polar solvent was mixed into a separate surfactant-free PEDOT:PSS aqueous solution (1.1% in H2O, surfactant-free, high-conductivity grade). Additionally, 1 wt % Triton-X was also added into the solution to tune its surface energy for optimal inkjet printing results. After printing, the film was placed on a hot plate and annealed at 120 °C for 15 min. The comparison of sheet resistance for various solvent additives with different numbers of printing passes is shown in Figure 3.4d. As expected, the data from the solvent-free PEDOT:PSS aqueous ink exhibit the highest sheet resistance of $\sim$ 6.2 k$\Omega/\square$ with a single pass printing. Other films with polar solvent additives show significantly lower sheet resistance, with 5 wt % EG exhibiting the lowest sheet resistance of $\sim$ 355 $\Omega/\square$. The samples with 5 wt % DMSO, 5 wt % DMF, and 5 wt % glycerol exhibit sheet resistance values of 767, 1914, and 2371 $\Omega/\square$, respectively. The results above indicate that polar solvents are indeed effective in improving the electrical property of the PEDOT:PSS. To reach an even lower sheet resistance, the number of printing passes can be increased. With 20 passes, the sample with 5 wt % EG additive exhibits the lowest sheet resistance of 58 $\Omega/\square$ and the one with 5 wt % DMSO exhibits the second lowest sheet resistance of 72 $\Omega/\square$. Furthermore, according to Figure 3.4d, both EG and DMSO additives are effective in lowering the sheet resistance of PEDOT:PSS. To have a better understanding of both additives and find the optimal ink composition, we have also compared the sheet resistance of PEDOT:PSS inks with different amounts of solvent additives ranging from 0 to 10 wt % as shown in Figure 3.4e. The results show that the PEDOT:PSS thin films with 1 wt % DMSO exhibit a slightly lower sheet resistance of 61 $\Omega/\square$ compared to 68 $\Omega/\square$ from the sample with 1 wt % EG. As the solvent content increases

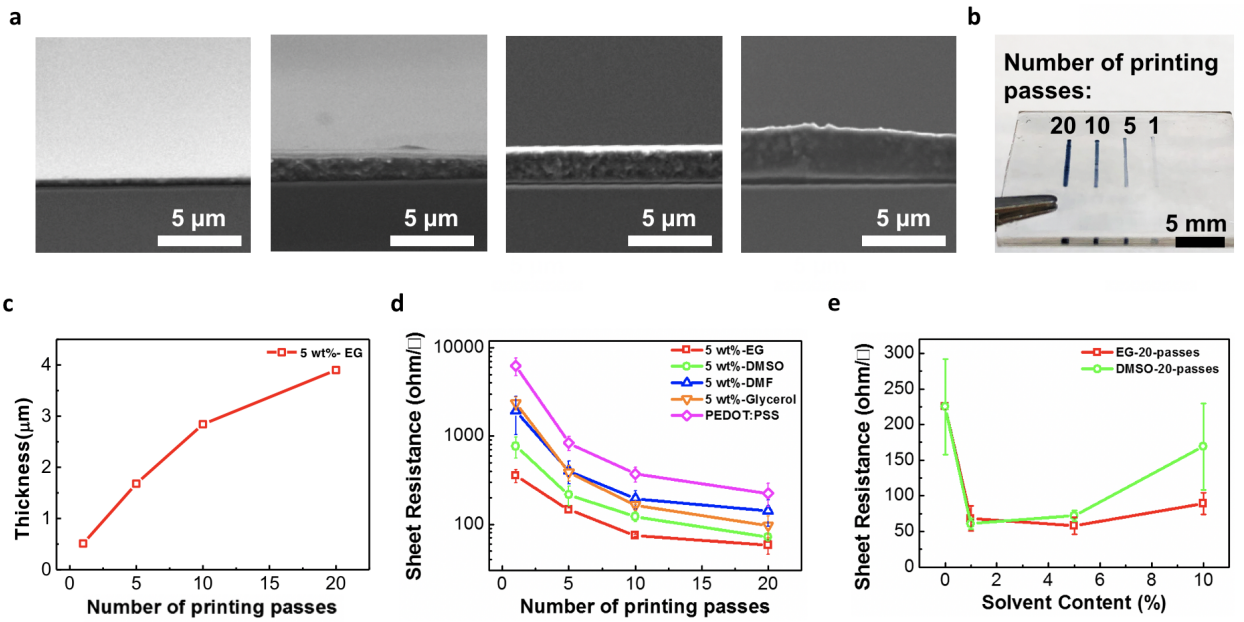

Figure 3.4: (a) SEM images showing the thickness of the inkjet-printed PEDOT:PSS thin film with 5 wt % EG after 1, 5, 10, and 20 print passes (from left to right), respectively. (b) Photograph of the inkjet-printed PEDOT:PSS thin film on PDMS with various numbers of print passes. (c) Thickness of the inkjet-printed PEDOT:PSS thin film with 5 wt % EG vs the number of print passes. (d) Comparison of the sheet resistance between the pristine PEDOT:PSS ink and PEDOT:PSS mixed with 5 wt % of various types of polar solvent additives after various numbers of print passes. (e) Comparison between the sheet resistance of the PEDOT:PSS thin film with EG or DMSO additives with various amounts of polar solvent content from 0, 1, and 5% to 10%.

to 10 wt %, samples with both types of additives show inferior performance compared to 1 and 5 wt %. The optimal ink formulations for DMSO and EG were obtained at 1 and 5 wt %, respectively. However, because the one with 5 wt % EG exhibits the lowest sheet resistance among all experimental conditions, we have chosen this as the optimal ink formulation for further experiments.

3.4 Stretchable PEDOT:PSS/PEO Thin Film Formulation and Characterization

The decrease in sheet resistance in the printed PEDOT:PSS thin film with the EG additive can be attributed to the morphology change of the PEDOT and PSS grains. High-resolution topography and phase images of the surface of the printed PEDOT:PSS thin films obtained using atomic force microscopy (AFM) are shown in Figure 3.5a,b. It has been reported that PEDOT and PSS grains can be differentiated by using AFM phase images,[163] where the dark regions correspond to soft materials and the bright regions correspond to more rigid polymers. In the PEDOT:PSS thin film, PSS is considered as a softer polymer and PEDOT is considered to be more rigid.[141] Figure 3.5a shows the height image of the pristine PEDOT:PSS thin film with a root-mean-square roughness of 1.7 nm, and the phase image indicates that small PEDOT grains are surrounded by small PSS grains. These insulating PSS grains hinder the carrier transport and impede the charge hopping with a discontinuous conducting pathway of PEDOT that results in a less conductive film. With the addition of EG, the PEDOT and PSS grains rearrange with thermal annealing, which separates the PEDOT grains from PSS grains as shown in Figure 3b. The microstructure of the thin film is more percolated due to the aggregation of the PEDOT grains (the brighter region in the phase image), and this percolating network could aid the charge hopping along the chain that leads to a more conductive film. The effect of the aforementioned morphology change with the help of a polar solvent is schematically illustrated in Figure 3.5c,d.

Although the thin film of PEDOT:PSS with the EG additive exhibits superior sheet resistance, the film is still unable to resist any significant deformation. When a large tensile strain (greater than 25%) is applied, the sheet resistance of the film will increase over 250% due to the formation and propagation of microcracks. To make the conducting polymer stretchable,

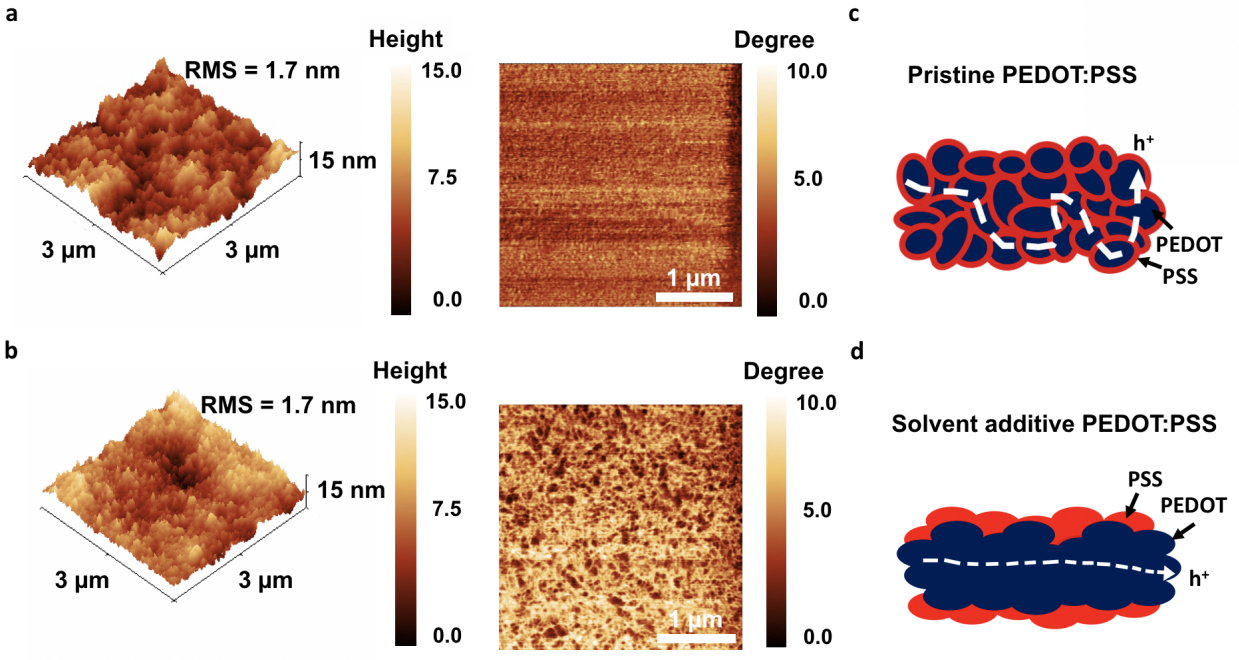

Figure 3.5: Morphology of the pristine PEDOT:PSS and PEDOT:PSS thin films with 5 wt % EG. Height and phase images of printed thin films of (a) PEDOT:PSS and (b) PEDOT:PSS with 5 wt % EG obtained with tapping-mode AFM. (c) Schematic illustration of the hole transport in the pristine PEDOT:PSS thin film. (d) Schematic illustrating the PEDOT:PSS phase separation and structural rearrangement after the addition of EG.

one possible way is to add soft polymer blends or plasticizers to decrease the interaction between polymer chains and increase the free volume between PEDOT and PSS grains.[164] Previous literature has shown that adding a soft polymer such as PEG, PVA, PDMS, or PU into PEDOT:PSS to form polymer blends can effectively decrease the Young's modulus and increase the elongation at break.[14, 138, 139, 165, 166] While this approach could result in the desired elasticity, the PEDOT:PSS polymer blends may also experience a decrease in electrical conductivity due to the insulation of these soft polymers. Moreover, some soft polymers such as PDMS are intrinsically hydrophobic and may be difficult to mix uniformly in the aqueous PEDOT:PSS solution, and its high viscosity also makes it challenging to fabricate high-resolution patterns through inkjet printing. In this work, we have selected the water-soluble soft polymer PEO as the polymer filler that can effectively encompass the brittle PEDOT and soft PSS grains.[167] In addition to making the PEDOT:PSS film stretchable, PEO can also facilitate the phase separation of PEDOT and PSS grains to form a more conductive network of PEDOT grains, which can offset the decrease in electrical conductivity due to the addition of insulating fillers. Unlike the solvent additives described above, PEO remains in the printed PEDOT:PSS thin film even after annealing at elevated temperatures. The hydroxyl groups on PEO may form strong hydrogen bonds with the sulfonic groups on PSS, thereby weakening the interaction between PEDOT and PSS chain and thus forming a more connective PEDOT network.[168] As a result, adding PEO into PEDOT:PSS and EG can result in highly stretchable thin films while maintaining its electrical performance.

We have compared the structure change of thin films of PEDOT:PSS with the EG additive before and after adding PEO. The thin films were inkjet-printed onto the PDMS substrate followed by thermal annealing at 120 °C for 15 min, and the samples were then mounted on a linear stage for the stretch test. Figure 3.6a shows the optical micrographs of printed thin films of PEDOT:PSS with 5 wt % EG in its relaxed state (left) and when being stretched to

50% (right). Under 50% tensile strain, the formation of microcracks can be easily seen from the images, which greatly affects the electrical properties of the film. In contrast, according to Figure 3.6b, similar printed thin films of PEDOT:PSS with 5 wt % EG and 66 wt % PEO additives show only minor cracks at the edges of the pattern under the same amount of strain. The SEM image of the PEDOT:PSS thin film with 5 wt % EG and 66 wt % PEO is presented in Figure 3.6c. The image shows the incorporation of crystalline PEO within the PEDOT:PSS thin film. Moreover, AFM images in Figure 3.6d show larger bright regions compared with the phase image in Figure 3.5b, which indicate that the PEDOT grains and the dark regions are soft PEO and PSS. The incorporation of PEO in PEDOT forms a percolation network as expected, which aids the charge transport similar to the effect of polar solvents. However, the decrease in the PEDOT concentration and increase in the PEO content can also negatively affect the electrical property of the PEDOT:PSS/PEO polymer blend. Figure 3.6e shows the sheet resistance of the film with various amounts of PEO. Before adding PEO, the sheet resistance of the PEDOT:PSS thin film with 5 wt % EG is $\sim 58\ \Omega/\square$. With 50 wt % (1:1) or 66 wt % (1:2) of PEO added, the sheet resistance values increase to ~ 84 and $205\ \Omega/\square$, respectively. The results are expected due to the lower percentage of PEDOT presented in the solution and the presence of insulated PEO.

Besides the effect of the PEO additive on sheet resistance, the change in the electromechanical property is also examined through stretch tests and the results are presented in Figure 3.6f. PDMS substrates (0.5 mm thick) with printed PEDOT:PSS or PEDOT:PSS/PEO thin films were mounted on a linear stage, and liquid metal (EGaIn) droplets were placed on both ends of the films for measurement purposes. The electrical measurements were performed after the fresh samples were first stretched for 20 cycles. The PEDOT:PSS sample without PEO exhibits a poor mechanical property with the sheet resistance increasing by 20% ($\Delta R/R_0 = 0.2$, where ΔR is the change in sheet resistance and R_0 is the sheet resistance in the

relaxed state) when the film is stretched by 10%. Moreover, the sheet resistance increases dramatically by 250% ($\Delta R/R_0 = 2.5$) under 25% tensile strain. In contrast, for the samples with 50 or 66 wt % PEO additives, under 10% tensile strain, the sheet resistance increases by only 9 or 1%, respectively. As the tensile strain increases to 50%, the sample with 50 wt % PEO additive experienced a 41% increase in sheet resistance, while the one with 66 wt % PEO additives only rose by 18%. We have also studied the electrical properties of the PEDOT:PSS/PEO thin film when stretched in the transverse direction, and the data are presented in Figure 3.7. The results clearly show that the PEO additive is very effective in rendering the PEDOT:PSS film stretchable. The stability of the PEDOT:PSS/PEO polymer blend under cyclic stretch tests was also studied, and the results are presented in Figure 3.6g. The samples with the PEDOT:PSS/PEO polymer blend were repeatedly stretched to 50% tensile strain for 1000 cycles, and $\Delta R/R_0$ remained almost unchanged at 42 or 20% for the samples with 50 or 66 wt % PEO, respectively.

In both ink formulations, the PEDOT:PSS/PEO polymer blends show good stability and compliance to mechanical strain without significant sacrifice in electrical performance. Although the ink with 66% of PEO offers the best stretchability, the sheet resistance is also much higher compared to the one with 50% of PEO. For wearable electronics applications, the human skin surface normally experiences no more than 30% tensile strain.[169] As a result, it is a good tradeoff to choose the formulation with 50 wt % PEO additive.

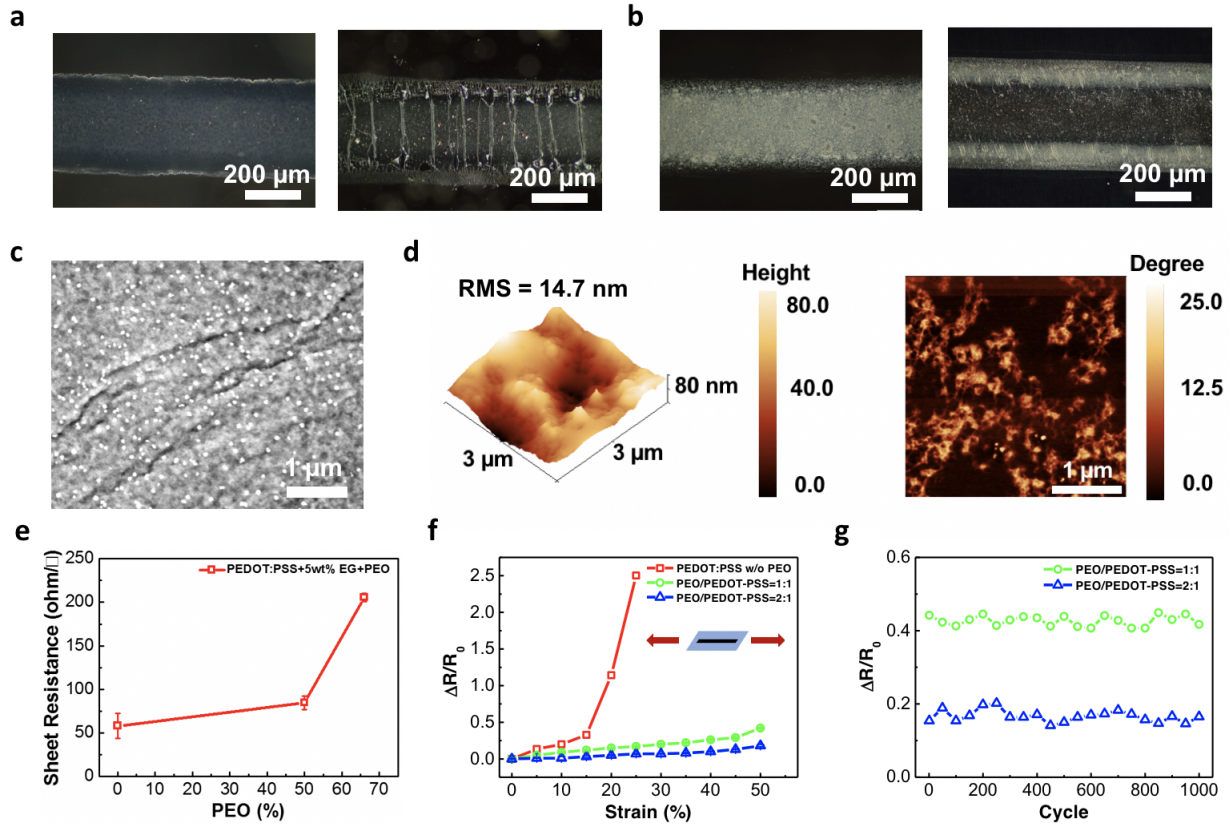

Figure 3.6: (a) Optical micrographs of printed thin films of PEDOT:PSS with 5 wt % EG under 0% (left) and 50% (right) of tensile strain showing the propagation of microcracks and structural failure when the film is stretched. (b) Optical micrographs of printed thin films of PEDOT:PSS with 5 wt % EG and 66 wt % PEO under 0% (left) and 50% (right) of tensile strain indicating that significantly fewer cracks appear in the thin film. (c) SEM image showing the microstructure of the PEDOT:PSS thin film with 5 wt % EG and 66 wt % PEO. (d) Tapping-mode AFM height and phase images showing the surface morphology of the PEDOT:PSS thin film with 5 wt % EG and 66 wt % PEO. (e) Sheet resistance of the inkjet-printed PEDOT:PSS thin film with 5 wt % EG and various amounts of PEO. (f) Relative change in resistance plotted as a function of tensile strain for the PEDOT:PSS thin film with 5 wt % EG and various amounts of PEO. (g) Electrical property of the PEDOT:PSS/PEO film under the cyclic stretching test with 50% tensile strain.

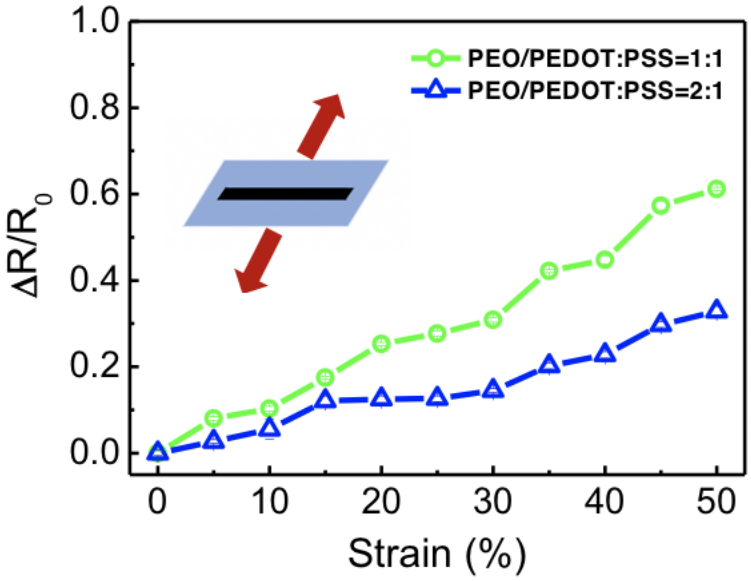

Figure 3.7: Relatively change in resistance as a function of tensile strain when the sample is stretched along the transverse direction.

3.5 Demonstration of PEDOT:PSS/PEO Conductor for Wearable Health Monitoring Applications

The above PEDOT:PSS/PEO composite ink can be processed into intrinsically stretchable electrodes or conductors for wearable electronics and bioelectronic applications. In Figure 3.8, we have demonstrated an inkjet-printed PEDOT:PSS-based soft sensor patch for ECG and PPG recording, allowing users to track the cardiac activity, cardiac cycle, and heart rate simultaneously. The schematic and photograph of the prototype of the integrated soft sensor patch are shown in Figure 3.8a,b. As an exemplary use case, the user may attach the sensor patch on his or her right wrist where one of the printed PEDOT:PSS/PEO electrodes on the backside of the PDMS substrate is in close contact with the skin. One finger from the left hand can then be placed on top of another ECG electrode on the front side of the PDMS substrate, and the other finger can be placed on the PPG sensor comprising a red light-

emitting diode (LED) and a photodiode (PD) (Figure 3.8c). Demonstration of the PPG recording is represented in Figure 3.8d-f, where the printed PEDOT:PSS/PEO film serves as stretchable interconnects between rigid circuit components (surface-mounted LED and PD). The PPG sensor can be used in both reflectance and transmission modes (Figure 3.8f). In the reflectance mode, the red LED and PD are placed on the same side of the finger. Due to the fact that blood absorbs more light than surrounding tissues, the small variations in the volume change between systolic and diastolic phases can be observed by the intensity change of backscattered light reaching to the photodiode.[170] In addition to the reflectance mode, the soft sensor patch can also be wrapped around the fingertip and transformed into a transmission mode PPG. The red LED is now located at the fingernail, whereas the PD is placed at the bottom of the fingertip. The photodiode then detects the intensity of the transmitted light through the tissue and blood vessel. Both modes of the PPG recordings provided valuable signals of the heart rate and cardiovascular system activity. Both modes of PPG waveforms were recorded and are presented in Figure 3.8d,e. The waveforms show clear periodic peaks that correspond to a heart rate of 72 bpm. The printed stretchable PEDOT:PSS/PEO polymer blend can also be used as a dry electrode for ECG recording applications, and the results are presented in Figure 3.8g-i. The PEDOT:PSS/PEO electrodes were inkjet-printed on both sides of the PDMS substrate with one electrode attached on the user's wrist and another attached to the finger, while a third electrode is placed on the user's thigh and served as a ground electrode. The three electrodes were connected to a commercial ECG monitor IC (AD8232, SparkFun) for data recording. To illustrate that the soft sensor patch can conformably adapt to the skin and the stretchability of the electrodes, two sets of ECG measurements were performed with the wrist flat and bent. Both waveforms in Figure 3.8g are periodic and represent the phases of electrical activity of the heartbeat. The two waveforms closely resemble each other, which demonstrate the stretchability of the PEDOT:PSS electrodes without mechanical or electrical failure under applied strain in a

bent wrist. In Figure 3.8h, the recorded ECG waveforms exhibit clearly distinguishable QRS interval and T waves in which the QRS complex represents ventricular depolarization and the T waves reflect the ventricular repolarization.[171] These signals can be further used to detect cardiovascular diseases, such as arrhythmias and myocardial infarction.[172, 173]

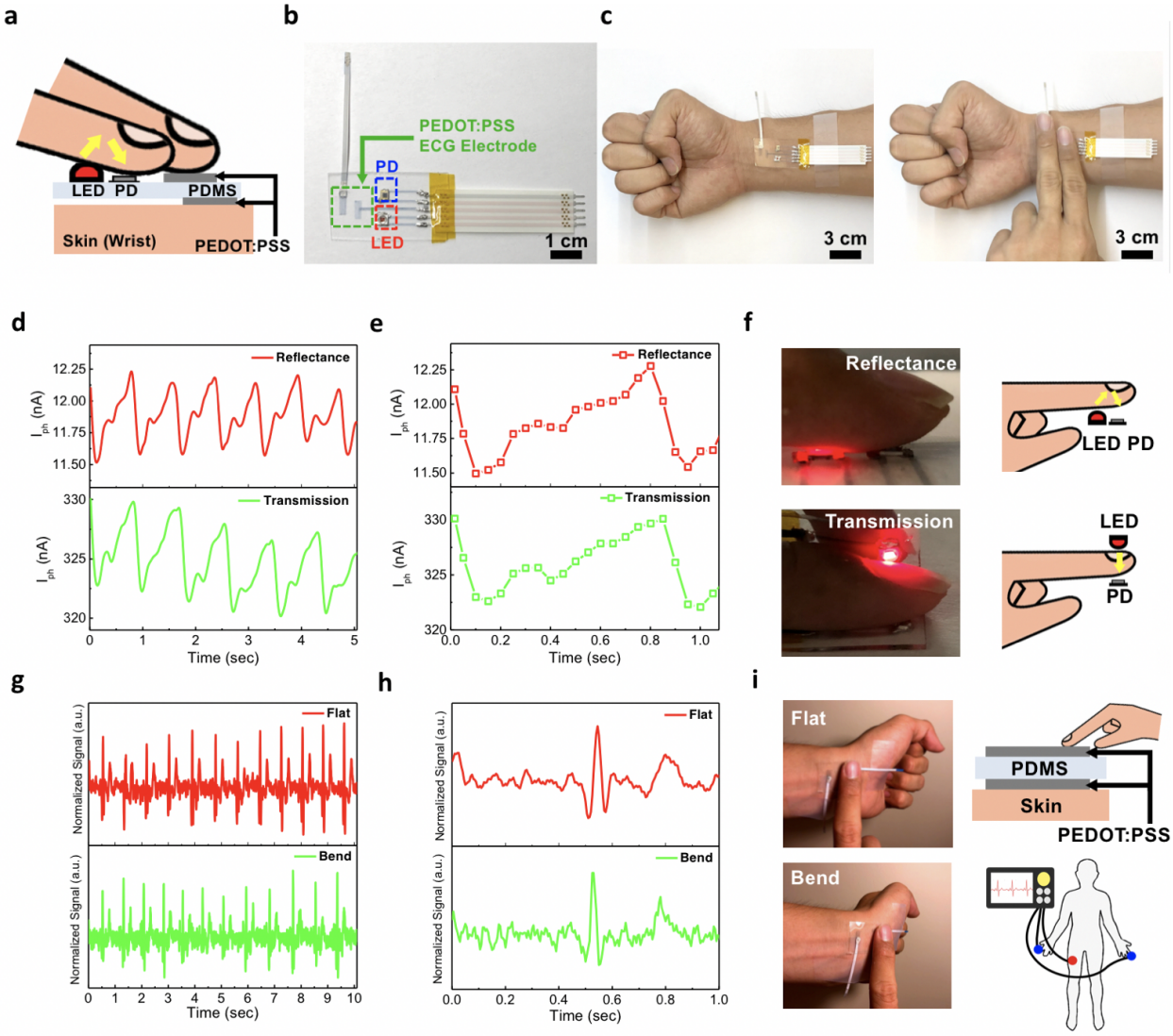

Figure 3.8: Representative applications of the printed stretchable PEDOT:PSS/PEO conductor for wearable electrocardiography (ECG) and photoplethysmography (PPG) sensors. (a) Schematic diagram of a PDMS patch with integrated ECG and PPG sensors for simultaneous recording of both physiological signals. (b) Photograph of the sensor patch with integrated ECG and PPG sensors. (c) Photograph showing the placement of the sensor patch on a human body for ECG and PPG recording. (d, e) PPG waveforms measured with 625 nm LED illumination using both reflective and transmission modes. (f) Photographs showing the experimental setup for reflectance and transmission mode PPG measurement. (g, h) ECG signals measured with printed PEDOT:PSS/EG/PEO electrodes. (i) Photographs and schematics showing the ECG electrode placement on the skin surface during the ECG measurements.

3.6 Summary

In summary, we have developed an inkjet-printable and stretchable PEDOT:PSS/PEO polymer blend with PEO to help improve elasticity and a polar solvent to help improve electrical conductivity and tune the ink rheology. Using the optimal ink formulation and printing recipe, printed thin films with a low sheet resistance of 84 $\Omega/\square$ that can resist up to 50% tensile strain for thousands of cycles have been achieved. We have further demonstrated that the stretchable polymer blends can be used as printed interconnects and electrodes to form an ultrathin wearable sensor patch for PPG and ECG monitoring applications. In particular, PPG was demonstrated in both reflectance and transmission mode, and the recorded signal clearly shows the pulsatile nature of blood in the tissue with indication of periodic systolic and diastolic peaks. The ECG waveforms collected from the polymer electrodes represent the activity of the ventricle during different phases of heartbeats. The highly elastic conductive material and lightweight soft sensor patch developed in this work may lead to low-cost wearables for vital sign and cardiovascular disease monitoring and various other smart connected health applications.

Chapter 4

Stretchable Sponge Electrodes for Long-Term and Motion-Artifact-Tolerant Recording of High-Quality Electrophysiologic Signals

4.1 Introduction

Soft electronic devices and sensors[154, 174–179] built using elastic materials or structures can maintain electrical performance and reliability under tension or bending conditions, and they have found a wide range of applications in wearable health monitoring devices,[3, 45, 51] resorbable medical implants,[180, 181] human-machine interfaces,[182, 183] and many more. Among the various applications above, clinical or ambulatory monitoring of electrophysiologic signals is a widely studied one because the biopotential signals transmitted through human

skin provide abundant information that can be used for early detection, prevention, and diagnosis of various cardiovascular, muscle and brain diseases.

For example, Electrocardiogram (ECG) is a common diagnostic signal for abnormal cardiac rhythms and electrolyte imbalances which can help prevent heart attacks, strokes, and heart disorders.[184, 185] Electromyography (EMG) assesses the health of nerves and muscles to diagnose nerve dysfunction or problems with nerve-to-muscle signaling.[186, 187] Electroencephalography (EEG) monitors brain activity to assess sleep disturbances, brain tumors, and epileps.[188, 189] Moreover, EMG or EEG signals collected by stretchable electrodes have also been used to control the wheelchair for patient with spinal cord injury[190, 191] and prosthetic limb systems for paralyzed patients.[192]

For clinical electrophysiologic signal recording, Ag/AgCl electrodes are still the most commonly used electrodes. Such an electrode consists of a central Ag/AgCl disc and a conductive hydrogel layer that hydrates the non-conductive stratum corneum layer and reduces electrode-skin contact impedance. The commercial Ag/AgCl electrodes do have a few significant drawbacks. First, because the Ag/AgCl electrodes are rigid, they do not conform well to human skin and may result in significant motion artifacts when the patient is active. Second, the Ag/AgCl electrode usually has a small active area and is surrounded by a large area of adhesive or packaging materials that do not contribute to signal collection. Lastly, the conductive gel usually dries within a relatively short period of time (e.g. one hour) on the electrode surface and the signal quality will gradually degrade as the gel evaporates. The issues above make the commercial Ag/AgCl electrode not particularly suitable for wearable and long-term ambulatory monitoring applications.

To overcome the challenges above, significant effort has been made to develop lightweight skin-conformable soft electrodes for biopotential recording. For example, some soft epidermal electrodes reported in the literature are designed to reduce the electrode-skin contact impedance, thereby improving signal quality, while others have designed electrodes that stick to the skin, thereby reducing motion artifacts during body movement.[15, 193–196] One approach is to use microneedles that penetrate the non-conductive stratum corneum layer to reduce the electrode-skin contact impedance. For example, Miura-ori tessellation structured microneedle electrodes fabricated from soft polydimethylsiloxane (PDMS) substrate coated with a titanium-gold metal layer can bend and maintain stable contact with the skin after penetration.[197] 3D-printed microneedle electrodes using medical grade 316L stainless steel can bypass the high impedance stratum corneum and increase the overall electrode surface area.[198] These microneedle electrodes provide stable attachment to the skin and can help obtain reliable ECG and EMG signals. Despite the advantages, there are some safety concerns and debates regarding the use of microneedles due to their invasive nature, which could raise biosafety concerns if the microneedles break into the skin and leave behind materials that could cause redness and skin irritation.[199] Another approach is to pattern the electrodes into biomimetic microstructures to increase the adhesion between the electrodes and the skin, thereby reducing motion artifacts. Grasshopper-inspired microstructured electrodes made of silver microparticles (AgNPs) mixed with PDMS fabricated on a microstructured wafer have low skin-contact impedance and can be applied directly to the skin without skin preparation or external pressure.[200] Inspired by the suction mechanism of octopus suckers, octopus-like polymer masters patterned polyurethane (PU)/multiwalled nanotubes (MWNTs)/silver flakes composite can increase the adhesion between electrodes and skin, and these types of electrodes can make conformal contact even with rough and moist human skin and can withstand bending and twisting conditions.[43] However, these bioinspired approaches typically require a more sophisticated fabrication process to make the mold masters through

photolithography and etching processes. A third approach is to modify the surface properties of the electrode to reduce the electrode-skin contact impedance. For example, the modified gold nanoparticles (AuNPs) thin film on a polyimide (PI) sheet has been shown to increase the surface roughness, resulting in a 1.54-fold increase in surface area compared to the bare sample.[201]

In this work, we demonstrate a soft sponge electrode that can be fabricated in a low-cost and scalable manner and is ideally suited for long-term and motion-artifact-tolerant recording of high-quality biopotential signals. The sponge electrode has a simple structure comprising a porous PDMS sponge that is thoroughly coated with a conductive poly(3,4-ethylenedioxythiophene) polystyrene sulfonate (PEDOT:PSS) layer. With numerous micropores of hundreds of micrometer size inside the sponge, the effective contact area between the skin and the electrode is greatly increased, which leads to a significant drop in skin-electrode contact impedance and an increase in signal-to-noise ratio (SNR). Moreover, compared to conventional planar electrodes, the porous structure of the sponge electrode allows the more conductive hydrogel to be stored within the micropores and thereby slowing down the gel drying time and preventing signal degradation over time, making such electrodes suitable for long recording sessions. The gel within the micropores also serves as a buffer layer to help reduce motion between the electrode and the skin and mitigate motion artifacts. Using such sponge electrodes, we have demonstrated high-quality and robust recording of ECG signals and EMG signals from both skeletal muscle cells (biceps contractions) and smooth muscle cells (uterine contractions). This work shows that our sponge electrodes serve as a viable alternative to commercial Ag/AgCl electrodes or other flexible/stretchable thin-film electrodes for wearable ambulatory biopotential monitoring applications.

4.2 Fabrication Process, Materials Preparation and Structural Analysis

4.2.1 Materials

PDMS (Sylgard 184) was purchased from Dow Corning. PEDOT:PSS (1.3 wt % dispersion in H_2O, conductive grade), PEDOT:PSS (5 wt % conductive screen printable ink), bis(trifluoromethane)sulfonimide lithium salt, ethylene glycol (anhydrous, 99.8%) were purchased from Sigma-Aldrich. A white sugar cube was purchased from C&H.

4.2.2 Preparation of the Porous PEDDOT:PSS/PDMS Electrode

The white sugar cubes 1.5 (W) x 1.5 (L) x 1.5 cm (H) were first placed into various molds to form desired shape and size. The PDMS was prepared by mixing the PDMS prepolymer with the curing agent with a mixing ratio of 10:1 w/w. A vacuum desiccator was used to remove air bubbles from the PDMS liquid. The sugar templates were then dipped into the PDMS liquid for 2 h to let the pores to be fully filled with the PDMS liquid and the sugar templates were subsequently cured in the oven for 3 h at 80 °C. After that, the sugar templates were placed in a hot water bath for 1 h at 100 °C to dissolve the sugar particles and formed the porous PDMS template.

4.2.3 Preparation of the Planar PEDOT:PSS Electrode

The porous PDMS template was pretreated by oxygen plasma at 60 W for 30 s for the top and bottom surfaces to aid the wetting of the ink. 5 wt % of ethylene glycol was added into PEDOT:PSS solution and then stirred at room temperature for 1 h. After that, the porous

PDMS template was then dipped into the as-prepared PEDOT:PSS solution for 30 min. The PEDOT:PSS-coated porous PDMS sponge was then cured in the oven for 3 h at 80 °C.

4.3 Concept of the soft PEDOT:PSS/PDMS sponge electrode

As illustrated in Figure 4.1a, the porous PEDOT:PSS/PDMS sponge can be used as soft wearable electrodes to record high-quality bioelectrical signals owing to its large internal surface area. For example, when two electrodes are placed on the right and left arms, ECG signals showing the electrical activities during the cardiac cycle can be obtained. When two electrodes are attached to the biceps, the EMG signals generated from the electrical activities that occur in response to nerve stimulation of the muscle can be recorded. The fabrication processes of the porous PEDOT:PSS/PDMS electrode are is schematically illustrated in Figure 4.1b, which begins with molding commercially available white sugar cubes into sacrificial templates with the desired sizes and shapes. The sugar templates are then immersed into the liquid PDMS, which then solidifies after curing. The sugar/PDMS templates are subsequently placed in a hot water bath to allow the sugar particles to be dissolved, leaving behind the porous PDMS templates. To facilitate the wetting of the PEDOT:PSS solution onto the hydrophobic PDMS surfaces, the porous PDMS templates need to be pre-treated with oxygen plasma. After treatment, the porous PDMS templates are immersed into the PEDOT:PSS solution followed by annealing of the PEDOT:PSS thin film. After the steps above, the porous PDMS templates are thoroughly coated with a conductive PEDOT:PSS thin film to form the soft sponge electrode. More details about the fabrication processes can be found in the Methods section. The photo and schematic diagram of the sponge electrode are shown in Figure 4.1c and 1d, and its softness is illustrated in Figure 4.2. As shown in

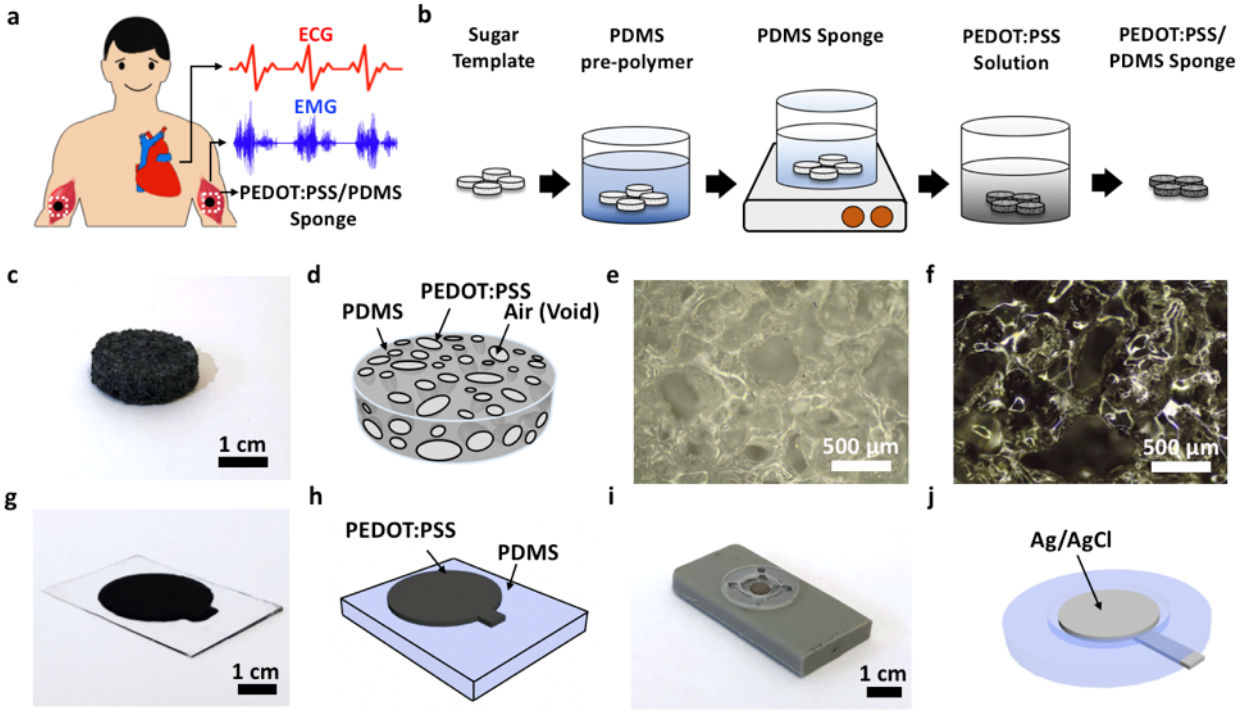

Figure 4.1: Concept of the soft PEDOT:PSS/PDMS sponge electrode. (a) Schematics illustrating the use of the PEDOT:PSS/PDMS sponge electrode for ECG and EMG recording applications. (b) Schematic diagrams illustrating the fabrication steps used to make the sponge electrodes. (c) Photograph of a sponge electrode. (d) Schematic illustrating the structure of the sponge electrode. (e, f) Optical micrographs showing the microstructures of the PDMS sponge (e) before and (f) after the PEDOT:PSS coating. (g, h) Photograph and schematic diagram of the PEDOT:PSS thin-film directly printed on a piece of planar PDMS substrate. (i, j) Photograph and schematic diagram illustrating the structure of a commercial Ag/AgCl electrode used as a gold-standard reference in this study.

the optical micrographs of the PDMS template before (Figure 4.1e) and after (Figure 4.1f) the PEDOT:PSS dip-coating process, the color of the PDMS sponge turns from white to black, confirming that the numerous micropores inside the PDMS template are coated with conductive PEDOT:PSS thin film, allowing the effective surface area of the electrode to be significantly increased. The size of these micropores ranges from 300 - 500 μm, which can be directly controlled by the size of the sugar particle used.

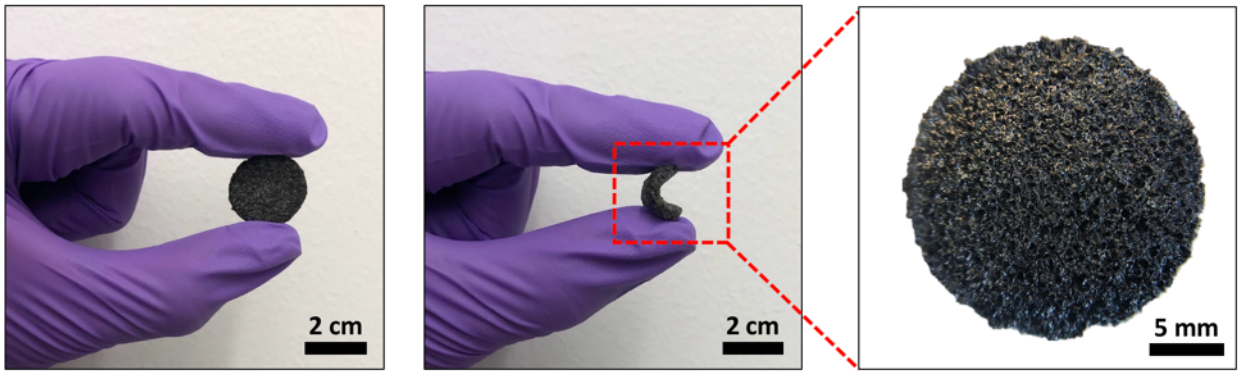

Figure 4.2: Photographs of the porous PEDOT:PSS/PDMS sponge electrode showing its softness and details of the micropores on the surface.

4.4 Electrode-Skin Impedance Analysis

4.4.1 Electrode-skin impedance characterization of the porous PEDOT:PSS/PDMS electrode

In order to thoroughly understand the benefits offered by a porous electrode for wearable and clinical electrophysiologic signal recording applications, we have systematically compared the sponge electrode against the screen-printed planar PEDOT:PSS electrode (Figure 4.1g and h) and the gold-standard commercially-available Ag/AgCl electrode (Figure 4.1i and j). The detailed analysis and comparison of electrode-skin impedance, ECG and EMG signal quality, motion artifacts, and signal decay during long-term recording will be discussed in the following sections. The electrode-skin contact impedance of the sponge electrode was measured by placing two circular-shaped electrodes on the skin surface of the human subject's arm with a separation distance of 5 cm (Figure 4.4). We first investigated the effect of the sponge electrode size and thickness on the electrode-skin impedance. As shown in Figure 4.3a, sponge electrodes with a fixed thickness of 2 mm and a radius ranging from 0.5 cm to 1 cm were fabricated. Figure 4.3b and c are their measured electrode-skin impedance from

10 Hz to 10 kHz without and with the use of conductive hydrogel, respectively. Similarly, sponge electrodes with a fixed radius of 1 cm and different thicknesses ranging from 2 mm to 7.5 mm were also studied (Figure 4.3d) and the corresponding electrode-skin impedance is presented in Figure 4.3e and f. Table 4.1 summarizes the key results and shows how the impedance scales with electrode area and thickness. As the radius/area of the sponge electrode increases, the impedance decreases monotonically, both with and without gel, which is as expected. However, the scaling is not exactly inversely proportional to the area, and it can be attributed to the micropores inside the sponge. For example, as the radius changes from 0.5 to 1 cm, the area of the electrode increases by a factor of 4, but the impedance without gel only decreases from 678.6 to 277.5 kΩ or a factor of 2.45. This is because when there is no conductive gel applied, only the top surface of the electrode contributes to the electrode-skin interface conductance, and those pores on the surface mean not the entire top surface is in contact with the skin, which causes the scaling behavior to deviate slightly from the ideal case. After the sponge electrode was filled with conductive hydrogel, the electrode-skin impedance dropped significantly to as low as 12.2 kΩ at 10 Hz for the sample with a 1 cm radius, corresponding to a 22.7-fold reduction in impedance after gel. The decrease in electrode-skin contact impedance can be attributed to two factors: 1) the drastic increase in effective electrode-skin contact area due to the internal surfaces of the micropores inside the sponge electrode; 2) the penetration and hydration of the conductive hydrogel into the stratum corneum layer - the outermost layer of the epidermis consists of dead skin cells, which are relatively non-conductive due to the lack of water in the cells.[202]

Regarding the thickness of the electrode, ideally, the impedance should increase linearly with thickness for a solid piece of the conductor. On the other hand, the case for a porous conductor is much more complicated as the increases in thickness also lead to a further increase in the effective contact area between the skin and the PEDOT:PSS, which in turn

helps lower the impedance. From the results in Table 4.1, it was observed that the measured impedance is largely independent of the electrode thickness, especially after the conductive gel was applied. The results suggest that while the entire sponge is filled with conductive gel, it is likely that the electrical conduction only happens down to a certain depth, and thus further increase of electrode thickness beyond this depth would not result in more performance gain. We have established a model to estimate the porosity, inner surface area, and expected reduction in sponge electrode impedance and those detailed analysis can be found in subsection 4.4.2. To sum up, the electrode-skin contact impedance is area-dependent but thickness-independent. For the following experiments on ECG and EMG signal recording, we selected the sponge electrode with a radius of 1 cm and a thickness of 2 mm. In order to further illustrate the benefit offered by the porous sponge electrode, we compare it with a screen-printed PEDOT:PSS thin-film electrode on a planar PDMS substrate, as well as a gold-standard BioSemi Ag/AgCl electrode widely used in clinical recording sessions. Figure 4.3g schematically illustrates the advantages offered by a porous electrode compared to conventional planar electrodes. Because the conductive gel soaks up the entire sponge electrode and makes electrical contact with the PEDOT:PSS that is coated on the inner surfaces of the micropores, the skin-electrode contact area is significantly larger compared to a planar electrode, resulting in a decrease in electrode-skin contact impedance. The impedance measurement results in Figure 4.3h confirm the above. Before conductive gel was applied, the measured electrode-skin impedance from the porous PEDOT:PSS electrode and planar PEDOT:PSS electrodes of the same size were 277 kΩ (blue trace) and 247 kΩ (green trace) at 10 Hz, respectively. The impedance from the planar electrode was actually slightly lower than the sponge electrode, which could be attributed to the fact that the bottom surface area of the sponge electrode was only partially in contact with the skin due to the pores resulting in a higher impedance (Figure 4.5). Once the conductive hydrogel was applied, the impedance of both the porous and the planar electrode decreased significantly by a factor of 23 to 12 kΩ

Table 4.1: Effect of the electrode area and thickness on the electrode-skin impedance.

	Area Scaling				**Thickness Scaling**			
Radius (cm)	**0.5**	**0.75**	**1**	**Thickness (mm)**	**2**	**3**	**5**	**7.5**
Area (cm^2)	**0.79**	**1.77**	**3.14**					
Impedance without gel @ 10 Hz (kΩ)	**678.6**	**366.8**	**277.5**		**277.5**	**205.7**	**348.1**	**168.5**
Impedance with gel @ 10 Hz (kΩ)	**80.2**	**33.3**	**12.2**		**12.2**	**17.2**	**17.7**	**14.6**

(red trace), and a factor of 3.9 to 63 kΩ (orange trace), respectively. Compared to the planar electrodes, the use of porous electrodes helps reduce the skin-electrode impedance by a factor of 5.25 at a frequency of 10 Hz. Figure 4.3i summarizes the electrode-skin contact impedance of the porous and planar electrodes at various frequencies, which shows that the drop in impedance after the application of the conductive hydrogel is much more significant in the sponge electrode (blue to red) compared to the planar electrode (green to orange) for all frequencies tested. More importantly, the porous electrode also offers a much lower impedance compared to the commercial Ag/AgCl electrode (80.4 kΩ at 10 Hz according to the dashed line in Figure 4.3h), suggesting the great potential of using the porous electrode for wearable or clinical electrophysiologic signal recording applications. The low skin-electrode interface impedance could lead to improved SNR as will be discussed in the following sections.

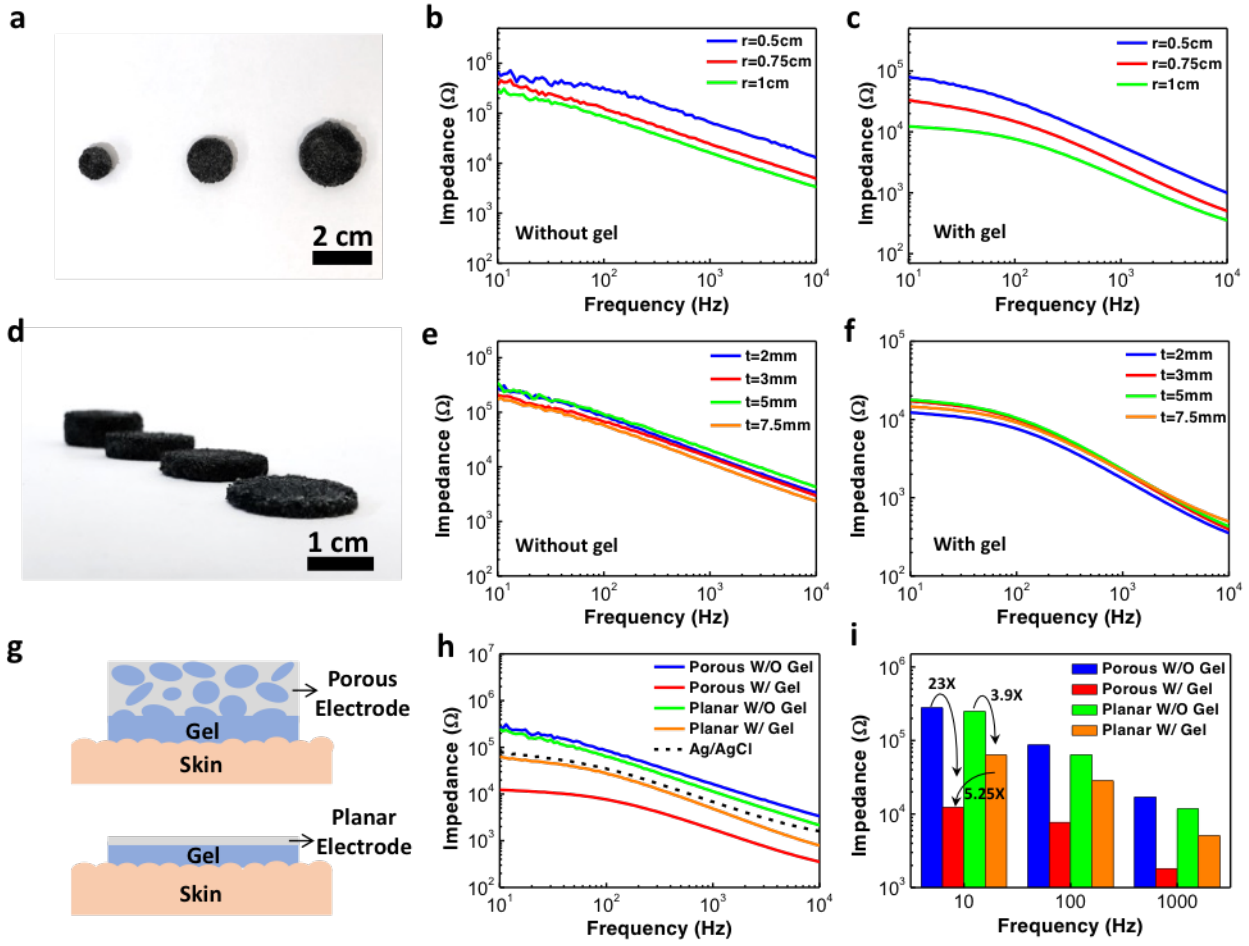

Figure 4.3: Skin-electrode impedance characterization of the porous PEDOT:PSS/PDMS electrode. (a) Photograph showing three sponge electrodes with the same thickness of 2 mm and different radii of 0.5, 0.75, and 1 cm. (b, c) Impedance spectra measured using the sponge electrodes of different radii (b) without and (c) with the use of conductive hydrogel. (d) Photograph showing four sponge electrodes with the same radius of 1 cm and different thicknesses of 2, 3, 5, and 7.5 mm. (e, f) Impedance spectra measured using the sponge electrodes of different thicknesses (e) without and (f) with the use of conductive hydrogel. (g) Schematic diagrams illustrating the difference in the electrode-gel-skin contact area between the sponge electrode and planar electrode. (h) Comparison of impedance spectra measured using the sponge electrode, planar electrode, and commercial Ag/AgCl electrode. (i) Impedance values at 10, 100, and 1000 Hz for the porous electrode and planar electrode with and without the use of conductive hydrogel.

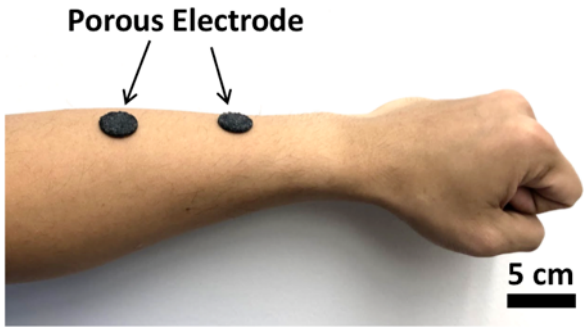

Figure 4.4: Photograph showing the porous PEDOT:PSS/PDMS electrode placement for electrode-skin contact impedance measurement. Two circular electrodes separated by a distance of 5 cm were placed on the volunteer's arm.

Figure 4.5: Schematics illustrating the difference in skin-electrode contact area between the porous electrode and planar electrode when no conductive hydrogel is used. The porous electrode has a typical pore size in the range of 300 – 500 μm and a porosity of 0.6192. When no conductive gel is used, the measured electrode-skin contact impedance is 247 kΩ for the planar electrode, which is slightly lower than the 277 kΩ measured from the porous electrode of the same size. The difference can be attributed to the fact that some micropores in the sponge electrode are only partially in contact with the skin surface, resulting in a slightly smaller skin-electrode contact area compared to the planar electrode.

4.4.2 Analysis of the decrease in electrode-skin impedance and increase in surface area offered by the porous electrode compared to the planar electrode

Calculation of the internal surface area of all micropores inside a porous electrode:

The parameters for porous electrode are listed as below:

Radius: 1cm; Thickness: 2 mm; Porosity: 0.6192; Average pore diameter: 400μm.

$$\text{Total number of micropores inside a sponge electrode}$$

$$= \frac{\text{Volume of an electrode} \times \text{Porosity}}{\text{Volume of a single micropore}}$$

$$= \frac{\pi \times (10^{-2})^2 \times (2 \times 10^{-3}\times) \times 0.6192}{\frac{4}{3}\pi \times (\frac{4\times 10^{-4}}{2})^3}$$

$$= 11610$$

$$\text{Total surface area from the micropores}$$

$$= \text{Total numbers of micropores} \times \text{Surface area of a single micropore}$$

$$= 11610 \times 4\pi \times (2 \times 10^{-4})^2$$

$$= 5.83 \times 10^{-3}\ (m^2)$$

Calculation and comparison of the surface area from a single layer micropores in a porous electrode and the surface area of a conventional planar thin-film electrode:

The parameters for planar electrode is listed as below: Radius: 1cm.

For the sponge electrode, consider only a single layer of micropores filled with conductive gel, calculate the total surface area contributed by these micropores assuming a packing density of 0.8034.[203]

Total surface area of a single layer of micropores

$$= \text{Numbers of pores} \times \text{Packing density} \times \text{Surface area of a micropore}$$

$$= \frac{\text{Cross-sectional area of an electrode}}{\text{Cross-sectional area of a micropore}} \times \text{Packing density} \times \text{Surface area of a micropore}$$

$$= \frac{\pi \times (10^{-2})^2}{\pi \times (2 \times 10^{-4})^2} \times 0.8 \times 4\pi \times (2 \times 10^{-4})^2$$

$$= 1.005 \times 10^{-3}\ (m^2)$$

Total surface area of a conventional planar electrode

$$= \pi \mathrm{r}^2$$

$$= 3.14 \times 10^{-4}\ (m^2)$$

From the calculation above, the internal surface area of the sponge electrode when considering all the micropores inside the sponge electrode is 0.00583 m^2 and the surface area of the corresponding planar electrode with the same size is 0.000314 m^2. The difference in surface area is 18.56 times. On the other hand, if we consider only the first layer of micropores that are in direct contact with the skin (Figure 4.6), then the surface area is 0.001005 m^2 according to total surface area of a single layer of micropores, which is 3.2 times larger than the planar electrode.

According to Figure 4.3h and i in the main paper, the electrode-skin contact impedance of the porous and planar electrodes at 10 Hz are 12 kΩ and 63 kΩ, respectively. Thus, the difference

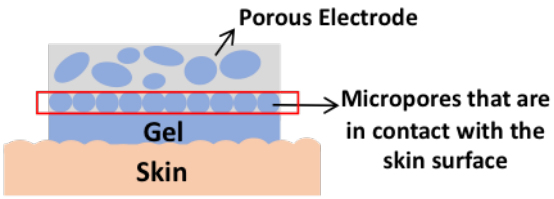

Figure 4.6: Porous electrodes showing the micropores that are in contact with the skin surface

in electrode-skin contact impedance between the porous electrode and planar electrode is 5.25 times, which falls between the values of 18.56 times and 3.2 times above. The above results suggest that not all micropores inside the sponge electrode contribute to the electrode-skin impedance, and it is very likely that only the first few layers of micropores that are close to the skin lead to the observed decrease in impedance. The analysis above also explains why the electrode-skin contact impedance does not scale linearly or even change much as the electrode thickness increases from 2 mm to 7.5 mm.

4.5 Sponge electrode for motion-artifact-tolerant ECG recordings

The porous PEDOT:PSS/PDMS electrode can be used for high-quality electrophysiologic signal recording. As shown in Figure 4.7a, during the ECG experiment, two sponge electrodes filled with conductive hydrogel were used as the signal and reference electrodes and were placed on a volunteer's left and right arms and fastened using antistatic wrist straps. The electrodes were wire-connected to an in-house built data recording unit with a sampling rate of 1 kHz that can either store the recorded data directly into a memory card for optimal power consumption or wirelessly transmit the signal to a computer in real-time. A photograph of the PCB board inside the data recording unit and its block diagram are shown in Figure 4.7b and c, respectively. The recorded signals are first filtered through a differential passive bandpass

filter with a frequency band of 0.1 Hz to 1 kHz to remove unwanted signals. The filtered signal is then amplified by a 60 dB instrumentation amplifier and digitized using a 16-bit analog-to-digital converter, followed by a microcontroller that handles and stores the digital signal into a microSD card. Using the above setup, we measured the ECG signals on the same volunteer, during the same day, and within a relatively short period of time using the porous and planar PEDOT:PSS electrodes and commercial Ag/AgCl electrodes. The recorded data in Figure 4.7d show clear ECG signals from all three types of electrodes with periodic peaks representing the different phases of the electrical activities during a heartbeat. From the period of the ECG waveform, one can estimate the corresponding heart rate to be $\sim$ 75 bpm. Figure 4.7e shows a representative cycle of the ECG waveform measured by the porous electrode, which exhibits a clearly distinguishable P wave that arises from the atrial depolarization, QRS complex that represents ventricular depolarization, and T wave that reflects the ventricular repolarization. These waveforms can be further used to detect cardiac abnormalities and various cardiovascular diseases.[171] As shown previously in Figure 4.3g, because the conductive gel penetrates the micropores inside the sponge electrode to form an intimate electrical contact between the PEDOT:PSS conductive layer and the skin surface, the large internal surface area offered by the sponge electrode and the interfacial layer offered by the gel can also help mitigate motion artifacts. Figure 4.7f shows the recorded ECG waveforms when strong motions (human subject rapid standing up and sitting down) were intentionally introduced during the regions indicated by the orange color. Note that the vertical axis range is from 0 to 4 V, which is significantly greater than the ECG signal amplitude to allow the motion artifacts to be seen. When motions were present, the muscle activities and the movement of the electrode relative to the skin surface resulted in strong voltage spikes exceeding 1 V in the ECG waveforms recorded by both the planar electrodes and the commercial Ag/AgCl electrodes. In contrast, the motion artifacts were significantly mitigated in the waveforms recorded by the porous electrodes, as shown in the blue trace.

Figure 4.7g shows a zoomed-in portion of the data in Figure 4.7f, in which the periodic R-peaks of each ECG waveform are indicated by the black triangle marks. Comparing the three waveforms, one can see that the ECG signals remained visible under the influence of motion artifacts for the porous electrode but disappeared for the planar and Ag/AgCl electrodes, again suggesting that the porous electrode is capable of motion-artifact-tolerant ECG recording, which is crucial for wearable devices and ambulatory electrophysiology recording sessions.

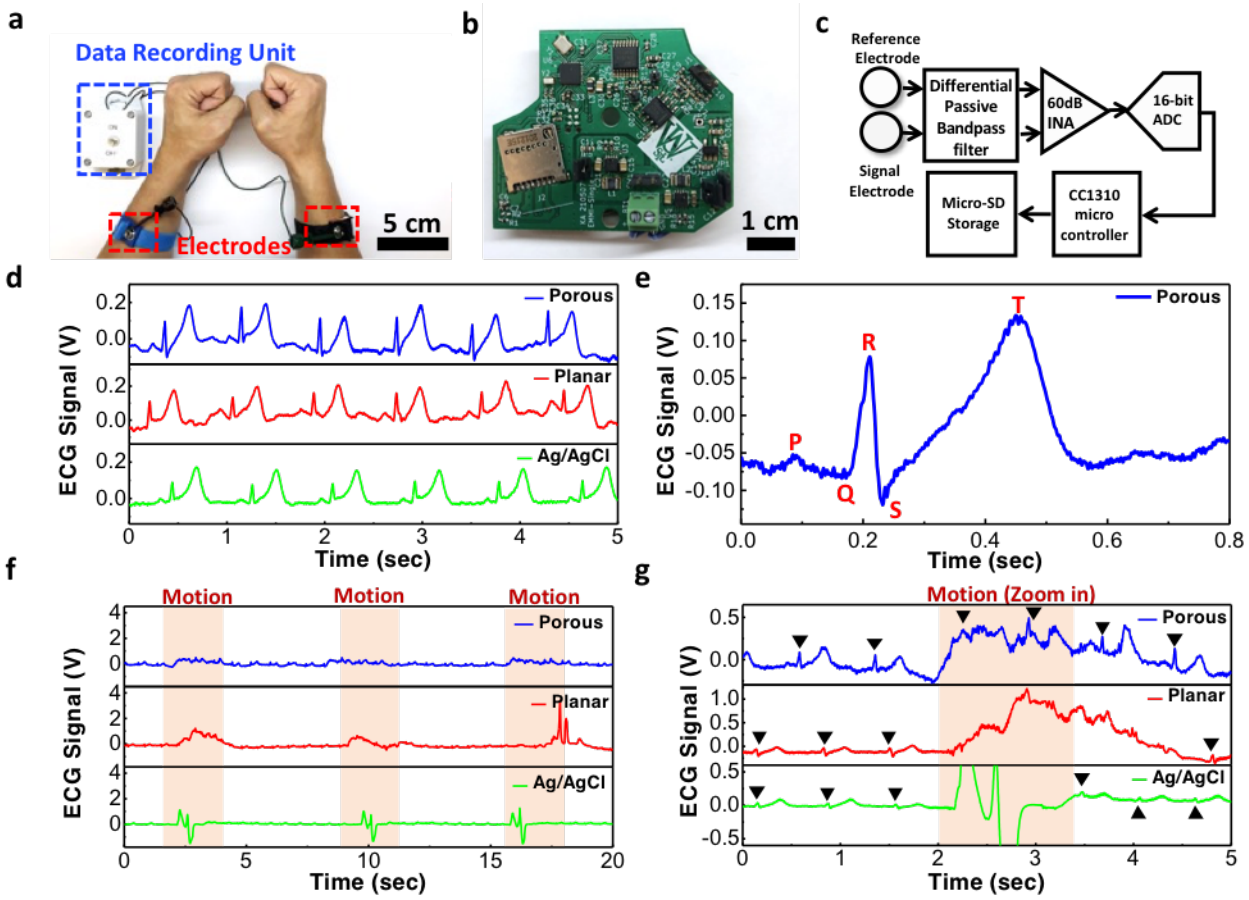

Figure 4.7: ECG recording and the effect of motion artifacts. (a) Photograph showing the ECG recording setup. (b) Photograph showing the PCB board of our in-house built biopotential data recorder. (c) Block diagram of the portable data recording unit. (d) ECG signals were measured using the porous PEDOT:PSS/PDMS electrode, planar PEDOT:PSS electrode, and commercial Ag/AgCl electrode. (e) A representative cycle of the ECG waveform acquired by the sponge electrode shows clear P wave, QRS complex, and T wave. (f) ECG signals are measured under the presence of motion artifacts caused by periodic body movement. (g) A zoomed-in view of the data in (f) shows the ECG peaks along with the motion artifacts.

4.6 Long-term monitoring of ECG signals

For electrophysiologic signal recording sessions in a clinical setting using conventional electrodes, the duration is typically limited to less than one hour due to the drying of the conductive hydrogel. The signal quality could degrade significantly as the gel dries up. Unlike the conventional electrodes, the sponge electrode could hold much more gel inside the micropores and thus allow the electrodes to last much longer. Figure 4.8 compares the ECG waveforms measured by the porous, planar, and commercial electrodes over a duration of 3 hours. As shown in Figure 4.8a, even after 3 hours, the porous electrodes kept producing high-quality ECG signals with a clear P wave, QRS complex, and T wave. As for the planar electrodes (Figure 4.8b) and commercial Ag/AgCl electrodes (Figure 4.8c), the signals were good from the beginning but degraded gradually over time. After 3 hours, the signal amplitude dropped significantly for the planar electrode or even completely disappeared for the Ag/AgCl electrode. Such signal decay can be attributed to the drying of gel as shown in Figure 4.9 and Figure 4.10. Because the total volume of the conductive hydrogel held inside the porous electrode is much larger compared to the amount of gel on the top surface of the planar electrodes, the evaporation of the gel is much slower and thus allowing the porous electrode to last longer. We also extracted the SNR of the ECG waveforms, and the results are displayed in Figure 4.8d. In the beginning, the highest SNR was 23.1 dB from the porous electrodes, which was just slightly better compared to the 22.6 dB from the commercial Ag/AgCl electrodes and 20.3 dB from the planar electrodes. After 2 hours of recordings, the SNR of the Ag/AgCl and planar electrodes dropped significantly to 10.7 and 13.6 dB, respectively, while the porous electrode was still able to maintain an SNR of 17.8 dB. After 3 hours, the signals from the Ag/AgCl electrodes disappeared, and the SNR from the planar electrode dropped to 11.7 dB, worse than the 16.1 dB offered by the porous electrodes. In conclusion, the results suggest that the evaporation rate of the conductive hydrogel may

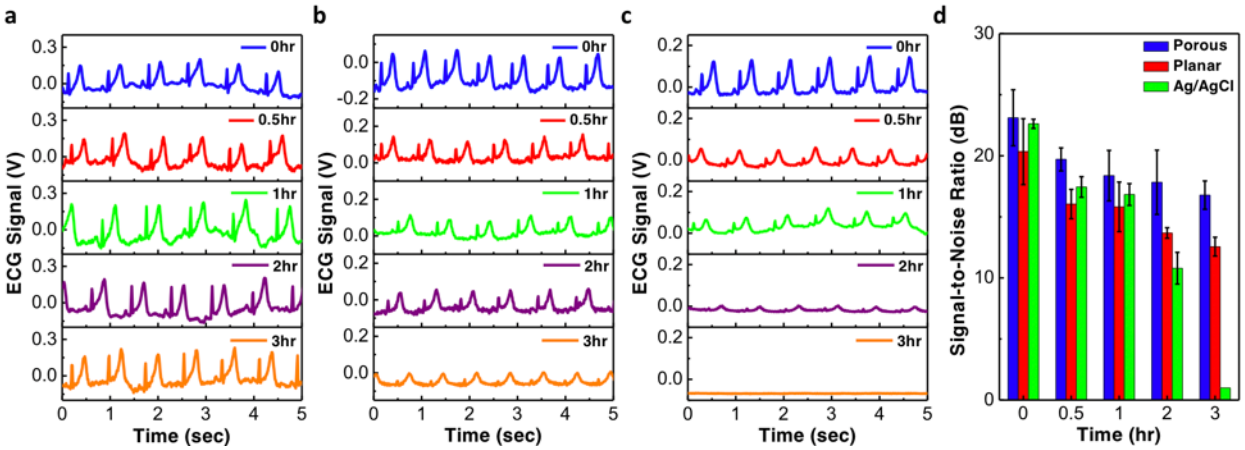

Figure 4.8: Long-term ECG signal recording. (a-c) ECG signals measured after various amount of time using the (a) porous PEDOT:PSS/PDMS electrodes; (b) planar PEDOT:PSS electrodes; and (c) commercial Ag/AgCl electrodes. (d) Comparison of the SNR between the three different types of electrodes.

be slower on the PEDOT:PSS surfaces compared to the Ag/AgCl surfaces and the porous structure inside the sponge electrode can store a larger amount of gel, allowing the stratum corneum layer to remain hydrated and maintaining good electrical contact between the skin and the electrode.

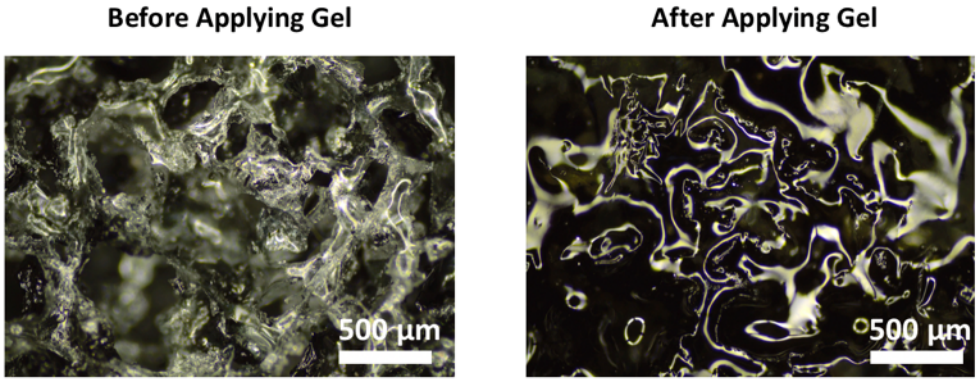

Figure 4.9: Optical micrographs showing the microstructure of the porous electrode before and after conductive hydrogel application. Once the gel is applied on the electrode, it gets absorbed into the sponge, filling all the micropores inside.

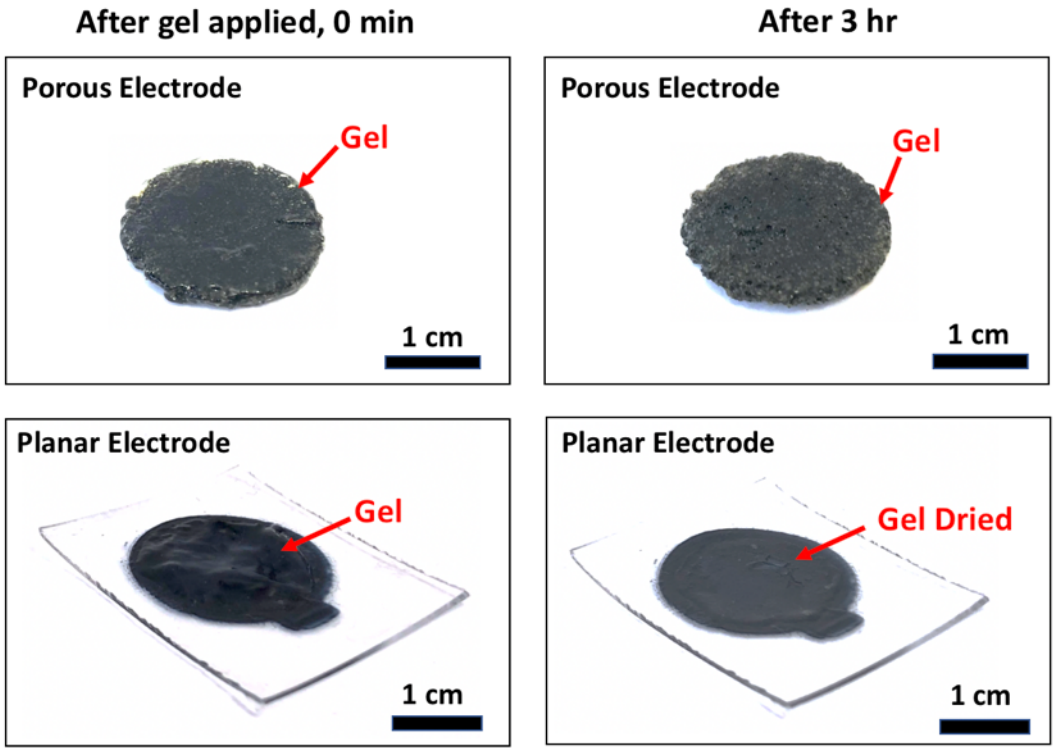

Figure 4.10: Photographs showing a comparison between the drying times of conductive hydrogel on the porous electrode and planar electrode. Because the gel can be fully absorbed into the micropores inside the sponge electrode, the gel dries much slower compared to the gel that can only be applied on the surface of the planar electrode. After three hours, the gel on the planar electrode surface had completely dried up while the sponge electrode remained wet.

4.7 Recording of Muscle EMG and uterine contraction EMG signals

The porous electrode can also be used to measures electrical activities in response to a nerve stimulation of the muscle fibers. In Figure 4.11a, two porous electrodes separated by a distance of 5 cm were placed on the biceps of the left arm and the same data recording unit above was used for data collection. When the volunteer's lifted a weight plate, the biceps brachii muscle contracted and produced strong EMG signals. Figure 4.11b shows the EMG waveforms recorded by the porous, planar and Ag/AgCl electrodes when the volunteer lifted a 7.5 pounds weight. The amplitude of the EMG signal measured by the porous, planar, and Ag/AgCl electrodes were 0.052, 0.048, and 0.051 V, respectively. When the weight was increased to 20 lbs, the amplitude of the EMG signal measured by the porous, planar, and Ag/AgCl increased to 0.098, 0.064, 0.054, respectively (Figure 4.11c). From the EMG signal amplitude summarized in Figure 4.11d, one can find that the porous electrodes can record similar or better signal compared to the gold standard Ag/AgCl electrodes, especially when lifting heavier weight that induces stronger muscle contraction. From the previous experiments on ECG motion artifacts, we have shown that the porous electrode can capture the ECG signal even during the presence of significant motion and muscle activities. Similarly, when heavy weights are lifted, the muscle trembles, and it might affect the EMG signal recording. With the use of a sponge electrode, the conductive hydrogel in the micropores could help mitigate the motion artifacts induced by the muscle tremble, thus allowing a more accurate EMG signal to be recorded. In addition to measuring EMG signals from skeletal muscle cells, the sponge electrodes can also be used to measure EMG from smooth muscle cells that produce much weaker signals. For example, high-quality signals induced by the uterine contraction activities can be measured from the abdominal surface of pregnant women,

providing a noninvasive method for evaluating various labor-related risks such as preterm birth.[204–207] In a patient study of Electromyometral Imaging, uterine contraction EMG during active labor was recorded using the sponge electrodes. The Washington University approved this study in St. Louis Institutional Review Board. One multiparous patient was recruited for this study, and the patient signed the informed consent documents. The uterine contraction EMG recording was performed in a labor and delivery room in Barns and Jewish Hospital, Washington University in St. Louis, School of Medicine when the patient was in active labor with 4.5 cm cervical dilation. Figure 4.11e and Figure 4.12 show the placement of the sponge electrodes on a pregnant woman in labor during the clinical recording session. The sponge electrodes were connected to our own data recording unit, and the commercial active Ag/AgCl electrodes were connected to a commercial 280-channel 24-bit resolution biopotential measurement system (BioSemi B.V, Amsterdam, The Netherlands) for data recording. The recording session lasted a total of approximately 850 seconds or 14 minutes, with 6 uterine contractions confirmed by the tocodynamometer (TOCO). Figure 5f shows the EMG data simultaneously recorded by the sponge and Ag/AgCl electrodes as well as the TOCO data that shows the pressure created by the uterine contraction activities. From the figure, one can see that the EMG signals recorded by the sponge electrode closely resembled the ones recorded by the commercial BioSemi Ag/AgCl active electrodes, and both EMG waveforms correlated well with the uterine contractions recorded by the TOCO. Moreover, the signals from the sponge electrodes exhibited much larger amplitude and better SNR compared to the Ag/AgCl electrodes, which was in part due to the higher gain from our in-house data recording unit (60 dB) compared to the BioSemi data recording system, and also the larger surface area offered by our porous electrode.

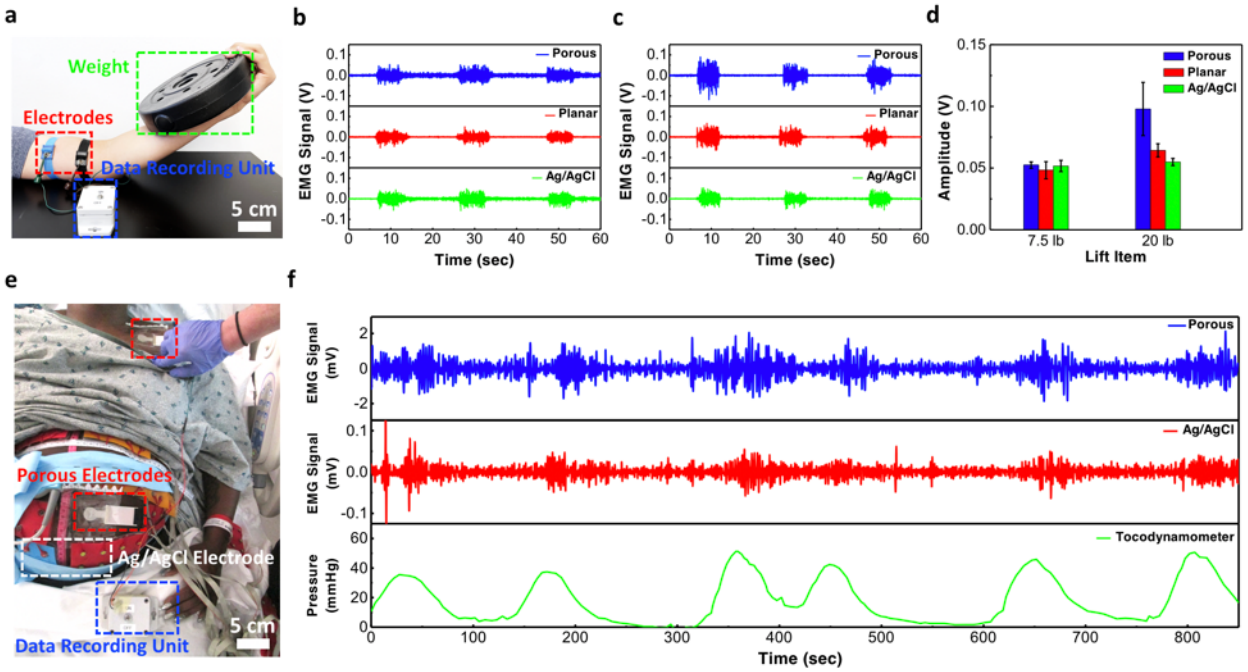

Figure 4.11: EMG signal recording from skeletal muscle and smooth muscle. (a) Photograph showing the setup for measuring EMG signal from the contraction of biceps. (b, c) EMG signals measured using various kinds of electrodes when the subject was lifting a (b) 7.5-lb or (c) 20-lb weight. (d) Comparison of the EMG signal amplitude measured with sponge, planar, and commercial Ag/AgCl electrodes. (e) Photograph showing the setup for recording EMG signals from uterine contraction activities in a clinical setting. (f) Comparison of EMG waveforms recorded from our porous electrodes and in-house built data recorder, the commercial BioSemi active Ag/AgCl electrodes and BioSemi biopotential measurement system, and the corresponding uterine contractions recorded from a tocodynamometer.

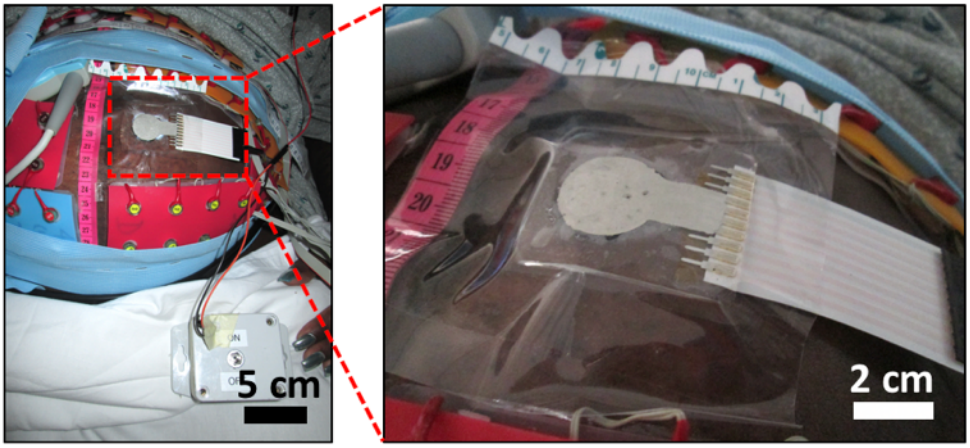

Figure 4.12: Photographs showing the experiment setup for recording the EMG signal from uterine contraction activities. The picture shows the attachments of the porous electrodes, commercial BioSemi Ag/AgCl electrodes, and TOCO on the anterior abdominal surface of a pregnant woman in labor. A piece of PDMS substrate coated with conductive silver epoxy was applied on the bottom surface of the sponge electrode to form electrical connection between the electrode the data recording unit.

4.8 Summary

In conclusion, we have developed a simple and low-cost method for fabricating a soft sponge electrode that is composed of a porous PDMS sponge coated with a conductive PEDOT:PSS layer and demonstrated its use for high-quality ECG and EMG signal recording applications. The porous structure greatly increases the skin-electrode contact area, thereby lowering the skin-electrode impedance and resulting in high-quality biopotential signal recording with improved SNR. More importantly, the sponge electrode can hold significantly more conductive hydrogel within its micropores to help mitigate motion artifacts and allow the electrode to be used for long recording sessions, both of which are crucial for wearable and ambulatory monitoring applications. This work demonstrates the great potential of our sponge electrode as a low-cost alternative for recording high-quality electrophysiologic signals in both in-home and clinical usage settings.

Chapter 5

Multimodal Sensing and Distinguishing of Pressure, Strain and Temperature

5.1 Introduction

The development of soft wearable electronic devices and sensors has attracted significant attention recently due to their wide range of applications in health monitoring,[182] body motion tracking[208] deformable displays,[209] and many others. Unlike conventional electronics manufactured on rigid and brittle wafers, soft electronic devices and sensors attempt to match the mechanical properties of human skin,[169] and they offer desirable features such as elasticity, which allows the device to be stretched and compressed while maintaining electrical performance and reliability. Stretchable pressure sensor,[46] strain sensor,[210] electrocardiogram (ECG) sensor,[211] and photoplethysmography sensor[3] integrated with stretchable electronic interconnects that can be stretched by up to several tens, or even hundreds of percent have all been demonstrated. Owing to their unique properties, these

soft sensors can form intimate contact with the human skin to allow high precision signal recording and also provide great wearing comfort. As a result, they have been extensively studied for wearable health monitoring device applications.

Many of the soft wearable sensors reported in the literature are designed to target the detection of one specific physical or chemical signal. There are some resistive, capacitive, piezo-electric, or triboelectric sensors that are responsive to multiple different stimuli but the selectivity and how to determine what causes the measured response become significant challenges.[212–215] Take pressure sensors as an example: pressure sensing rubber,[67] capacitive pressure sensor based on a structured dielectric layer,[216] and polyvinylidene fluoride- based piezoelectric pressure sensor[99] are good for pressure detection but not particularly suitable for measuring longitudinal strain. On the other hand, strain sensors based on the metal nanoparticles[16, 217] or conductive nanocomposite[218, 219] are typically not very sensitive or even incapable of detecting pressure stimulus. For applications such as wearable health monitoring devices, soft robotics, and many others, it is often desirable to have multimodal sensor devices that are capable of responding to a variety of physical or chemical stimuli. In order to achieve multimodal sensing, one solution is to integrate multiple single-modality sensors into a single sensor device. One example is a planar-type sensor patch with integrated acceleration, temperature, and electrocardiogram sensors to monitor the human motion, skin temperature, and electrocardiogram signals simultaneously.[220] Another example is a device with a layer-by-layer sandwich structure with humidity, thermal, and pressure sensors stacked on top of each other to monitor various motion and daily life activities.[221] Nevertheless, integrating multiple sensors into either planar-type or sandwiched structure and recording each electrical signal independently not only requires a more complex systems and read out circuits but also a more sophisticated fabrication processes and interconnects, which is not necessarily a preferred solution when low-cost sensors are needed.

Alternatively, a number of research groups have reported new device structures capable of detecting various mechanical stimuli and differentiate the stimuli in a single device by utilizing multiple sensing layers.[222, 223] For example, sensors with sandwiched multilayer structure comprising polydimethylsiloxane (PDMS)/single-walled carbon nanotube (SWNT) film/ porous PDMS/PDMS spacers/SWNT-film/PDMS have been reported to detect and differentiate tensile strain due to the change in resistance within SWNTs film and normal pressure from the change in capacitance. In addition, the sensor can also harvest a variety of mechanical energies owing to the triboelectric effect between SWNT, porous PDMS, and the air gap created by PDMS spacers.[224] Sensors based on mechanical interlocking with metal-coated, high-aspect-ratio polyurethane acrylate nanofibers sandwiched between elastomer layers can also achieve pressure, shear, and torsion detection simultaneously and differentiate each stimulus by the magnitudes and frequencies of the corresponding signals.[225] Lastly, a multilayer sensor constructed with polytetrafluoroethylene film, copper sheets, silver nanowires film, and a sponge-like graphene/polydimethylsiloxane composite has also been reported to perform pressure and temperature sensing and material identification due to piezoresistive, thermo- electric, and triboelectric effects.[226]

Despite the significant progress on multimodal sensors described above, it is clear that many of the solutions still require fairly complex device structures and fabrication processes. Here, we report a multimodal sensor with a very simple single-layer device structure comprising a porous PDMS sponge coated with a conductive poly(3,4-ethyl-enedioxythiophene):polystyrene sulfonate (PEDOT:PSS) layer. The sensor can achieve pressure, strain, and temperature sensing and with the ability to distinguish the stimuli. To fabricate the porous PDMS sponge, a commercially available sugar cube was used as a sacrificial template, which can be subsequently leached in hot water. After the PDMS sponge was formed, it was thoroughly

coated with a thin layer of a PEDOT:PSS conductive polymer through a low-cost dip-coating process. The ability to respond to three kinds of stimuli and with the selectivity to distinguish whether the response was caused by pressure, strain, or temperature was achieved by simultaneously measuring both the resistance and capacitance changes and the different trends in their responses (i.e., decrease in resistance and increase in capacitance under pressure; increase in resistance and decrease in capacitance under tensile strain; decrease in resistance and negligible change in capacitance under elevated temperature). The effect of micropore size on the mechanical properties and sensitivity of the sensor has also been studied. If resistance change is used as the calibration curve to quantify the stimuli, then the porous PEDOT:PSS/PDMS sponge sensor with a smaller pore size generally improves sensitivity. Due to high sensitivity to pressure, strain, and temperature change, the porous PEDOT:PSS/PDMS sponge sensor could have various applications toward motion sensing and sensors for soft robots. As a proof-of-concept, we have demonstrated the use of the sensor on an artificial hand for object detection, gesture recognition, and temperature sensing applications.

5.2 Fabrication Process and Materials Characterization

5.2.1 Materials

Polydimethylsiloxane (Sylgard 184) was purchased from Dow Corning. White sugar cube was purchased from C&H. Brown sugar cube was purchase from La Perruche. Poly(3,4-ethylenedioxythiophene)-poly(styrenesulfonate) (1.3 wt % dispersion in H_2O, conductive grade) and ethylene glycol (EG) (anhydrous, 99.8%) were purchased from Sigma-Aldrich. The silver conductive epoxy was purchase from MG Chemicals.

5.2.2 Fabrication of Porous PEDOT:PSS/PDMS Sensor

The PDMS was prepared by mixing the PDMS prepolymer with a curing agent with a mixing ratio of 10:1 w/w, and then a vacuum desiccator was used to remove the bubbles from the PDMS liquid. The sugar cubes 1.5 (W) × 1.5 (L) × 1.5 cm (H) were then dipped into the PDMS liquid for 2 h to let the pores inside the cubes be filled with PDMS liquid. After that, the sugar cubes filled with PDMS were cured in an oven for 3 h at 80 °C. The cubes were then placed in a hot water bath for 1 h at 100 °C to allow the sugar to be dissolved, leaving behind the PDMS sponge.

The porous PDMS sponge was cut into a size of 1.5 (W) × 1.5 (L) × 0.75 cm (H). To aid the wetting, the PEDOT:PSS ink on the hydrophobic PDMS surface, the porous PDMS sample was pretreated by oxygen plasma (Plasma Etch PE25) at 60 W for 30 s on both the top and bottom sides that are 1.5 (W) × 1.5 cm (L). 5 wt % ethylene glycol was added into the PEDOT:PSS solution and then stirred at room temperature for 1 h. The porous PDMS sponge was then dipped into the as-prepared PEDOT:PSS solution for 30 min. After that, the PEDOT:PSS-coated PDMS sponge was cured in the oven for 3 h at 80 °C.

5.2.3 Characterization of PEDOT:PSS/PDMS Sensor

The microstructure of the porous PDMS and porous PEDOT:PSS/PDMS was captured using both an optical microscope (Olympus BX53M) and an environmental scanning electron microscope (Thermo Fisher Quattro S ESEM). The element analysis was performed by environmental scanning electron microscope equipped with an energy-dispersive X-ray spectrometer (Oxford Aztec).

Silver conductive epoxy was applied at the bottom surface of the sensor to make electrical contacts between the sensor and the measurement instruments. The size of the silver conductive epoxy is 1.5 (W) $\times$ 0.1 cm (L). The porous PEDOT:PSS/PDMS sponge sensor was then placed on a modified syringe pump with a 3D-printed loading platform for pressure measurement. A commercial force sensor (FSR 402, Interlink Electronics, Inc.) was attached to the bottom of the loading platform as a reference sensor that measures the actual pressure applied to the sensor. For the tensile strain testing, a modified syringe pump was used with the porous PEDOT:PSS/PDMS sensor clamped in between the moving stage. Temperature sensing experiments were performed on a heating plate. Both the resistance and capacitance measurements were recorded using a semiconductor device analyzer (Keysight B1500A). For the dynamic capacitance measurement, an evaluation board (EVAL-AD7746EB, Analog Devices, Inc.) was used to measure the continuous change of capacitance under pressure and tensile strain.

The compressive and tensile stress-strain curves were measured by a mechanical testing system (ElectroForce 3200). The PDMS sponge made from brown sugar cubes has a larger micropore size than the one made from white sugar cubes. The mechanical characterization results show that the sponge made from brown sugar cubes with a larger pore size and greater porosity has lower Young's modulus and is thus softer than the sponge made from white sugar cubes with smaller pore size.

As shown in Figure 5.1, the Current-voltage (I-V) curves measured from the PEDOT:PSS /PDMS sponge sensors in a relaxed state show a linear relationship. The sensor made from a white sugar cube with a smaller pore size is more resistive than the sensor made from a brown sugar cube.

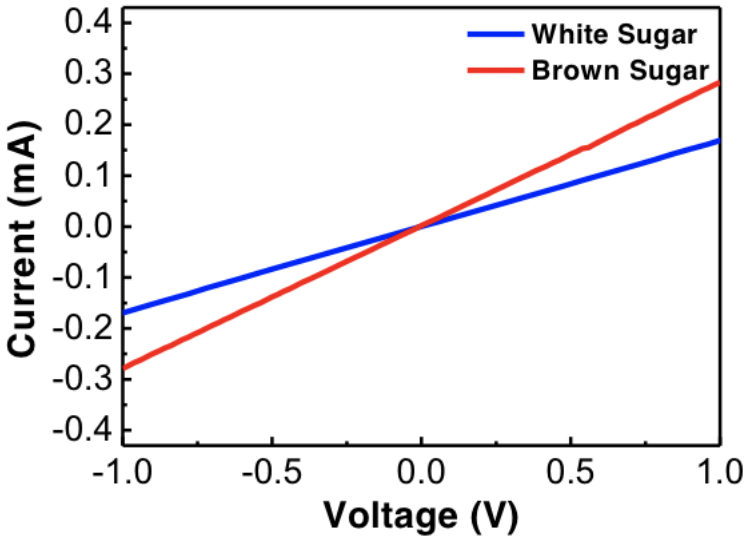

Figure 5.1: Current-voltage relationship of the porous PEDOT:PSS/PDMS sensors made from white and brown sugar cubes.

5.3 Design Concept

The porous PEDOT:PSS/PDMS sensor is capable of detecting and distinguishing pressure, strain, and temperature stimuli. The concept of the sensor's response curves to various types of stimuli are schematically illustrated in Figure 5.2a. When external pressure is applied normal to the top surface of the sensor, the electrical properties of the sensor change. The sensor's electrical resistance decreases due to the increase of contacts between the PEDOT:PSS thin films coated on the porous PDMS sponge, which results in more paths for electrical conduction. In the meantime, the compression of the micropores within the PDMS results in an increase in capacitance because the volume percentage of air in the sensor decreases and the dielectric constant of PDMS ($\varepsilon_{PDMS} = 2.77$) is greater than the air ($\varepsilon_{air} = 1.0006$).[227, 228] In contrast, when a tensile strain is applied along the longitudinal direction of the sensor, the resistance increases due to the elongation of the sensor, which disrupted the conductive PEDOT:PSS thin film, and the capacitance decreases due to the increase in distance of the

sponge between the electrodes. Lastly, as the temperature rises, the increase in thermal energy aids the carrier transport and charge hopping between the PEDOT grains, resulting in a decrease in resistance, whereas the capacitance remains almost unchanged. Therefore, by simultaneously measuring both the electrical resistance and capacitance, the different trends in resistance and capacitance change will allow us to differentiate whether the detected stimulus is from pressure, strain, or temperature. A more detailed study about the sensing mechanism will be discussed in the following paragraphs.

The compressibility, bendability, and stretchability of the porous PEDOT:PSS/PDMS sensor are shown in Figure 5.2b. The shape of the sensor would fully recover after the external stimuli were released. The fabrication processes of the porous PEDOT:PSS/PDMS sensor are schematically illustrated in Figure 5.2c. More details about the fabrication steps and the formulation of conductive PEDOT:PSS ink can be found in the Methods section. In brief, the processes start from commercially available sugar cubes immersed in PDMS liquid, followed by the solidification of PDMS. The sugar/PDMS cubes are then placed in hot water to leach the sugar particles, which results in porous PDMS sponges. Due to the hydrophobicity of PDMS, the PDMS sponges were pretreated with oxygen plasma to improve the wetting of the PEDOT:PSS ink. After the oxygen plasma treatment, the porous PDMS sponges were first immersed in the PEDOT:PSS solution and subsequently placed in an air oven to anneal the PEDOT:PSS thin film. After the above processes, conductive PEDOT:PSS thin film was successfully coated onto the porous PDMS. Both optical photos and optical micrographs of the sugar cubes, porous PDMS sponges, and porous PEDOT:PSS/PDMS sponges (from left to right) are shown in Figure 5.2d. As shown in the left images of Figure 5.2d, both brown and white sugar cubes were used in this study, with brown sugar exhibiting a larger sugar particle size ($700-1000$ μm) than the white sugar ($300-500$ μm). The center images are the porous PDMS sponges formed after sugar leaching. The micropores inside the porous PDMS

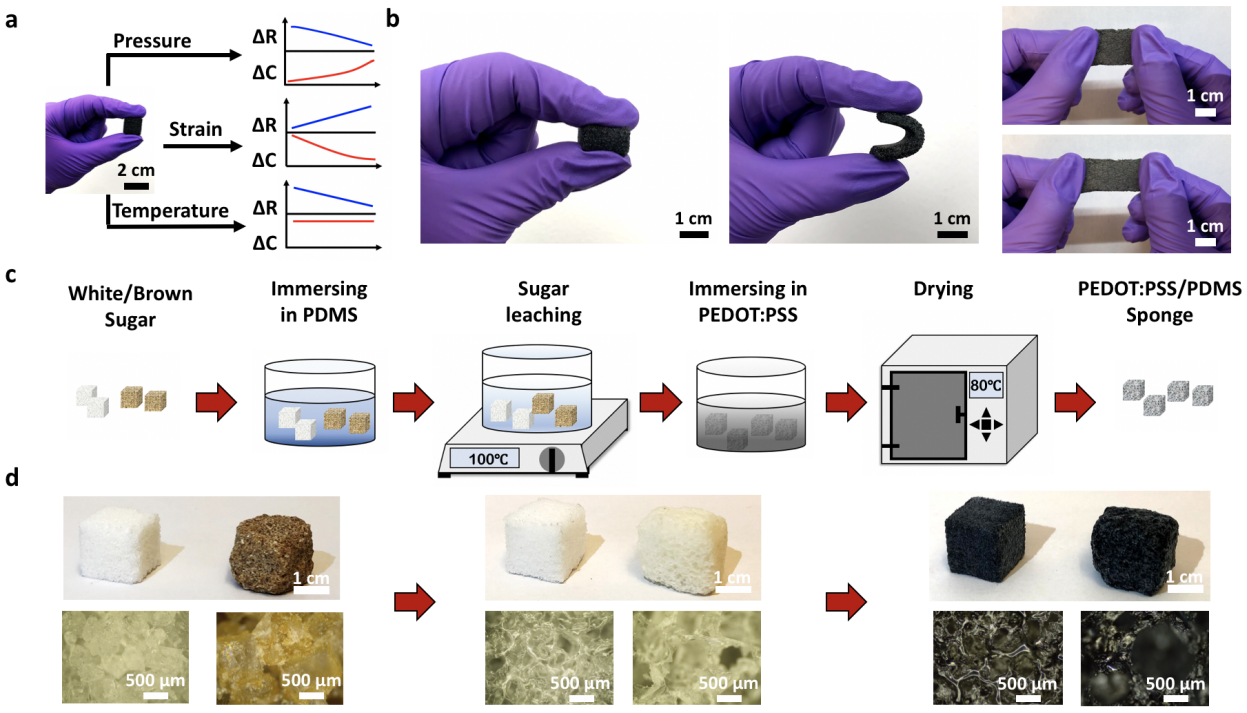

Figure 5.2: Multimodal sensor based on porous PEDOT:PSS/PDMS sponge. (a) Schematics illustrating the different trends in resistance and capacitance change caused by different physical stimuli. (b) Photos showing the compressibility, bendability, and stretchability of the porous PEDOT:PSS/PDMS sponge sensor. (c) Schematics illustrating the fabrication steps of the porous PEDOT:PSS/PDMS sponge sensor. (d) Photos and optical micrographs showing the white and brown sugar cubes used as templates, the corresponding PDMS and PEDOT:PSS/PDMS sponges after each fabrication step.

sponge made with brown sugar is larger than the ones inside the sponge made with white sugar, which is as expected based on the original sugar particle size. The use of different sugar templates allows us to study the effect of micropore size on the sensor response. Lastly, after the PEDOT:PSS coating process, the white color of the porous PDMS sponge turns into black color porous PEDOT:PSS/ PDMS sponge, as shown in the images on the right-hand side of Figure 5.2d.

We have performed the microstructure and the element composition analysis of the porous PDMS sponge and the porous PEDOT:PSS/PDMS sponge by scanning electron microscopy (SEM) and the energy-dispersive X-ray spectroscopy (EDX). The structural formula of PDMS

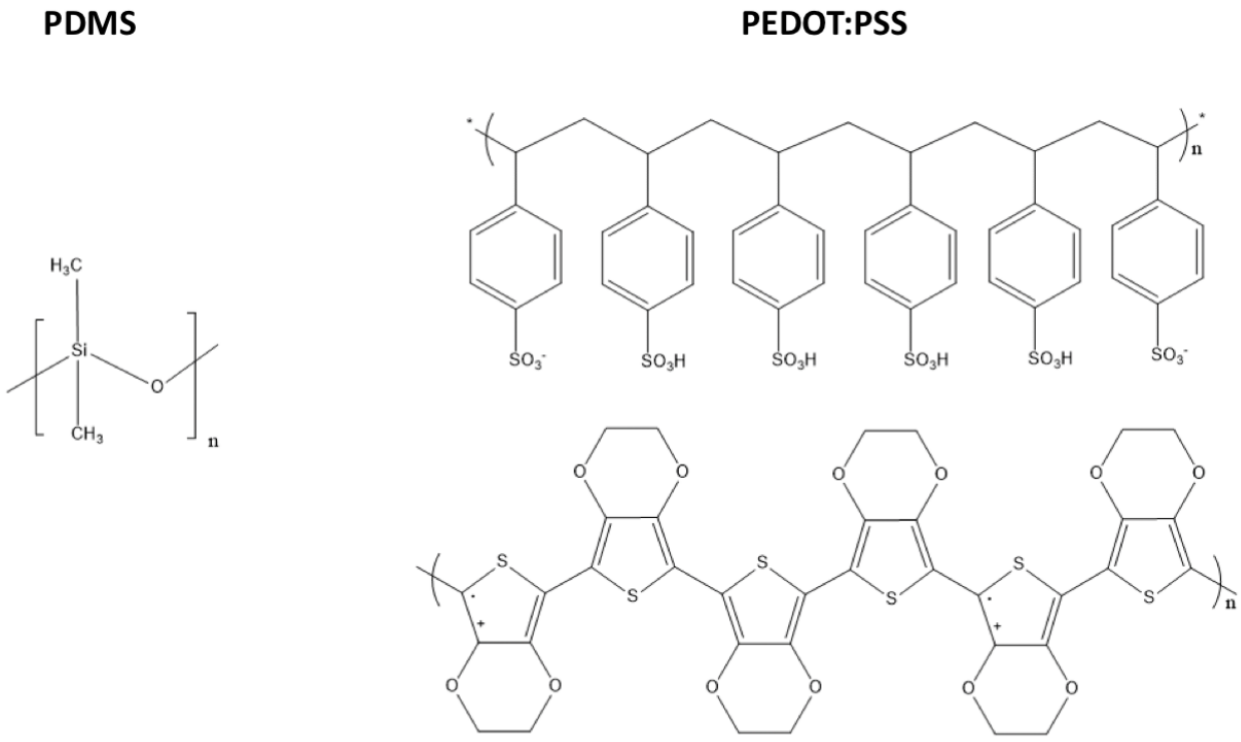

Figure 5.3: The chemical structures of PDMS and conducting polymer PEDOT:PSS, showing the presence of sulfur element in PEDOT:PSS but not in PDMS.

and PEDOT:PSS shown in Figure 5.31 suggests the element content of sulfur is present in PEDOT:PSS but not in PDMS. From the EDX analysis results of porous PDMS sponge shown in Figure 5.4a,b, carbon, oxygen, and silicon elements can be identified. In contrast, from the porous PEDOT:PSS/PDMS sponge, in addition to the three elements above, sulfur can also be found as shown in Figure 5.4c,d, which confirms that the PEDOT:PSS thin film has indeed been coated onto the inner surface of the PDMS sponge. One thing to note is that the small peak at around 1.041 keV ($K_\alpha = 1.041$) in Figure 5.4d is confirmed to be the impurity of sodium content from the glassware. More detailed information is presented in Figure 5.52.

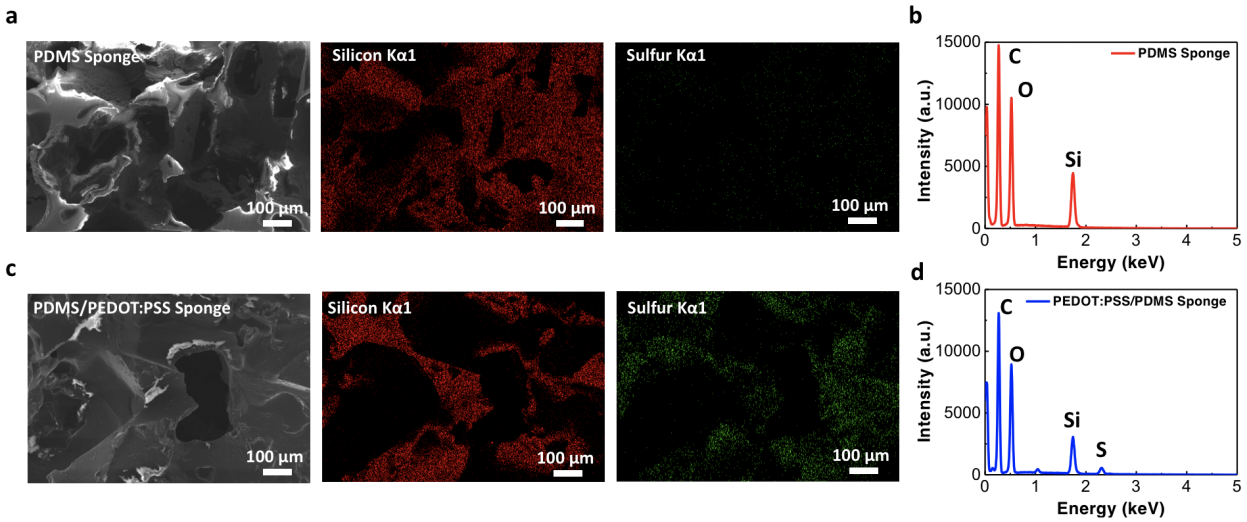

Figure 5.4: SEM and EDX analysis of the multimodal sponge sensor. (a) SEM and the corresponding EDX images of the PDMS sponge. (b) EDX spectrum of the PDMS sponge. (c) SEM and the corresponding EDX images of the PEDOT:PSS/PDMS sponge. (d) EDX spectrum of the PEDOT:PSS/PDMS sponge.

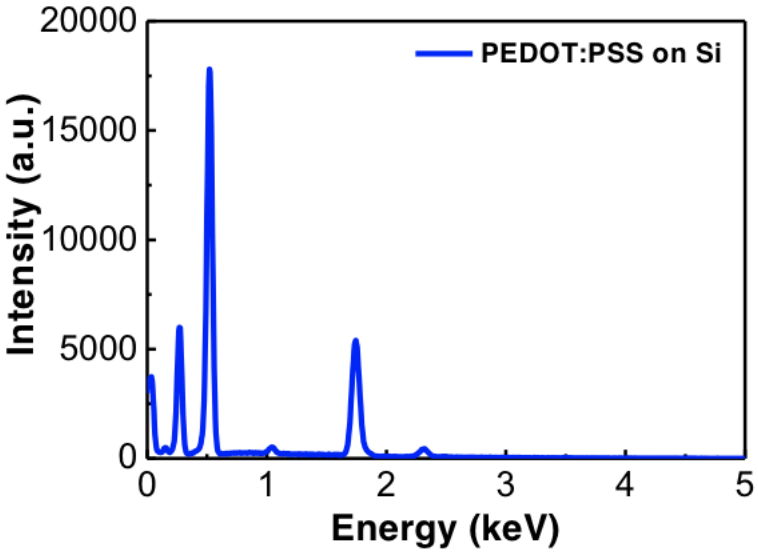

Figure 5.5: EDX analysis of the PEDOT:PSS thin film spun coated on a silicon wafer.

5.4 Characterization of Sensing Modality

5.4.1 Pressure Sensor

In this work, we used two types of sugar templates (white sugar and brown sugar) to fabricate the porous PEDOT:PSS/ PDMS sensor to study and compare the effect of micropore size and porosity on the device sensitivity under compressive and tensile strain stimuli. As discussed in Figure 5.2d, the samples fabricated using white sugar cubes tend to have smaller micropore sizes and lower porosity than those fabricated using brown sugar. Details about the porosity calculation is listed below and can be found in Table 5.1.

$$\text{Porosity} = \frac{\text{Void Volume}}{\text{Total Volume}} = \frac{\text{Total Volume - } \frac{\text{Weight of Porous PDMS Sponge}}{\text{PDMS Density}}}{\text{Total Volume}}$$

As will be discussed below, both the pore size and porosity have a significant impact on the sensor's sensitivity and performance. Figure 5.6a shows the sensor response curve ($\Delta R/R_0$ vs compressive strain) of the porous PEDOT:PSS/PDMS sensor when the device is being compressed to up to 70% strain. From figure 5.6, one can see that the resistance of the sensor decreases with increasing compression strain. For example, under 20% compressive strain, the relative change in resistance of the sensors made from the white sugar and brown sugar are -13 and -5%, respectively. As the compressive strain increases to 70%, the relative change in resistance increases to -61 and -45% for sensors made from white and brown sugar, respectively. The mechanism of the decrease in resistance under compressive strain (i.e., pressure applied normal to the top surface) can be attributed to the increase in the overlapping area of the PEDOT:PSS thin film coated on the inner surface of the porous PDMS sponge. When pressure is applied to the sensor, the micropores gradually close, and

the conductive PEDOT:PSS thin film on the inner surface of the pores forms temporary contacts with each other, resulting in a more conductive network. Once the pressure is released, the micropores return to their initial morphology, which causes the resistance to also return to the initial value. Furthermore, Figure 5.6a also shows that the sensor made from the white sugar cubes exhibits a more significant amount of change in resistance (i.e., better sensitivity) than the sensor made from the brown sugar cubes. As indicated in Figure 5.2d, because the size of the micropores in the PDMS sponge made with white sugar cubes are smaller than the one made from brown sugar cubes, the smaller pore size results in a greater increase in conductive paths formed in PEDOT:PSS under the same amount of compressive strain. As a result, the sensor made from the white sugar cube exhibits a greater amount of change in resistance.

We have also measured the precise pressure applied onto the porous PEDOT:PSS/PDMS sensor under various amount of compressive strain using a commercially available force sensor (FSR 402 Interlink Electronics, Inc.). The sensing response as a function of pressure derived from Figure 5.6a is plotted in Figure 5.6b. More details about the electromechanical setup can be found in the Methods section. From Figure 5.6b, one can see that the sensor made from the brown sugar cubes exhibits a slightly greater response when compared to the sensor made from white sugar cubes under the same amount of pressure. This is because the mechanical properties of the PDMS sponge also have a great impact on the sensor performance. Because the PEDOT:PSS/PDMS sponge sensor made from brown sugar has greater porosity (Table 5.1), it is softer than the sensor made from white sugar (compressive stress-strain curve shown in Figure 5.73), and therefore experiences higher compressive strain and larger deformation of the micropores under the same amount of pressure. Moreover, the sensor made from the brown sugar cubes can only be compressed up to 86 kPa, whereas the sensor made from white sugar can go up to 229 kPa at 70% of compressive strain. The

dynamic response of the porous PEDOT:PSS/PDMS sensor has also been studied, and the results are presented in Figure 5.6c. The sensors were repeatedly compressed to a strain of 70% and then released to a relaxed state. The results show that the resistance decreases when the sensor is compressed and returns to the initial value after the pressure is released during each loading-unloading cycle, confirming the good repeatability of the sensor response.

The electrical capacitance of the sensor is also responsive to the compressive strain. Figure 5.6d shows the relative change in capacitance plotted as a function of compressive strain ($\Delta C/C_0$ vs compressive strain), and Figure 5.6e shows the relative change in capacitance plotted as a function of pressure ($\Delta C/C_0$ vs pressure). When pressure is applied, the capacitance of the sponge sensor increases due to an increase in its effective dielectric constant. More specifically, when a sponge sensor is in its relaxed state, the fringing capacitance is composed of the capacitance of the PDMS sponge and the air within the micropores. When the sensor gets compressed, the air is displaced, and a larger percentage of the volume is now composed of PDMS, which has a much greater permittivity than air (2.77 for PDMS vs 1.00061 for air), resulting in an increase in the device capacitance. In terms of the relation between the pore size on the capacitance change, the relative change in capacitance is greater for the sample with a larger micropore size and higher porosity (sensor made from the brown sugar) both under the same compressive strain (Figure 5.6d) and pressure (Figure 5.6e). Similarly, the capacitance change in the porous PEDOT:PSS/PDMS sponge sensor also shows great repeatability, as can be seen from the dynamic response measurements in Figure 5.6f. In summary, the mechanisms of the sensor response under compression discussed above are schematically illustrated in Figure 5.6g.

Table 5.1: The porosity comparison between the PDMS sponges made from white sugar cubes and brown sugar cubes.

	Porosity	**Standard deviation**
PDMS sponge made from white sugar cubes	0.6192	0.0145
PDMS sponge made from brown sugar cubes	0.6966	0.0125

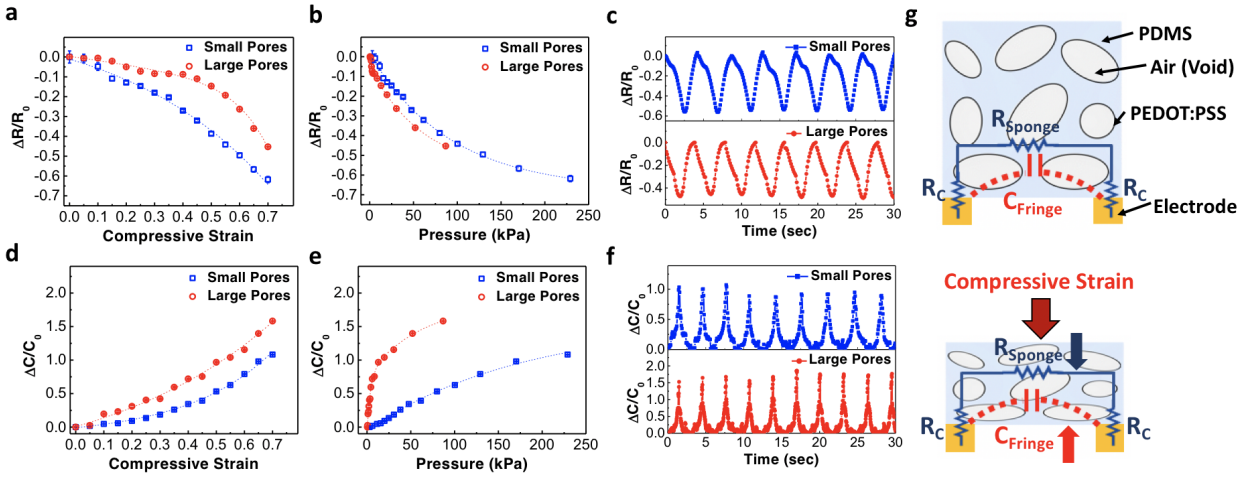

Figure 5.6: Electrical characterization of the porous PEDOT:PSS/PDMS sensor in response to compressive strain and pressure. (a) Relative change in resistance plotted as a function of compressive strain. Dotted lines: fitting curves. (b) Relative change in resistance plotted as a function of pressure. Dotted lines: fitting curves. (c) Dynamic response in resistance of the porous PEDOT:PSS/PDMS sensor when it was repeatedly compressed to a strain of 70% and released. (d) Relative change in capacitance plotted as a function of compressive strain. Dotted lines: fitting curves. (e) Relative change in capacitance plotted as a function of pressure. Dotted lines: fitting curves. (f) Dynamic response in capacitance of the porous PEDOT:PSS/PDMS sensor when it was repeatedly compressed to a strain of 70% and released. (g) Schematic illustration of the porous PEDOT:PSS/PDMS sponge sensor showing the increase in fringe capacitance and decrease in electrical resistance under compressive strain.

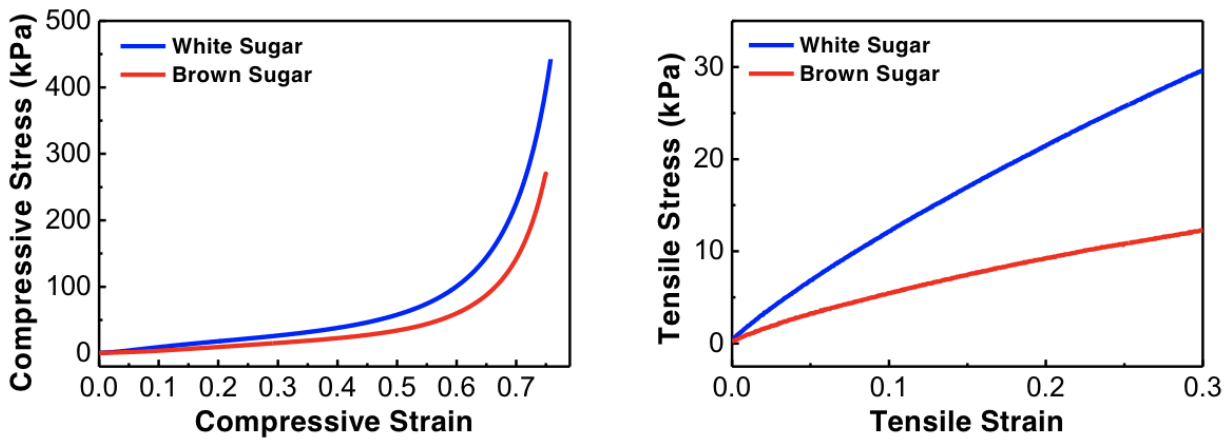

Figure 5.7: The compressive (a) and tensile (b) stress-strain curves of the porous PEDOT:PSS/PDMS sponge sensor.

5.4.2 Strain Sensor

In addition to responding to compressive strain and pressure, the porous PEDOT:PSS/PDMS sensor can also respond well to tensile strain. Figure 5.8a shows the sensor response curve ($\Delta R/R_0$ vs tensile strain) of the porous PEDOT:PSS/PDMS sponge when stretched to a strain of 30%. As the tensile strain increases, the porous PEDOT:PSS/ PDMS sensors made from both white and brown sugar show an increase in resistance due to the disruption of PEDOT:PSS thin film. Similar to its response to pressure, the pore size of the sensor also affects its sensitivity and the response to the tensile strain. From the current-voltage curves measured from the porous PEDOT:PSS/PDMS sensors in their relaxed state (Figure 5.14 and Table 5.2), one can find that the resistance (R_0) of the sensor made from white sugar cube (smaller pore size) is greater than the sensor made from the brown sugar cube (larger pore size). The higher resistance in the relaxed state from the porous PEDOT:PSS/ PDMS sensor with smaller pores suggests that the coating layer thickness and the content of conductive PEDOT:PSS on the PDMS sponge with smaller pores may be less than the one with larger pores. The smaller pore size also results in a more significant increase in resistance under the

same amount of tensile strain. For example, when the sensor is stretched to a strain of 10%, the sensor made from the white sugar cubes exhibits a resistance increase of 21.4% compared to 14.0% for the sensor made from brown sugar cubes. As the tensile strain increases to 30%, the sensor made from the white sugar cubes exhibits a resistance increase of 150% compared to 42% for the sensor made from brown sugar cubes. The greater response and better sensitivity from the sponge sensor with smaller pore size can be attributed to the smaller thickness of PEDOT:PSS coating on the sponge, which makes the PEDOT:PSS conductive pathway in the sensor made from white sugar cubes more easily to be disrupted upon longitudinal stretch leading to a greater change in resistance under the same amount of tensile strain. The dynamic response of the porous PEDOT:PSS/PDMS sensor under tensile strain is also measured and shown in Figure 5.8b. Both sensors were repeatedly stretched to a strain of 30% and released, and the sensor response ($\Delta R/R_0$) remained stable after each stretching-releasing cycle. Figure 5.8c shows the capacitance change of the porous PEDOT:PSS/PDMS sponge sensor ($\Delta C/C_0$ vs tensile strain) when stretching to a strain of 30%. The sensor exhibits a decrease in capacitance under tensile strain due to an increase in distance between two contact electrodes and a reduction in effective dielectric constant when the sponge is stretched. Comparing the sensors made from the white sugar cubes and the brown sugar cubes, the latter exhibits a greater change in capacitance under the same amount of tensile strain, which arises from the larger micropore size and the higher porosity causing a greater change in air volume and a more significant decrease in dielectric constant. In summary, for both pressure and tensile strain stimuli, smaller pore size results in a greater change in resistance and less change in capacitance. For dynamic response, similar to the resistance change presented in Figure 5.8b, the capacitance change of the porous PEDOT:PSS/ PDMS sensor (Figure 5.8d) also remains stable and shows no noticeable degradation under cyclic stretch tests to a strain of 30%. The long-term stability test results

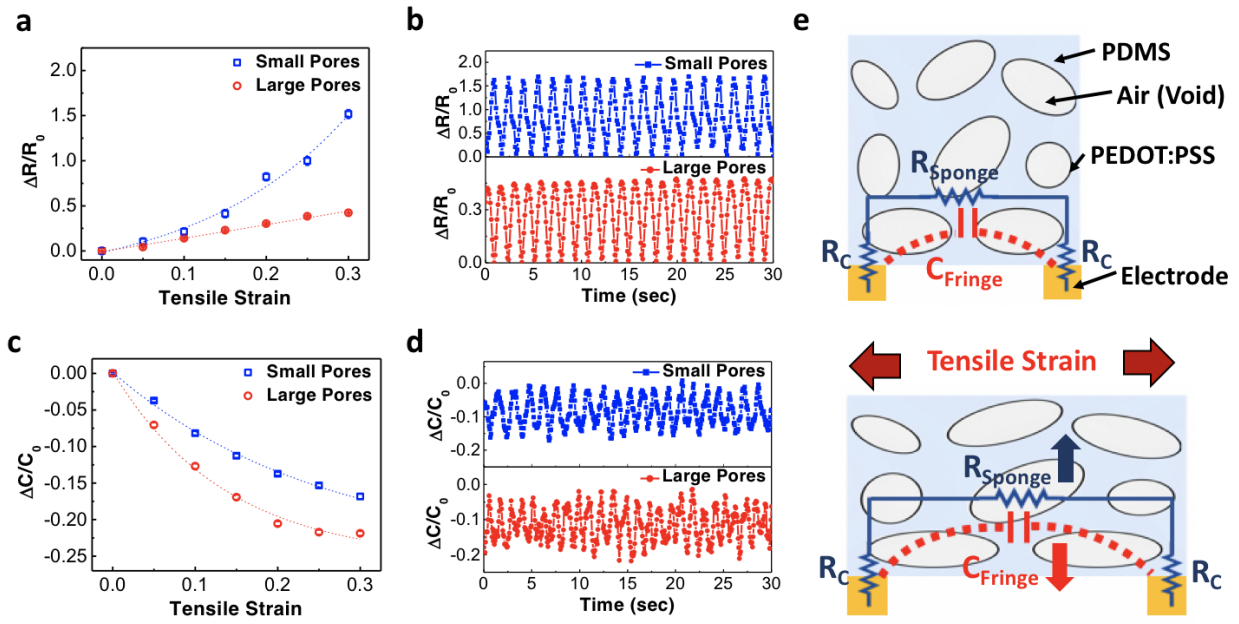

Figure 5.8: Electrical characterization of the porous PEDOT:PSS/PDMS sensor in response to tensile strain. (a) Relative change in resistance plotted as a function of tensile strain. Dotted lines: fitting curves. (b) Dynamic response in resistance of the porous PEDOT:PSS/PDMS sensor when it was repeatedly stretched to a strain of 30% and released. (c) Relative change in capacitance plotted as a function of tensile strain. Dotted lines: fitting curves. (d) Dynamic response in capacitance of the porous PEDOT:PSS/PDMS sensor when it was repeatedly stretched to a strain of 30% and released. (e) Schematic illustration of the porous PEDOT:PSS/PDMS sponge sensor showing the decrease in fringe capacitance and increase in electrical resistance under tensile strain.

with up to 1000 cycles can be found in Figure 5.9 and Figure 5.10. Figure 5.8e schematically illustrates the mechanisms of the sensor response under tensile strain.

5.4.3 Temperature Sensor

Because PEDOT:PSS is a well-known temperature-sensitive conductive polymer,[161, 229–231] it can also be used for temperature sensing applications. For the experiments below, porous sensors with smaller pore sizes were used. The electrical conductivity depends on the charge transport along the conductive PEDOT grains and the charge hopping between the PEDOT and PSS grains. As the temperature increases, the increased thermal energy makes it

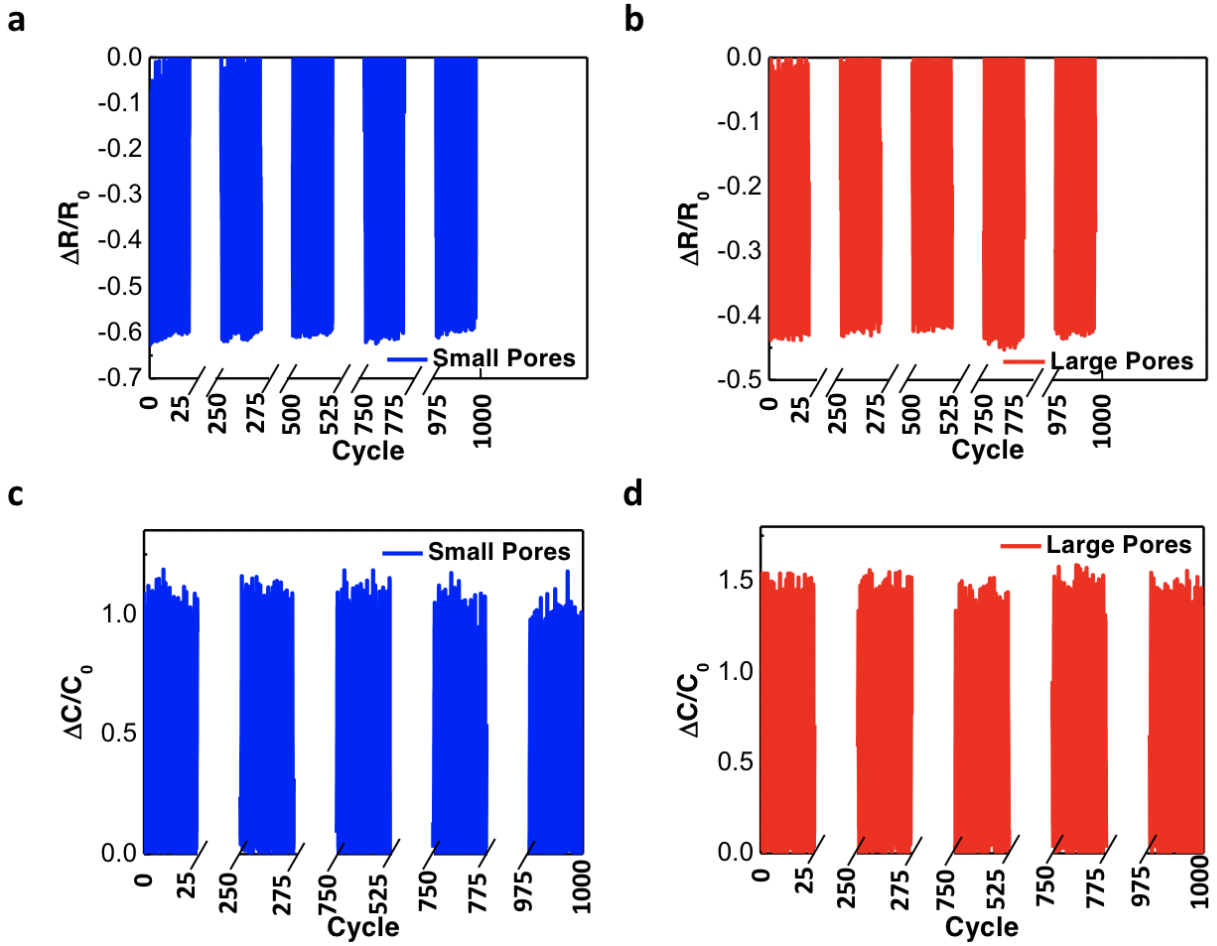

Figure 5.9: Long-term dynamic response measurements of the porous PEDOT:PSS/PDMS sensor in response to compressive strain. (a, b) Relative change in resistance of the sensor when it was repeatedly compressed to a strain of 70% and released for 1000 cycles. (c, d) Relative change in capacitance of the sensor when it was repeatedly compressed to a strain of 70% and released for 1000 cycles.

Table 5.2: Resistance and capacitance values of the porous PEDOT:PSS/PDMS sponge sensor (width, length, and height of the sponge are all 1.5 cm) measured in relax state.

	R_0 (Ω)	Standard deviation	C_0 (F)	Standard deviation
Sensor made from white sugar cubes	5955.42	586.87	3.35x10-12	6.17 x10-13
Sensor made from brown sugar cubes	2953.9	452.68	3.92 x10-12	4.75 x10-13

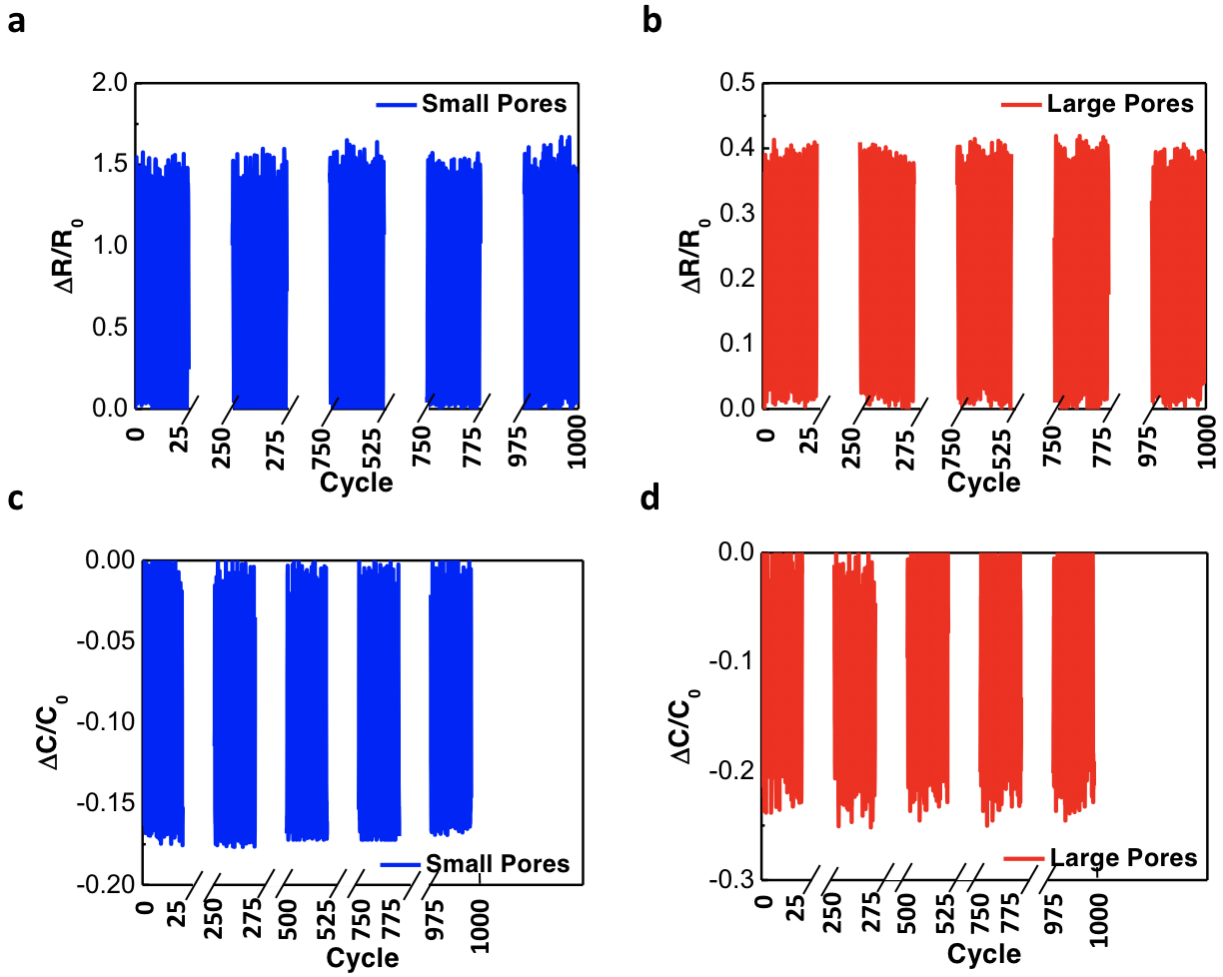

Figure 5.10: Long-term dynamic response measurements of the porous PEDOT:PSS/PDMS sensor in response to tensile strain. (a, b) Relative change in resistance of the sensor when it was repeatedly stretched to a strain of 30% and released for 1000 cycles. (c, d) Relative change in capacitance of the sensor when it was repeatedly stretched to a strain of 30% and released for 1000 cycles.

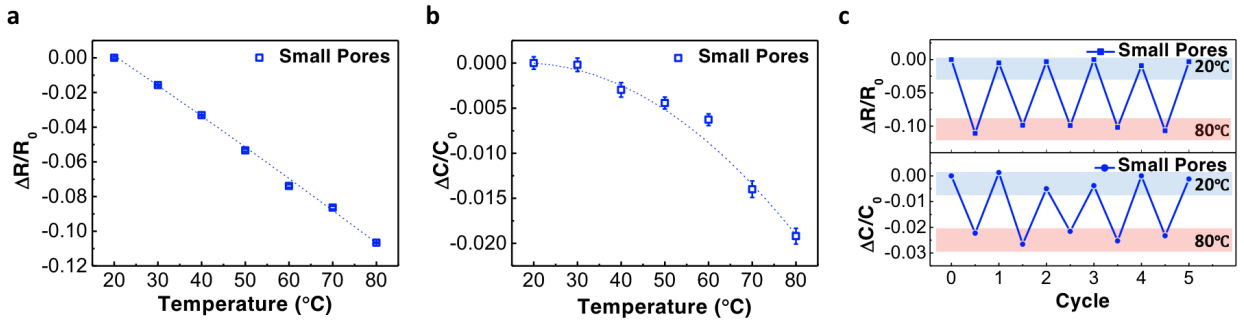

Figure 5.11: Electrical characterization of the porous PEDOT:PSS/PDMS sensor in response to temperature change. (a) Relative change in resistance plotted as a function of temperature. Dotted line: fitting curve. (b) Relative change in capacitance plotted as a function of temperature. Dotted line: fitting curve. (c) Dynamic response of the porous PEDOT:PSS/PDMS sensor under cyclic heating and colling between 20 and 80 °C.

more likely for charge carriers to overcome the potential barriers and hop between the adjacent grains, which results in a decrease in the resistance of the film. Figure 5.11a,b shows the resistance and capacitance change of the porous PEDOT:PSS/PDMS sponge sensor measured at various temperatures. The resistance decreases linearly with increasing temperature due to the enhancement of charge transport discussed above, and the results are also consistent with previously reported work.[232] In terms of the capacitance, the measured change was only -2.0% when the sample was heated from room temperature to 80 °C, which was much smaller than the changes measured under compressive or tensile strain. The slight decrease in capacitance under heating could be attributed to the thermal expansion of the porous PDMS due to its high thermal expansion coefficient, which would lead to a reduction in capacitance similar to the tensile strain case analyzed above. We tested the sensor under repeated heating and cooling cycles from between 20 and 80 °C and confirmed that its response was repeatable. Additional data with more heating/cooling cycles can be found in Figure 5.12.

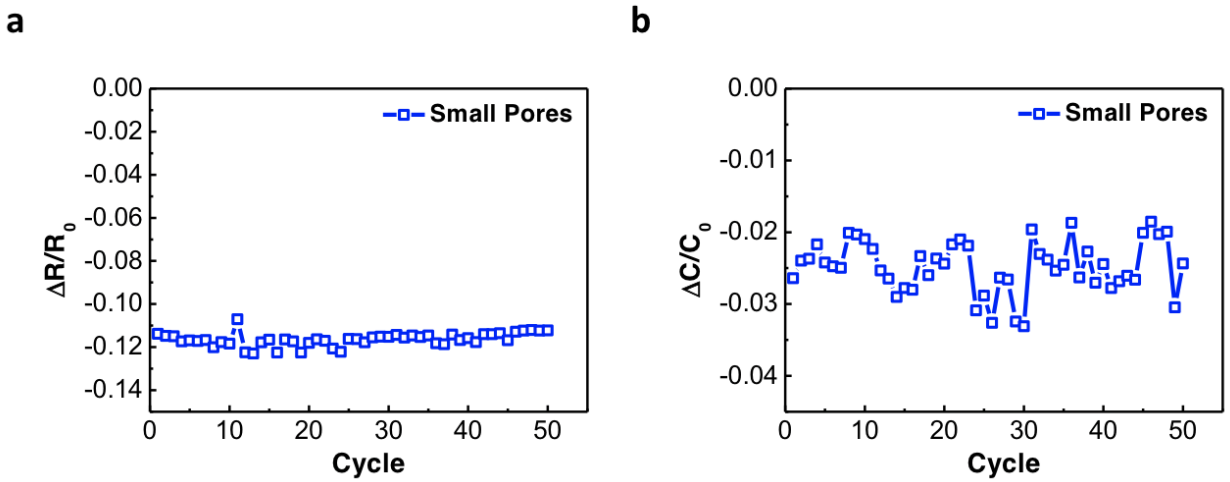

Figure 5.12: Long-term measurements of the porous PEDOT:PSS/PDMS sensor in response to temperature change. (a) Relative change in resistance of the sensor measured at 80 °C after each heating cooling cycle for 50 cycles. (b) Relative change in capacitance of the sensor measured at 80 °C after each heating cooling cycle for 50 cycles.

5.5 Multimodal sensor applications

Because the resistance and capacitance change in the porous PEDOT:PSS/PDMS sensor exhibit different trends for different stimuli, selectivity can be achieved by simultaneously measuring the device resistance and capacitance. The ability to differential pressure, strain, and temperature could enable various applications in smart wearables. In Figure 5.13, we have shown that the above porous PEDOT:PSS/PDMS sensors can be attached to different positions on an artificial hand to demonstrate object detection, gesture recognition, and temperature sensing applications. For example, if a resistance decrease and a capacitance increase are measured from the sensor, it can be inferred as a pressure stimulus applied on its surface. In contrast, when the resistance increases and the capacitance decreases, it means the sensor is being stretched. Lastly, when the resistance decreases but with no noticeable change in capacitance, it could be interpreted as increasing temperature. In Figure 5.13a, five sponge sensors were attached to the fingertips to detect the pressure exerted on the fingertip when

the hand was grabbing an object. The resistance and capacitance data clearly show that when the hand was holding an object, only the sensors on figures that were in contact with the object showed decrease in electrical resistance and an increase in capacitance. By comparing the resistance and capacitance change with the response curve in Figure 5.6b,e, it is possible to determine the precise pressure on each fingertip using the fitting equations in the Table 5.3. In Figure 5.13b, the sensors were attached to the finger joints to measure the bending angle of the joints to determine the hand gestures. When the palm was fully open, there was no bending in any of the sensors and thus no change in resistance and capacitance. When the figures were bent, the sponge sensors were stretched, and the tensile strain resulted in an increase in resistance and a decrease in capacitance. The resistance and capacitance values could be used to determine the strain applied and the precise bending angle of each finger based on the data in Figure 5.8. Lastly, the porous PEDOT:PSS/ PDMS sensor attached to the fingertips can also be used to detect the temperature change. As shown in Figure 5.13c, the artificial hand was placed on a hot plate heated to 20, 50, and 80 °C, respectively. As expected, the electrical data show that the resistance decreases monotonically under elevated temperatures while the capacitance remains almost unchanged.

Table 5.3: Summary of ink formulations and measured properties.

Name of the measurement	**Pore size**	**Equation**	**R^2**
$\Delta R/R_0$ vs. Compressive Strain	small	$\Delta R/R_0$ = -0.11·exp(-ε/-0.52) – 0.11·exp(-ε/0.52) + 0.21	0.9877
$\Delta R/R_0$ vs. Compressive Strain	large	$\Delta R/R_0$ = -0.065·exp(-ε/-0.197) – 0.065·exp(-ε/-0.197) + 0.003	0.9789
$\Delta C/C_0$ vs. Compressive Strain	small	$\Delta C/C_0$ = 0.06·exp(-ε/-0.306) + 0.06·exp(-ε/-0.306) – 0.137	0.995
$\Delta C/C_0$ vs. Compressive Strain	large	$\Delta C/C_0$ = 0.38·exp(-ε/-0.62) + 0.38·exp(-ε/-0.62) – 0.755	0.9959
$\Delta R/R_0$ vs. Pressure	small	$\Delta R/R_0$ = 0.34·exp(-P/93.15) + 0.344·exp(-P/93.15) – 0.67	0.9944
$\Delta R/R_0$ vs. Pressure	large	$\Delta R/R_0$ = 0.53·exp(-P/61.19) + 0.07·exp(-P/1.9) – 0.58	0.9908
$\Delta C/C_0$ vs. Pressure	small	$\Delta C/C_0$ = -0.8·exp(-P/178.11) – 0.8·exp(-P/178.09) + 1.55	0.9952
$\Delta C/C_0$ vs. Pressure	large	$\Delta C/C_0$ = -0.82·exp(-P/3.71) – 1.07·exp(-P/57.71) + 1.82	0.997
$\Delta R/R_0$ vs. Tensile Strain	small	$\Delta R/R_0$ = 0.18·exp(-ε/-0.18) + 0.18·exp(-ε/-0.18) – 0.38	0.9697
$\Delta R/R_0$ vs. Tensile Strain	large	$\Delta R/R_0$ = 13.73·exp(-ε/-18.58) + 13.73·exp(-ε/-18.32) – 27.48	0.9721
$\Delta C/C_0$ vs. Tensile Strain	small	$\Delta C/C_0$ = 0.12·exp(-ε/0.25) + 0.12·exp(-ε/0.25) – 0.24	0.9923
$\Delta C/C_0$ vs. Tensile Strain	large	$\Delta C/C_0$ = 0.13·exp(-ε/0.13) + 0.13·exp(-ε/0.13) – 0.25	0.9852
$\Delta R/R_0$ vs. Temperature	small	$\Delta R/R_0$ = -1.66·10-3··T – 1.403·10-6·T^2 + 0.035	0.9983
$\Delta C/C_0$ vs. Temperature	small	$\Delta C/C_0$ = 3.0347·10-4·T – 6.156·10-6·T^2 – 0.0038	0.9645

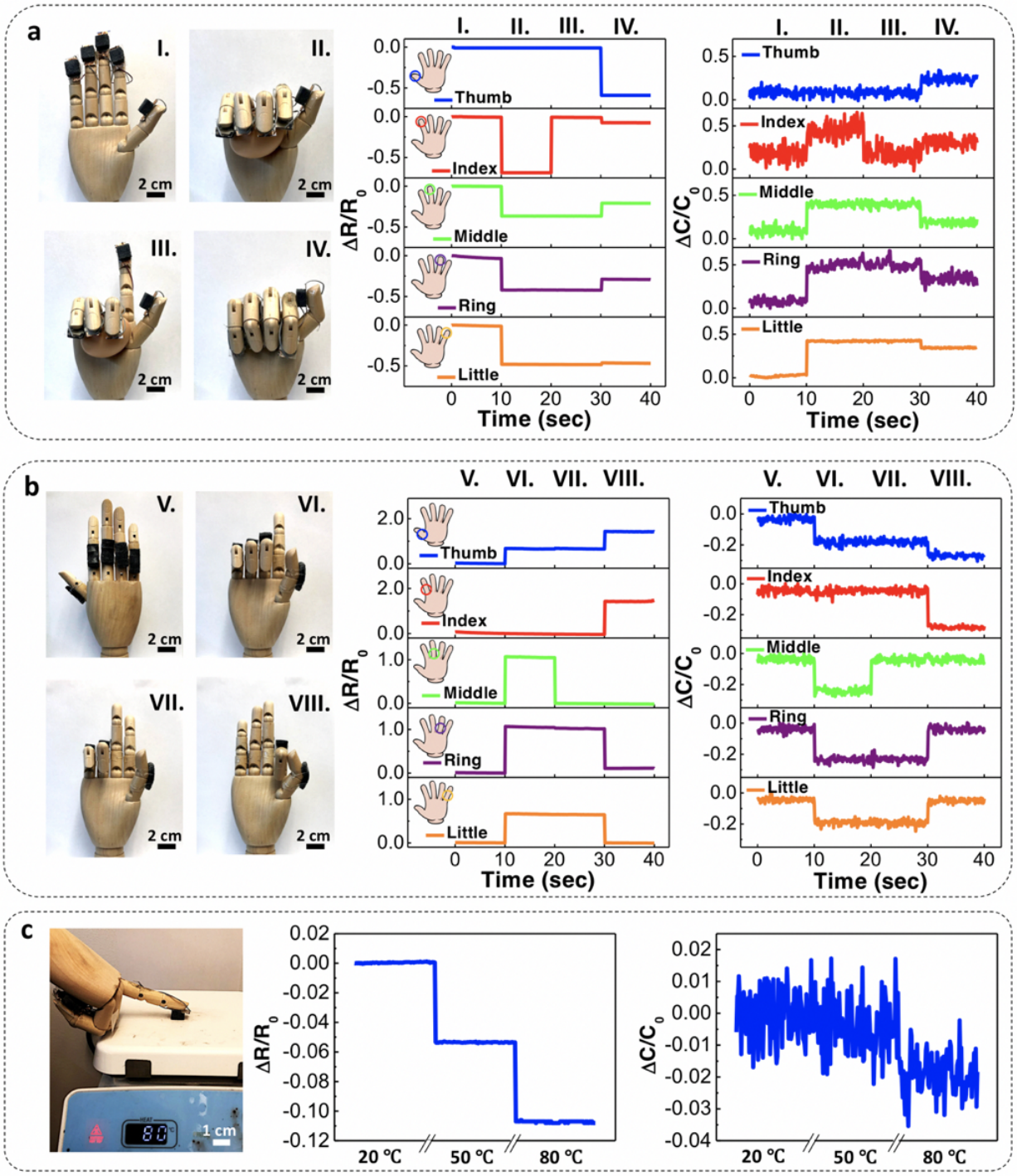

Figure 5.13: (Caption next page.)

Figure 5.13: Application of the multimodal sponge sensor for object detection, gesture recognition, and temperature sensing. (a) Porous PEDOT:PSS/PDMS sensors were attached to the five fingertips of an artificial hand for pressure sensing application. Various fingers were brought into contact with the object in I, II, III, and IV, and responses can be measured in the corresponding sensors, which indicate the detection of contacts between the fingertips and the object. (b) Porous PEDOT:PSS/PDMS sensors were attached to the finger joints of an artificial hand for gesture detection application. The five different fingers were bent to various amount in V, VI, VII, and VIII, and the correct responses can be measured in the corresponding sensors, allowing the gesture of the hand to be detected. (c) Porous PEDOT:PSS/PDMS sensor attached to the fingertip was brought into contact with a hot plate. The resistance change in the sensor allows the surface temperature to be measured.

5.6 Summary

In summary, we have achieved a soft, lightweight, and high sensitivity sponge sensor based on porous PDMS coated with a thin layer of PEDOT:PSS. The sensor can respond to and distinguish three different types of stimuli (pressure, strain, and temperature) through the changing resistance and capacitance. The mechanism of the sensor's response to different stimuli and the effect of the pore size on the sensor performance have been systematically studied. With its stretchability, sensitivity, and multimodality sensing capability, we have further demonstrated its application in pressure sensing, temperature sensing, object detection, and gesture recognition. The sensor developed in this work may lead to low-cost wearables for motion tracking and soft robotics applications.

Chapter 6

Conclusion and Future Work

6.1 Summary of Dissertation

In this thesis, the author has studied the synthesis of stretchable materials, the fabrication process, the characterization and the integration of each sensory component, including strain sensors, pressure sensors, temperature sensors, stretchable conductors, ECG, EMG, PPG sensors. The author also demonstrated the capability and feasibility of using stretchable sensors in a clinical setting.

Soft pressure sensors have a wide range of application in smart wearables, the resistive pressure sensors are promising due to their great sensitivity and the simple readout circuit that can measured the resistance change. We have demonstrated an inkjet-printed resistive pressure sensor that offers high sensitivity of up to 0.48 kPa^{-1} with a simple device structure consisting of a piece of PDMS, conductive silver nanoparticle film, and VHB tape. The sensing mechanism of the sensor mainly comes from the microcracks formed by the pressure-induced

strain. The demonstrated prototype shows the ability to measure arterial pulse waveforms or detect acoustic vibrations, which are promising for biomedical applications.

Stretchable conductor is one of the key components in soft electronics that allows seamless integration of devices and sensor on elastic substrate. We have demonstrated a PEDOT:PSS/PEO stretchable polymer blend that can be patterned using inkjet printing with low sheet resistance of 84 $\Omega/\square$ and can resist up to 50% of tensile strain up to 1000 cycles with only minimal changes in electrical performance. By integrating stretchable PEDOT:PSS/PEO conductor with light-emitting diodes and photodetectors, a photoplethysmography has been demonstrated to show the heart rate of 72 bpm. The stretchable PEDOT:PSS/PEO can also be used as dry electrodes for ECG recording, which shows the potential for low-cost smart wearable health monitor applications.

Besides pressure sensors and stretchable conductors, the skin-attachable electrodes are another important component of human health monitoring. In this work, we reported an elastomer sponge electrode that reduces electrode-skin contact impedance, improves signal-to-noise ratio, and is suitable for long-term biopotential signals recordings with reduced motion artifacts. The sponge electrode fabricated from a simple sugar leaching and low-cost dip-coating process contains numerous micropores that greatly increase the skin-electrode contact area and help lower the contact impedance by a factor of 5.25 or 6.7 compared to planar PEDOT:PSS electrodes or gold-standard Ag/AgCl electrodes, respectively. By using these sponge electrodes, we have demonstrated long-term ECG monitoring up to three hours, the feasibility of EMG monitoring in a clinical setting, and high signal-to-noise ratio biopotential signals with less motion artifacts. These porous sponge electrodes can shed light for long-term wearable health monitoring applications.

Lastly, the project reported earlier are targeted or responded to individual stimulus. However, it is desirable to have multimodal sensors that can respond to various stimuli. Again, we utilized an elastic PDMS sponge, which can respond to and differentiate between three different types of stimuli, pressure, strain, and temperature by recording changes in resistance and capacitance. Through the study of the effect of pore size on sensor sensitivity, it is found that sponge sensors with smaller pore size usually have higher sensitivity. In this work, we have demonstrated use of the porous sponge sensor on an artificial hand for object detection, gesture recognition, and temperature sensing applications, which shows the potential for human-machine interface applications.

6.2 Outlook

Based on the results achieved in this thesis, there are several potential research directions may be carried out for the next step. They are listed as follows:

6.2.1 Smart Textile for Health Monitoring Applications

Soft wearable electronics have been widely explored in personal health monitoring applications through light-weight skin-attachable devices that provide better electronic-skin contact and comfort. However, the limitations of skin breathability issues have not been addressed. In contrast, textiles with embedded electronic components and circuits hold great potential for next-generation wearable electronics, and their breathability and water vapor permeability can lead to better user comfort. Such textiles are often referred to as smart textiles, which are capable of sensing various stimuli, including mechanical, thermal, chemical and biological signals, including ECG, EMG, EEG. In this thesis, we have developed the inkjet-printed PEDOT:PSS/PEO composites that can withstand 50% tensile strain over thousands of

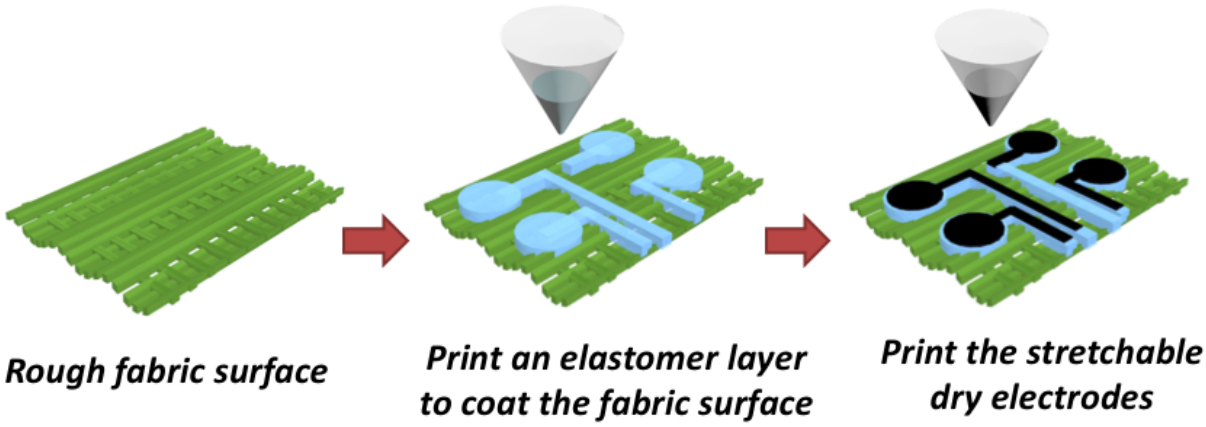

Figure 6.1: Schematics illustrating the process of fabricating stretchable electrodes on fabric surfaces.

cycles. The next step in our research could design electronics on fabrics for health monitoring applications. Our proposed processes start with an elastomer pattern on rough fabric surface and then print stretchable PEDOT:PSS dry electrodes as shown in Figure 6.1. The study will mainly focus on ink rheology optimization on rough fabric surfaces, reduction of electrode-skin contact impedance and material biocompatibility to demonstrate that dry electrodes can be used to record ECG and EMG signals for maternal health imaging, as described in Section 6.2.2.

6.2.2 Multimodal Imaging of Maternal Health

Approximately 10% of pregnant women give birth preterm every year, resulting in high fetal mortality for these premature babies.[233] The mechanisms of initiation and transmission of uterine contractions during preterm labor and delivery remain unknown. The current methods of monitoring uterine contractions with a tocodynamometer or intrauterine pressure catheter can only provide rough information. In order to resolve this issue, Electromyometrial Imaging (EMMI) system developed in the lab of Dr. Yong Wang at Washington University

School of Medicine can non-invasively track three-dimensional electrical signal patterns on the uterus during contractions with a high spatial and temporal resolution. The developed EMMI system can reconstruct uterine surface electrograms, potential maps and isochrone maps as shown in Figure 6.2.[234] The measurement equipment currently used in the EMMI system is manufactured by BioSemi with an integrated 2x4 rigid Ag-AgCl electrode. The measurement of the entire uterine contraction, which consists of 256 unipolar rigid electrodes on the surface of the pregnant woman's abdomen, is not only time-consuming to measure, but also uncomfortable for the patient. Additionally, the rigid electrode patch may detach from the uterine surface during measurement due to bending and twisting of the rigid electrode through body and muscle movement. Another disadvantage is that the high cost of electrodes limits their use in disposables. To overcome these challenges, a low-cost, skin-attachable, self-adhesiveness and stretchable sensor patch that can record high quality electrical signals is urgently needed. Figure 6.3 demonstrated the wireless multi-modal stretchable sensor path with ECG, pressure and piezo sensor. The piezoelectric sensor can generate voltages and currents when they are impacted by mechanical stimuli and act as self-sustaining power sources. Moreover, ECG sensors can collect surface biopotentials, while pressure sensors may be able to record uterine contractions.

6.2.3 Digital Health Monitoring Systems

Digital health monitoring has huge potential for remote health sensing as 20% of US residents live in rural areas but only 9% of physicians work in rural areas.[235] The access to real-time health data is critical for physicians, who can assess and treat patients in the short term. Soft wearable health monitoring device has the potential to be attached to the skin comfortably and provide clinical-grade health monitoring. The sensor patch may integrate multiple units and component devices, not only limited to sensor units, but also batteries,

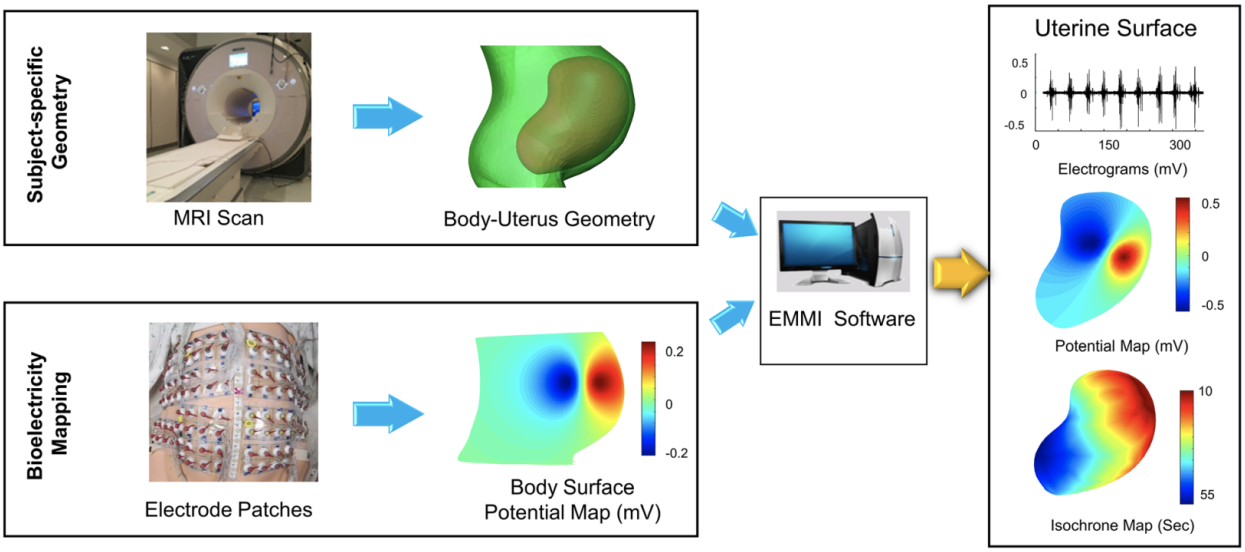

Figure 6.2: Schematic of EMMI system. Top left, a patient-specific bodyuterus geometry is obtained and segmented from an MRI scan while the patient is wearing up to 256 MRI-compatible markers. Lower left, body surface potentials are recorded from up to 256 pin-type unipolar electrode patches placed in positions corresponding to the MRI-compatible markers. Middle, EMMI software combines the two data sets to reconstruct uterine surface (top right) electrograms (electrical waveforms over time at each uterine site) and (middle right) potential maps (electrical activity across the uterus at a single time point). Lower right, activation times can be derived from the electrograms to construct isochrone maps. EMMI software is an in-house developed MATLAB package able to solve the inverse problem. Reprinted from Ref.[234].

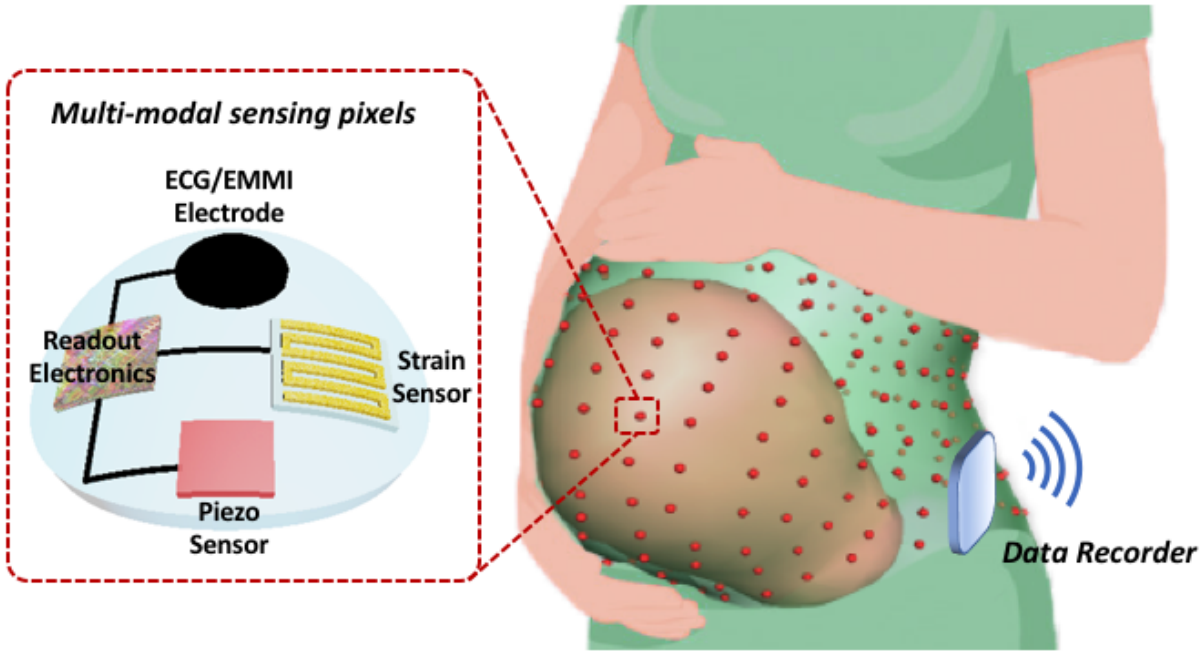

Figure 6.3: Schematic of a multi-modal stretchable sensor patch with ECG, pressure and piezo senor.

wireless communication, wireless charging, and cloud platforms that can process health data in real-time, which provides the following benefits to the personal health. One is that early detection of changes in health status and immediate evaluation of treatment can prevent clinical deterioration. The second is that emergencies can be notified within a short period of time, and alert information can be sent to emergency services to assist patients. Figure 6.4 shows an example of a soft skin-attachable health monitoring system for athletes, workers, and COVID-19 patients that tracks heart activity, respiratory activity, body temperature in real-time, and connects to a cloud platform to provide patient health status.[236] Inspired by this health monitoring system, the next step in research could connect the developed silver nanoparticle pressure sensor and soft porous PEDOT:PSS/PDMS electrodes with

stretchable PEDOT:PSS/PEO conductors to construct a low-cost, skin-attachable, lightweighted wearable sensor patch for high signal quality ECG, EMG, arterial pulse recording systems.

6.2.4 Haptic Sensors for Virtual and Augmented Reality Applications

Emerging technologies for virtual reality and augmented reality have been investigated over the past decade. Nowadays, most virtual reality and augmented reality products use lenses, light sources, and displays to create images. And, with the help of cameras, the system can track and detect objects. In the future, with integrated soft wearable tactile sensors, users can now touch and interact with virtual environments by moving their fingers. Smart wearable gloves can include accelerometers and gyroscopes for motion tracking, pressure sensors for static and dynamic force detection, strain sensors for finger bending motion and gesture detection, biosensors for nerve and muscle activity recording. In addition, the system can also combine machine learning and artificial intelligence to enhance the system's functionality, allowing it to adapt to the behavior of different users. Integrating each sensor into a perception system paves the way for users to participate in virtual worlds in a variety of situations, including medical, educational, and industrial, reducing the barriers between virtual and real environments. Figure 6.5 shows an example of a smart glove with tactile sensors and tactile mechanical stimulators for human-machine interface and virtual reality applications.[237] For the next step in our research, we can fabricate the PEDOT:PSS/PDMS sponge sensor into the shape of a human hand covering the entire skin. The sensor can distinguish between strain or pressure applied to the skin, and can fully capture any hand motion in a low-cost way.

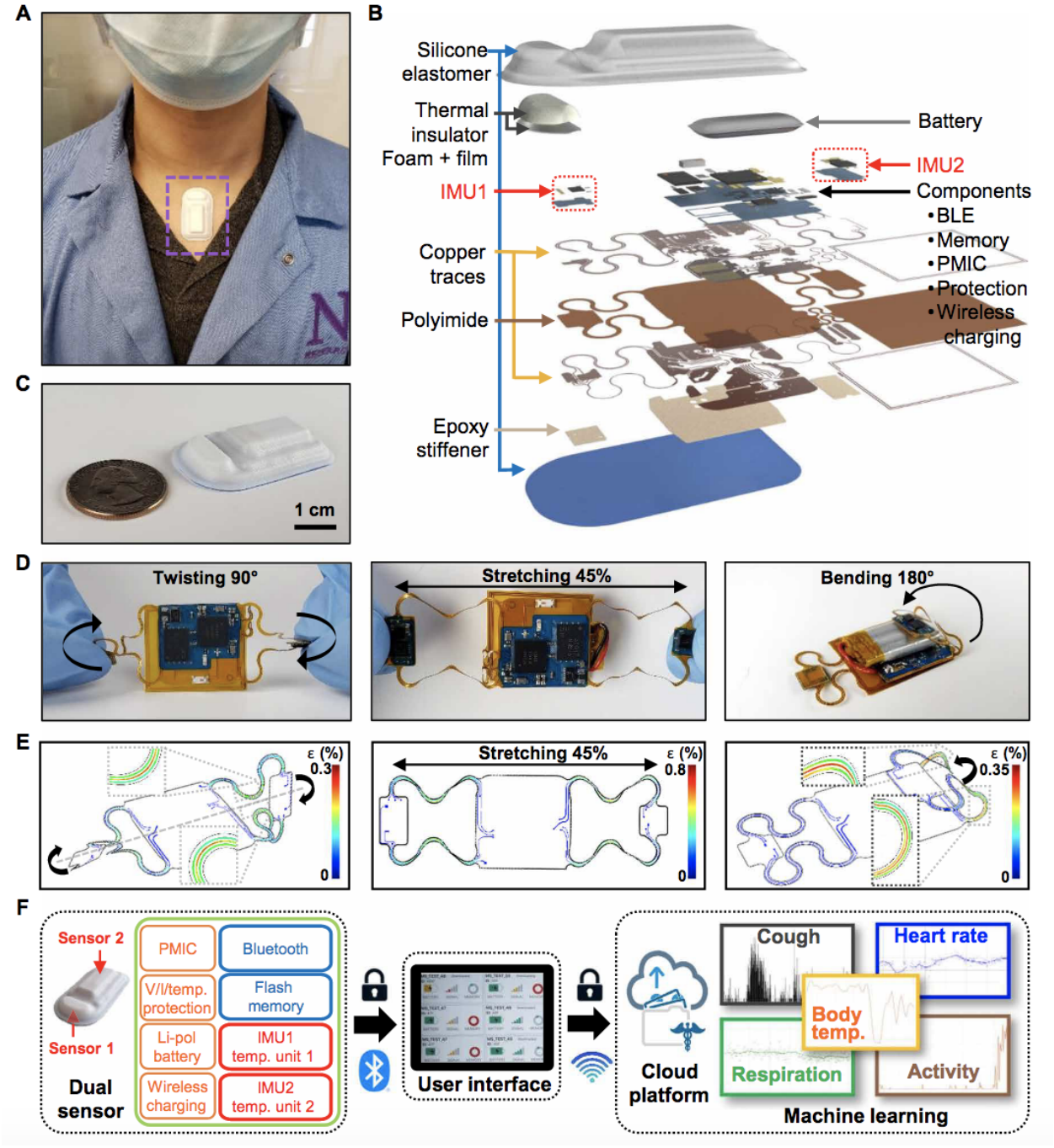

Figure 6.4: (Caption next page.)

Figure 6.4: Images, schematic illustrations, functional flow charts, and mechanical modeling results for a wireless, skin-interfaced device designed for dual MA measurements at the SN and the SM. (A) Image of the device mounted on the base of the neck, positioned with one end at the SN and the other at the SM. (B) Exploded-view schematic illustration of the active components, interconnect schemes, and enclosure architectures. (C) Image of a device next to a U.S. quarter (diameter, 24.26 mm). (D) Images of the device during various mechanical deformations: a twisting angle of 90°(left), 45% uniaxial stretching (middle), and a bending angle of 180° (right). (E) Finite element modeling of the mechanics for the deformations in (D). The contour plots show the maximum principle strains in the metal layer of the serpentine interconnects for twisting (left), stretching (middle), and bending (right). (F) Block diagram of the system operation. A tablet provides an interface for operating the device, wirelessly downloading the data from the device, and transmitting these data to a cloud server through a cellular network. Processing on the cloud platform yields vital signals (HR, respiration, and body temperature) and other metrics of interest (cough count and physical activity). Reprinted from Ref.[236].

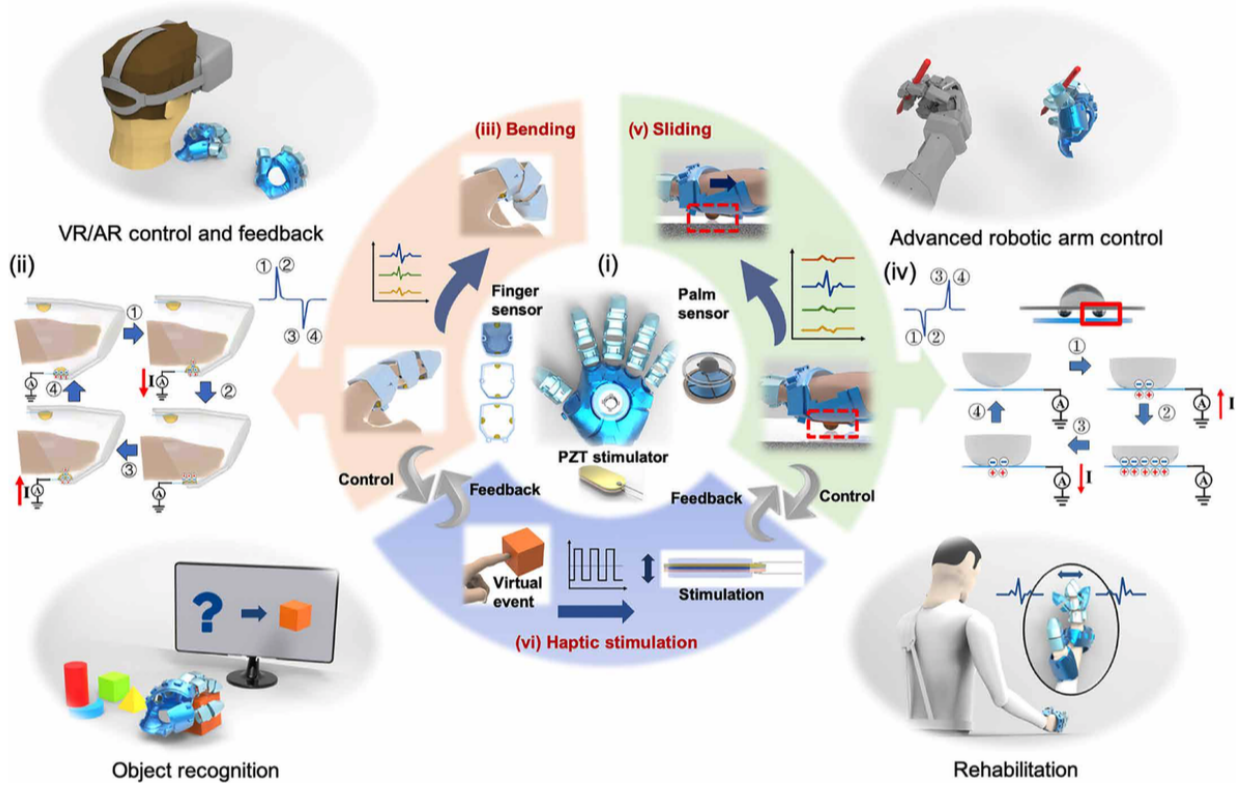

Figure 6.5: Schematics of glove-based HMI for diversified applications. (i) Three major functional units: triboelectric finger sensor and (ii) the working principle for (iii) detecting bending motions, triboelectric palm sensor, and (iv) the working principle for (v) detecting sliding motions, as well as piezoelectric haptic mechanical stimulator for (vi) haptic stimulation. Reprinted from Ref.[237].

References

1. Sekitani, T., Nakajima, H., Maeda, H., Fukushima, T., Aida, T., Hata, K. & Someya, T. Stretchable active-matrix organic light-emitting diode display using printable elastic conductors. *Nature materials* **8,** 494–499 (2009).

2. Mackanic, D. G., Kao, M. & Bao, Z. Enabling deformable and stretchable batteries. *Advanced Energy Materials* **10,** 2001424 (2020).

3. Lee, Y. *et al.* Standalone real-time health monitoring patch based on a stretchable organic optoelectronic system. *Science Advances* **7,** eabg9180 (2021).

4. Lim, S. *et al.* Transparent and stretchable interactive human machine interface based on patterned graphene heterostructures. *Advanced Functional Materials* **25,** 375–383 (2015).

5. Kim, D.-H. *et al.* Stretchable and foldable silicon integrated circuits. *Science* **320,** 507–511 (2008).

6. Chiechi, R. C., Weiss, E. A., Dickey, M. D. & Whitesides, G. M. Eutectic gallium–indium (EGaIn): a moldable liquid metal for electrical characterization of self-assembled monolayers. *Angewandte Chemie International Edition* **47,** 142–144 (2008).

7. Zhu, S., So, J.-H., Mays, R., Desai, S., Barnes, W. R., Pourdeyhimi, B. & Dickey, M. D. Ultrastretchable fibers with metallic conductivity using a liquid metal alloy core. *Advanced Functional Materials* **23,** 2308–2314 (2013).

8. Boley, J. W., White, E. L. & Kramer, R. K. Mechanically sintered gallium–indium nanoparticles. *Advanced Materials* **27,** 2355–2360 (2015).

9. Ladd, C., So, J.-H., Muth, J. & Dickey, M. D. 3D printing of free standing liquid metal microstructures. *Advanced Materials* **25,** 5081–5085 (2013).

10. Lee, P. *et al.* Highly stretchable and highly conductive metal electrode by very long metal nanowire percolation network. *Advanced materials* **24,** 3326–3332 (2012).

11. Dauzon, E. *et al.* Conducting and stretchable PEDOT: PSS electrodes: Role of additives on self-assembly, morphology, and transport. *ACS applied materials & interfaces* **11,** 17570–17582 (2019).

12. Lipomi, D. J., Lee, J. A., Vosgueritchian, M., Tee, B. C.-K., Bolander, J. A. & Bao, Z. Electronic properties of transparent conductive films of PEDOT: PSS on stretchable substrates. *Chemistry of Materials* **24,** 373–382 (2012).

13. Wang, Y. *et al.* A highly stretchable, transparent, and conductive polymer. *Science advances* **3,** e1602076 (2017).

14. Li, P., Sun, K. & Ouyang, J. Stretchable and conductive polymer films prepared by solution blending. *ACS applied materials & interfaces* **7,** 18415–18423 (2015).

15. Kim, D.-H. *et al.* Epidermal electronics. *science* **333,** 838–843 (2011).

16. Zhang, S., Cai, L., Li, W., Miao, J., Wang, T., Yeom, J., Sepúlveda, N. & Wang, C. Fully Printed Silver-Nanoparticle-Based Strain Gauges with Record High Sensitivity. *Advanced Electronic Materials* **3,** 1700067 (2017).

17. Widlund, T., Yang, S., Hsu, Y.-Y. & Lu, N. Stretchability and compliance of free-standing serpentine-shaped ribbons. *International Journal of Solids and Structures* **51,** 4026–4037 (2014).

18. Fan, J. A. *et al.* Fractal design concepts for stretchable electronics. *Nature communications* **5,** 1–8 (2014).

19. Qi, D. *et al.* Suspended wavy graphene microribbons for highly stretchable microsupercapacitors. *Advanced Materials* **27,** 5559–5566 (2015).

20. Qi, D., Zhang, K., Tian, G., Jiang, B. & Huang, Y. Stretchable electronics based on PDMS substrates. *Advanced Materials* **33,** 2003155 (2021).

21. Guo, C. F., Liu, Q., Wang, G., Wang, Y., Shi, Z., Suo, Z., Chu, C.-W. & Ren, Z. Fatigue-free, superstretchable, transparent, and biocompatible metal electrodes. *Proceedings of the National Academy of Sciences* **112,** 12332–12337 (2015).

22. Miyamoto, A. *et al.* Inflammation-free, gas-permeable, lightweight, stretchable on-skin electronics with nanomeshes. *Nature nanotechnology* **12,** 907–913 (2017).

23. Guo, C. F., Sun, T., Liu, Q., Suo, Z. & Ren, Z. Highly stretchable and transparent nanomesh electrodes made by grain boundary lithography. *Nature communications* **5,** 1–8 (2014).

24. Cao, X., Chen, H., Gu, X., Liu, B., Wang, W., Cao, Y., Wu, F. & Zhou, C. Screen printing as a scalable and low-cost approach for rigid and flexible thin-film transistors using separated carbon nanotubes. *ACS nano* **8,** 12769–12776 (2014).

25. Metters, J. P., Kadara, R. O. & Banks, C. E. New directions in screen printed electroanalytical sensors: an overview of recent developments. *Analyst* **136,** 1067–1076 (2011).

26. Zhou, X., Peng, Y., Peng, R., Zeng, X., Zhang, Y.-a. & Guo, T. Fabrication of large-scale microlens arrays based on screen printing for integral imaging 3D display. *ACS Applied Materials & Interfaces* **8,** 24248–24255 (2016).

27. Cao, R. *et al.* Screen-printed washable electronic textiles as self-powered touch/gesture tribo-sensors for intelligent human–machine interaction. *ACS nano* **12,** 5190–5196 (2018).

28. Corea, J. R., Flynn, A. M., Lechêne, B., Scott, G., Reed, G. D., Shin, P. J., Lustig, M. & Arias, A. C. Screen-printed flexible MRI receive coils. *Nature communications* **7,** 1–7 (2016).

29. Hyun, W. J., Secor, E. B., Hersam, M. C., Frisbie, C. D. & Francis, L. F. High-resolution patterning of graphene by screen printing with a silicon stencil for highly flexible printed electronics. *Advanced Materials* **27,** 109–115 (2015).

30. Kordás, K. *et al.* Inkjet printing of electrically conductive patterns of carbon nanotubes. *Small* **2,** 1021–1025 (2006).

31. Finn, D. J., Lotya, M. & Coleman, J. N. Inkjet printing of silver nanowire networks. *ACS applied materials & interfaces* **7,** 9254–9261 (2015).

32. Komuro, N., Takaki, S., Suzuki, K. & Citterio, D. Inkjet printed (bio) chemical sensing devices. *Analytical and bioanalytical chemistry* **405,** 5785–5805 (2013).

33. Mattana, G., Loi, A., Woytasik, M., Barbaro, M., Noël, V. & Piro, B. Inkjet-Printing: A New Fabrication Technology for Organic Transistors. *Advanced Materials Technologies* **2,** 1700063 (2017).

34. Lin, X., Kavalakkatt, J., Lux-Steiner, M. C. & Ennaoui, A. Inkjet-Printed Cu2ZnSn (S, Se) 4 Solar Cells. *Advanced Science* **2,** 1500028 (2015).

35. Kim, S.-Y. *et al.* High-resolution electrohydrodynamic inkjet printing of stretchable metal oxide semiconductor transistors with high performance. *Nanoscale* **8,** 17113–17121 (2016).

36. Maleki, H. & Bertola, V. Recent advances and prospects of inkjet printing in heterogeneous catalysis. *Catalysis Science & Technology* **10,** 3140–3159 (2020).

37. Rajendra Acharya, U., Paul Joseph, K., Kannathal, N., Lim, C. M. & Suri, J. S. Heart rate variability: a review. *Medical and biological engineering and computing* **44,** 1031–1051 (2006).

38. Ashley, E. A. & Niebauer, J. in *Cardiology Explained* (Remedica, 2004).

39. Finsterer, J. EMG-interference pattern analysis. *Journal of Electromyography and Kinesiology* **11,** 231–246 (2001).

40. Acharya, U. R., Sree, S. V., Swapna, G., Martis, R. J. & Suri, J. S. Automated EEG analysis of epilepsy: a review. *Knowledge-Based Systems* **45,** 147–165 (2013).

41. Tao, J. X., Ray, A., Hawes-Ebersole, S. & Ebersole, J. S. Intracranial EEG substrates of scalp EEG interictal spikes. *Epilepsia* **46,** 669–676 (2005).

42. Kim, T., Park, J., Sohn, J., Cho, D. & Jeon, S. Bioinspired, highly stretchable, and conductive dry adhesives based on 1D–2D hybrid carbon nanocomposites for all-in-one ECG electrodes. *ACS nano* **10,** 4770–4778 (2016).

43. Min, H., Jang, S., Kim, D. W., Kim, J., Baik, S., Chun, S. & Pang, C. Highly air/water-permeable hierarchical mesh architectures for stretchable underwater electronic skin patches. *ACS Applied Materials & Interfaces* **12,** 14425–14432 (2020).

44. Ha, T. *et al.* A chest-laminated ultrathin and stretchable E-Tattoo for the measurement of electrocardiogram, seismocardiogram, and cardiac time intervals. *Advanced Science* **6,** 1900290 (2019).

45. Wang, C. *et al.* Monitoring of the central blood pressure waveform via a conformal ultrasonic device. *Nature biomedical engineering* **2,** 687–695 (2018).

46. Choong, C.-L. *et al.* Highly stretchable resistive pressure sensors using a conductive elastomeric composite on a micropyramid array. *Advanced materials* **26,** 3451–3458 (2014).

47. Trung, T. Q., Ramasundaram, S., Hwang, B.-U. & Lee, N.-E. An all-elastomeric transparent and stretchable temperature sensor for body-attachable wearable electronics. *Advanced materials* **28,** 502–509 (2016).

48. Hong, S. Y. *et al.* Stretchable active matrix temperature sensor array of polyaniline nanofibers for electronic skin. *Advanced materials* **28,** 930–935 (2016).

49. Tai, L.-C. *et al.* Methylxanthine drug monitoring with wearable sweat sensors. *Advanced materials* **30,** 1707442 (2018).

50. Song, Y., Min, J., Yu, Y., Wang, H., Yang, Y., Zhang, H. & Gao, W. Wireless battery-free wearable sweat sensor powered by human motion. *Science advances* **6,** eaay9842 (2020).

51. Gao, W. *et al.* Fully integrated wearable sensor arrays for multiplexed in situ perspiration analysis. *Nature* **529,** 509–514 (2016).

52. Liu, Y., Pharr, M. & Salvatore, G. A. Lab-on-skin: a review of flexible and stretchable electronics for wearable health monitoring. *ACS nano* **11,** 9614–9635 (2017).

53. Kwon, Y.-T. *et al.* All-printed nanomembrane wireless bioelectronics using a biocompatible solderable graphene for multimodal human-machine interfaces. *Nature communications* **11,** 1–11 (2020).

54. Pan, L. *et al.* An ultra-sensitive resistive pressure sensor based on hollow-sphere microstructure induced elasticity in conducting polymer film. *Nature communications* **5,** 1–8 (2014).

55. Chhetry, A., Yoon, H. & Park, J. Y. A flexible and highly sensitive capacitive pressure sensor based on conductive fibers with a microporous dielectric for wearable electronics. *Journal of Materials Chemistry C* **5,** 10068–10076 (2017).

56. Chun, J., Lee, K. Y., Kang, C.-Y., Kim, M. W., Kim, S.-W. & Baik, J. M. Embossed hollow hemisphere-based piezoelectric nanogenerator and highly responsive pressure sensor. *Advanced Functional Materials* **24,** 2038–2043 (2014).

57. Lee, K. Y., Yoon, H.-J., Jiang, T., Wen, X., Seung, W., Kim, S.-W. & Wang, Z. L. Fully packaged self-powered triboelectric pressure sensor using hemispheres-array. *Advanced energy materials* **6,** 1502566 (2016).

58. Joo, Y. *et al.* Silver nanowire-embedded PDMS with a multiscale structure for a highly sensitive and robust flexible pressure sensor. *Nanoscale* **7,** 6208–6215 (2015).

59. Chen, M., Luo, W., Xu, Z., Zhang, X., Xie, B., Wang, G. & Han, M. An ultrahigh resolution pressure sensor based on percolative metal nanoparticle arrays. *Nature communications* **10,** 1–9 (2019).

60. Kang, S. *et al.* Highly sensitive pressure sensor based on bioinspired porous structure for real-time tactile sensing. *Advanced Electronic Materials* **2,** 1600356 (2016).

61. Wan, S., Bi, H., Zhou, Y., Xie, X., Su, S., Yin, K. & Sun, L. Graphene oxide as high-performance dielectric materials for capacitive pressure sensors. *Carbon* **114,** 209–216 (2017).

62. Amjadi, M., Turan, M., Clementson, C. P. & Sitti, M. Parallel microcracks-based ultrasensitive and highly stretchable strain sensors. *ACS applied materials & interfaces* **8,** 5618–5626 (2016).

63. Lee, J., Pyo, S., Kwon, D.-S., Jo, E., Kim, W. & Kim, J. Ultrasensitive strain sensor based on separation of overlapped carbon nanotubes. *Small* **15,** 1805120 (2019).

64. Shintake, J., Piskarev, Y., Jeong, S. H. & Floreano, D. Ultrastretchable strain sensors using carbon black-filled elastomer composites and comparison of capacitive versus resistive sensors. *Advanced Materials Technologies* **3,** 1700284 (2018).

65. Atalay, O., Atalay, A., Gafford, J., Wang, H., Wood, R. & Walsh, C. A Highly Stretchable Capacitive-Based Strain Sensor Based on Metal Deposition and Laser Rastering. *Advanced Materials Technologies* **2,** 1700081 (2017).

66. Kim, S.-R., Kim, J.-H. & Park, J.-W. Wearable and transparent capacitive strain sensor with high sensitivity based on patterned Ag nanowire networks. *ACS applied materials & interfaces* **9,** 26407–26416 (2017).

67. Jung, S., Kim, J. H., Kim, J., Choi, S., Lee, J., Park, I., Hyeon, T. & Kim, D.-H. Reverse-micelle-induced porous pressure-sensitive rubber for wearable human–machine interfaces. *Advanced Materials* **26,** 4825–4830 (2014).

68. Mackay, J., Mensah, G. A. & Greenlund, K. *The atlas of heart disease and stroke* (World Health Organization, 2004).

69. Fuchs, F. D. & Whelton, P. K. High blood pressure and cardiovascular disease. *Hypertension* **75,** 285–292 (2020).

70. Lee, J. C., Hudson, S. E. & Tse, E. *Foldable interactive displays* in *Proceedings of the 21st annual ACM symposium on User interface software and technology* (2008), 287–290.

71. Huitema, E. The future of displays is foldable. *Information Display* **28,** 6–10 (2012).

72. Wang, H. *et al.* A highly stretchable liquid metal polymer as reversible transitional insulator and conductor. *Advanced Materials* **31,** 1901337 (2019).

73. Cai, Y. *et al.* Extraordinarily Stretchable All-Carbon Collaborative Nanoarchitectures for Epidermal Sensors. *Advanced Materials* **29,** 1606411 (2017).

74. Lee, S. *et al.* Ag nanowire reinforced highly stretchable conductive fibers for wearable electronics. *Advanced Functional Materials* **25,** 3114–3121 (2015).

75. Jeong, S. H., Zhang, S., Hjort, K., Hilborn, J. & Wu, Z. PDMS-based elastomer tuned soft, stretchable, and sticky for epidermal electronics. *Advanced Materials* **28,** 5830–5836 (2016).

76. Amjadi, M., Yoon, Y. J. & Park, I. Ultra-stretchable and skin-mountable strain sensors using carbon nanotubes–Ecoflex nanocomposites. *Nanotechnology* **26,** 375501 (2015).

77. Li, W., Zhou, Y., Wang, Y., Li, Y., Jiang, L., Ma, J. & Chen, S. Highly stretchable and sensitive SBS/graphene composite fiber for strain sensors. *Macromolecular Materials and Engineering* **305,** 1900736 (2020).

78. Park, G. *et al.* Immunologic and tissue biocompatibility of flexible/stretchable electronics and optoelectronics. *Advanced healthcare materials* **3,** 515–525 (2014).

79. Williams, D. F. On the mechanisms of biocompatibility. *Biomaterials* **29,** 2941–2953 (2008).

80. Pizzoferrato, A., Ciapetti, G., Stea, S., Cenni, E., Arciola, C. R., Granchi, D., *et al.* Cell culture methods for testing biocompatibility. *Clinical materials* **15,** 173–190 (1994).

81. Mukkamala, R., Hahn, J.-O., Inan, O. T., Mestha, L. K., Kim, C.-S., Töreyin, H. & Kyal, S. Toward ubiquitous blood pressure monitoring via pulse transit time: theory and practice. *IEEE Transactions on Biomedical Engineering* **62,** 1879–1901 (2015).

82. Yamamoto, Y., Yamamoto, D., Takada, M., Naito, H., Arie, T., Akita, S. & Takei, K. Efficient skin temperature sensor and stable gel-less sticky ECG sensor for a wearable flexible healthcare patch. *Advanced healthcare materials* **6,** 1700495 (2017).

83. Honda, W., Harada, S., Arie, T., Akita, S. & Takei, K. Wearable, human-interactive, health-monitoring, wireless devices fabricated by macroscale printing techniques. *Advanced Functional Materials* **24,** 3299–3304 (2014).

84. Huang, X. *et al.* Stretchable, wireless sensors and functional substrates for epidermal characterization of sweat. *small* **10,** 3083–3090 (2014).

85. You, I., Kim, B., Park, J., Koh, K., Shin, S., Jung, S. & Jeong, U. Stretchable E-skin apexcardiogram sensor. *Advanced Materials* **28,** 6359–6364 (2016).

86. Schwartz, G., Tee, B. C.-K., Mei, J., Appleton, A. L., Kim, D. H., Wang, H. & Bao, Z. Flexible polymer transistors with high pressure sensitivity for application in electronic skin and health monitoring. *Nature communications* **4,** 1–8 (2013).

87. Nakata, S., Arie, T., Akita, S. & Takei, K. Wearable, flexible, and multifunctional healthcare device with an ISFET chemical sensor for simultaneous sweat pH and skin temperature monitoring. *ACS sensors* **2,** 443–448 (2017).

88. Harada, S., Honda, W., Arie, T., Akita, S. & Takei, K. Fully printed, highly sensitive multifunctional artificial electronic whisker arrays integrated with strain and temperature sensors. *ACS nano* **8,** 3921–3927 (2014).

89. Wang, C., Hwang, D., Yu, Z., Takei, K., Park, J., Chen, T., Ma, B. & Javey, A. User-interactive electronic skin for instantaneous pressure visualization. *Nature materials* **12,** 899–904 (2013).

90. Cao, Y., Figueroa, J., Li, W., Chen, Z., Wang, Z. L. & Sepúlveda, N. Understanding the dynamic response in ferroelectret nanogenerators to enable self-powered tactile systems and human-controlled micro-robots. *Nano Energy* **63,** 103852 (2019).

91. Gao, M., Li, L. & Song, Y. Inkjet printing wearable electronic devices. *Journal of Materials Chemistry C* **5,** 2971–2993 (2017).

92. Huang, Q. & Zhu, Y. Printing conductive nanomaterials for flexible and stretchable electronics: A review of materials, processes, and applications. *Advanced Materials Technologies* **4,** 1800546 (2019).

93. Jason, N. N., Ho, M. D. & Cheng, W. Resistive electronic skin. *Journal of Materials Chemistry C* **5,** 5845–5866 (2017).

94. Zhu, B. *et al.* Hierarchically structured vertical gold nanowire array-based wearable pressure sensors for wireless health monitoring. *ACS applied materials & interfaces* **11,** 29014–29021 (2019).

95. Park, J., Lee, Y., Hong, J., Ha, M., Jung, Y.-D., Lim, H., Kim, S. Y. & Ko, H. Giant tunneling piezoresistance of composite elastomers with interlocked microdome arrays for ultrasensitive and multimodal electronic skins. *ACS nano* **8,** 4689–4697 (2014).

96. Gong, S., Schwalb, W., Wang, Y., Chen, Y., Tang, Y., Si, J., Shirinzadeh, B. & Cheng, W. A wearable and highly sensitive pressure sensor with ultrathin gold nanowires. *Nature communications* **5,** 1–8 (2014).

97. Park, S. *et al.* Stretchable energy-harvesting tactile electronic skin capable of differentiating multiple mechanical stimuli modes. *Advanced Materials* **26,** 7324–7332 (2014).

98. Shi, H., Al-Rubaiai, M., Holbrook, C. M., Miao, J., Pinto, T., Wang, C. & Tan, X. Screen-printed soft capacitive sensors for spatial mapping of both positive and negative pressures. *Advanced Functional Materials* **29,** 1809116 (2019).

99. Park, S.-H., Lee, H. B., Yeon, S. M., Park, J. & Lee, N. K. Flexible and stretchable piezoelectric sensor with thickness-tunable configuration of electrospun nanofiber mat and elastomeric substrates. *ACS applied materials & interfaces* **8,** 24773–24781 (2016).

100. Curry, E. J. *et al.* Biodegradable piezoelectric force sensor. *Proceedings of the National Academy of Sciences* **115,** 909–914 (2018).

101. Kang, D. *et al.* Ultrasensitive mechanical crack-based sensor inspired by the spider sensory system. *Nature* **516,** 222–226 (2014).

102. Choi, Y. W., Kang, D., Pikhitsa, P. V., Lee, T., Kim, S. M., Lee, G., Tahk, D. & Choi, M. Ultra-sensitive pressure sensor based on guided straight mechanical cracks. *Scientific reports* **7,** 1–8 (2017).

103. Yang, T. *et al.* Tactile sensing system based on arrays of graphene woven microfabrics: electromechanical behavior and electronic skin application. *ACS nano* **9,** 10867–10875 (2015).

104. Kong, D., Le, L. T., Li, Y., Zunino, J. L. & Lee, W. Temperature-dependent electrical properties of graphene inkjet-printed on flexible materials. *Langmuir* **28,** 13467–13472 (2012).

105. Cai, L., Zhang, S., Miao, J., Yu, Z. & Wang, C. Fully printed stretchable thin-film transistors and integrated logic circuits. *Acs Nano* **10,** 11459–11468 (2016).

106. Cai, L., Zhang, S., Zhang, Y., Li, J., Miao, J., Wang, Q., Yu, Z. & Wang, C. Direct printing for additive patterning of silver nanowires for stretchable sensor and display applications. *Advanced Materials Technologies* **3,** 1700232 (2018).

107. Andersson, H., Manuilskiy, A., Unander, T., Lidenmark, C., Forsberg, S. & Nilsson, H.-E. Inkjet printed silver nanoparticle humidity sensor with memory effect on paper. *IEEE Sensors Journal* **12,** 1901–1905 (2011).

108. Molina-Lopez, F., Briand, D. & De Rooij, N. All additive inkjet printed humidity sensors on plastic substrate. *Sensors and Actuators B: Chemical* **166,** 212–222 (2012).

109. Ando, B. & Baglio, S. All-inkjet printed strain sensors. *IEEE Sensors Journal* **13,** 4874–4879 (2013).

110. Michelis, F., Bodelot, L., Bonnassieux, Y. & Lebental, B. Highly reproducible, hysteresis-free, flexible strain sensors by inkjet printing of carbon nanotubes. *Carbon* **95,** 1020–1026 (2015).

111. Vuorinen, T., Niittynen, J., Kankkunen, T., Kraft, T. M. & Mäntysalo, M. Inkjet-printed graphene/PEDOT: PSS temperature sensors on a skin-conformable polyurethane substrate. *Scientific reports* **6,** 1–8 (2016).

112. Jiang, J. *et al.* Fabrication of transparent multilayer circuits by inkjet printing. *Advanced Materials* **28,** 1420–1426 (2016).

113. Park, J. Y., Yoo, S. J., Lee, E.-J., Lee, D. H., Kim, J. Y. & Lee, S.-H. Increased poly (dimethylsiloxane) stiffness improves viability and morphology of mouse fibroblast cells. *BioChip Journal* **4,** 230–236 (2010).

114. Mannsfeld, S. C. *et al.* Highly sensitive flexible pressure sensors with microstructured rubber dielectric layers. *Nature materials* **9,** 859–864 (2010).

115. Nichols, W. W. Clinical measurement of arterial stiffness obtained from noninvasive pressure waveforms. *American journal of hypertension* **18,** 3S–10S (2005).

116. Bi, C., Chen, B., Wei, H., DeLuca, S. & Huang, J. Efficient flexible solar cell based on composition-tailored hybrid perovskite. *Advanced Materials* **29,** 1605900 (2017).

117. Takei, K., Honda, W., Harada, S., Arie, T. & Akita, S. Toward flexible and wearable human-interactive health-monitoring devices. *Advanced healthcare materials* **4,** 487–500 (2015).

118. Khan, Y. *et al.* A flexible organic reflectance oximeter array. *Proceedings of the National Academy of Sciences* **115,** E11015–E11024 (2018).

119. Choi, M., Park, Y. J., Sharma, B. K., Bae, S.-R., Kim, S. Y. & Ahn, J.-H. Flexible active-matrix organic light-emitting diode display enabled by MoS2 thin-film transistor. *Science advances* **4,** eaas8721 (2018).

120. Yu, M., Wan, H., Cai, L., Miao, J., Zhang, S. & Wang, C. Fully printed flexible dual-gate carbon nanotube thin-film transistors with tunable ambipolar characteristics for complementary logic circuits. *ACS nano* **12,** 11572–11578 (2018).

121. Wan, H., Cao, Y., Lo, L.-W., Zhao, J., Sepulveda, N. & Wang, C. Flexible carbon nanotube synaptic transistor for neurological electronic skin applications. *ACS nano* **14,** 10402–10412 (2020).

122. Rao, Z., Ershad, F., Almasri, A., Gonzalez, L., Wu, X. & Yu, C. Soft electronics for the skin: from health monitors to human–machine interfaces. *Advanced Materials Technologies* **5,** 2000233 (2020).

123. Jeong, Y. R. *et al.* A skin-attachable, stretchable integrated system based on liquid GaInSn for wireless human motion monitoring with multi-site sensing capabilities. *NPG Asia Materials* **9,** e443–e443 (2017).

124. Chortos, A. & Bao, Z. Skin-inspired electronic devices. *Materials Today* **17,** 321–331 (2014).

125. Cotur, Y., Kasimatis, M., Kaisti, M., Olenik, S., Georgiou, C. & Güder, F. Stretchable composite acoustic transducer for wearable monitoring of vital signs. *Advanced functional materials* **30,** 1910288 (2020).

126. Bade, S. G. R. *et al.* Stretchable Light-Emitting Diodes with Organometal-Halide-Perovskite–Polymer Composite Emitters. *Advanced Materials* **29,** 1607053 (2017).

127. Pu, X. *et al.* Ultrastretchable, transparent triboelectric nanogenerator as electronic skin for biomechanical energy harvesting and tactile sensing. *Science advances* **3,** e1700015 (2017).

128. Rogers, J. A., Someya, T. & Huang, Y. Materials and mechanics for stretchable electronics. *science* **327,** 1603–1607 (2010).

129. Lo, L.-W., Shi, H., Wan, H., Xu, Z., Tan, X. & Wang, C. Inkjet-printed soft resistive pressure sensor patch for wearable electronics applications. *Advanced Materials Technologies* **5,** 1900717 (2020).

130. Tang, J. *et al.* Highly stretchable electrodes on wrinkled polydimethylsiloxane substrates. *Scientific reports* **5,** 1–9 (2015).

131. Khang, D.-Y., Rogers, J. A. & Lee, H. H. Mechanical buckling: mechanics, metrology, and stretchable electronics. *Advanced Functional Materials* **19,** 1526–1536 (2009).

132. Sun, Y., Kumar, V., Adesida, I. & Rogers, J. A. Buckled and wavy ribbons of GaAs for high-performance electronics on elastomeric substrates. *Advanced Materials* **18,** 2857–2862 (2006).

133. Oh, J. Y., Jun, G. H., Jin, S., Ryu, H. J. & Hong, S. H. Enhanced electrical networks of stretchable conductors with small fraction of carbon nanotube/graphene hybrid fillers. *ACS applied materials & interfaces* **8,** 3319–3325 (2016).

134. Larmagnac, A., Eggenberger, S., Janossy, H. & Vörös, J. Stretchable electronics based on Ag-PDMS composites. *Scientific reports* **4,** 1–7 (2014).

135. Kim, Y. *et al.* Stretchable nanoparticle conductors with self-organized conductive pathways. *Nature* **500,** 59–63 (2013).

136. Hu, W., Niu, X., Li, L., Yun, S., Yu, Z. & Pei, Q. Intrinsically stretchable transparent electrodes based on silver-nanowire–crosslinked-polyacrylate composites. *Nanotechnology* **23,** 344002 (2012).

137. Chen, Y., Carmichael, R. S. & Carmichael, T. B. Patterned, flexible, and stretchable silver nanowire/polymer composite films as transparent conductive electrodes. *ACS applied materials & interfaces* **11,** 31210–31219 (2019).

138. Tseng, Y.-T., Lin, Y.-C., Shih, C.-C., Hsieh, H.-C., Lee, W.-Y., Chiu, Y.-C. & Chen, W.-C. Morphology and properties of PEDOT: PSS/soft polymer blends through

hydrogen bonding interaction and their pressure sensor application. *Journal of Materials Chemistry C* **8,** 6013–6024 (2020).

139. Dauzon, E. *et al.* Stretchable and transparent conductive PEDOT: PSS-based electrodes for organic photovoltaics and strain sensors applications. *Advanced Functional Materials* **30,** 2001251 (2020).

140. Lee, J. H. *et al.* Highly conductive, stretchable, and transparent PEDOT: PSS electrodes fabricated with triblock copolymer additives and acid treatment. *ACS applied materials & interfaces* **10,** 28027–28035 (2018).

141. Vosgueritchian, M., Lipomi, D. J. & Bao, Z. Highly conductive and transparent PEDOT: PSS films with a fluorosurfactant for stretchable and flexible transparent electrodes. *Advanced functional materials* **22,** 421–428 (2012).

142. Jung, S., Sou, A., Gili, E. & Sirringhaus, H. Inkjet-printed resistors with a wide resistance range for printed read-only memory applications. *Organic electronics* **14,** 699–702 (2013).

143. Hoath, S. D. *et al.* Oscillations of aqueous PEDOT: PSS fluid droplets and the properties of complex fluids in drop-on-demand inkjet printing. *Journal of Non-Newtonian Fluid Mechanics* **223,** 28–36 (2015).

144. Basak, I. *et al.* Inkjet printing of PEDOT: PSS based conductive patterns for 3D forming applications. *Polymers* **12,** 2915 (2020).

145. Li, L., Pan, L., Ma, Z., Yan, K., Cheng, W., Shi, Y. & Yu, G. All inkjet-printed amperometric multiplexed biosensors based on nanostructured conductive hydrogel electrodes. *Nano letters* **18,** 3322–3327 (2018).

146. Huang, T.-T. & Wu, W. Inkjet-printed wearable nanosystems for self-powered technologies. *Advanced Materials Interfaces* **7,** 2000015 (2020).

147. Sico, G., Montanino, M., De Girolamo Del Mauro, A. & Minarini, C. Improving the gravure printed PEDOT: PSS electrode by gravure printing DMSO post-treatment. *Journal of Materials Science: Materials in Electronics* **29,** 11730–11737 (2018).

148. Sico, G., Montanino, M., Del Mauro, A. D. G., Imparato, A., Nobile, G. & Minarini, C. Effects of the ink concentration on multi-layer gravure-printed PEDOT: PSS. *Organic Electronics* **28,** 257–262 (2016).

149. Fan, X. *et al.* PEDOT: PSS for flexible and stretchable electronics: modifications, strategies, and applications. *Advanced Science* **6,** 1900813 (2019).

150. Carrasco-Torres, G., Valdés-Madrigal, M. A., Vásquez-Garzón, V. R., Baltiérrez-Hoyos, R., la Cruz-Burelo, D., Román-Doval, R., Valencia-Lazcano, A. A., *et al.* Effect of silk fibroin on cell viability in electrospun scaffolds of polyethylene oxide. *Polymers* **11,** 451 (2019).

151. Vomero, M. *et al.* Highly stable glassy carbon interfaces for long-term neural stimulation and low-noise recording of brain activity. *Scientific reports* **7,** 1–14 (2017).

152. Jabbar, F., Soomro, A. M., Lee, J.-w., Ali, M., Kim, Y. S., Lee, S.-h. & Choi, K. H. Robust Fluidic Biocompatible Strain Sensor Based on PEDOT: PSS/CNT Composite for Human-wearable and High-end Robotic Applications. *Sensors and Materials* **32,** 4077–4093 (2020).

153. Monteiro A, I., Kollmetz, T., Musson, D. S., McGlashan, S. R. & Malmström, J. Polystyrene-block-polyethylene oxide thin films: In vitro cytocompatibility and protein adsorption testing. *Biointerphases* **15,** 011003 (2020).

154. Yuk, H., Lu, B., Lin, S., Qu, K., Xu, J., Luo, J. & Zhao, X. 3D printing of conducting polymers. *Nature communications* **11,** 1–8 (2020).

155. Hoath, S. D., Jung, S., Hsiao, W.-K. & Hutchings, I. M. How PEDOT: PSS solutions produce satellite-free inkjets. *Organic Electronics* **13,** 3259–3262 (2012).

156. Gemeiner, P., Peřinka, N., Švorc, L., Hatala, M., Gál, L., Belovičová, M., Syrov, T. & Mikula, M. Pt–free counter electrodes based on modified screen–printed PEDOT: PSS catalytic layers for dye–sensitized solar cells. *Materials Science in Semiconductor Processing* **66,** 162–169 (2017).

157. Van Driessche, I. *et al.* Chemical solution deposition using ink-jet printing for YBCO coated conductors. *Superconductor Science and Technology* **25,** 065017 (2012).

158. Derby, B. Inkjet printing of functional and structural materials: fluid property requirements, feature stability, and resolution. *Annual Review of Materials Research* **40,** 395–414 (2010).

159. Yang, L. *et al.* Determination of dynamic surface tension and viscosity of non-Newtonian fluids from drop oscillations. *Physics of Fluids* **26,** 113103 (2014).

160. Dybowska-Sarapuk, L., Kielbasinski, K., Arazna, A., Futera, K., Skalski, A., Janczak, D., Sloma, M. & Jakubowska, M. Efficient inkjet printing of graphene-based elements: Influence of dispersing agent on ink viscosity. *Nanomaterials* **8,** 602 (2018).

161. Ouyang, J., Xu, Q., Chu, C.-W., Yang, Y., Li, G. & Shinar, J. On the mechanism of conductivity enhancement in poly (3, 4-ethylenedioxythiophene): poly (styrene sulfonate) film through solvent treatment. *Polymer* **45,** 8443–8450 (2004).

162. Wijeratne, K., Ail, U., Brooke, R., Vagin, M., Liu, X., Fahlman, M. & Crispin, X. Bulk electronic transport impacts on electron transfer at conducting polymer electrode–electrolyte interfaces. *Proceedings of the National Academy of Sciences* **115,** 11899–11904 (2018).

163. Wang, Y., Song, R., Li, Y. & Shen, J. Understanding tapping-mode atomic force microscopy data on the surface of soft block copolymers. *Surface science* **530,** 136–148 (2003).

164. Kayser, L. V. & Lipomi, D. J. Stretchable conductive polymers and composites based on PEDOT and PEDOT: PSS. *Advanced Materials* **31,** 1806133 (2019).

165. Luo, R., Li, H., Du, B., Zhou, S. & Zhu, Y. A simple strategy for high stretchable, flexible and conductive polymer films based on PEDOT: PSS-PDMS blends. *Organic Electronics* **76,** 105451 (2020).

166. Taroni, P. J. *et al.* Toward stretchable self-powered sensors based on the thermoelectric response of PEDOT: PSS/polyurethane blends. *Advanced Functional Materials* **28,** 1704285 (2018).

167. Ratna, D., Divekar, S., Samui, A., Chakraborty, B. & Banthia, A. Poly (ethylene oxide)/clay nanocomposite: thermomechanical properties and morphology. *Polymer* **47,** 4068–4074 (2006).

168. Wang, T., Qi, Y., Xu, J., Hu, X. & Chen, P. Effects of poly (ethylene glycol) on electrical conductivity of poly (3, 4-ethylenedioxythiophene)–poly (styrenesulfonic acid) film. *Applied surface science* **250,** 188–194 (2005).

169. Yuk, H., Lu, B. & Zhao, X. Hydrogel bioelectronics. *Chemical Society Reviews* **48,** 1642–1667 (2019).

170. Tamura, T., Maeda, Y., Sekine, M. & Yoshida, M. Wearable photoplethysmographic sensors—past and present. *Electronics* **3,** 282–302 (2014).

171. Klabunde, R. E. Cardiac electrophysiology: normal and ischemic ionic currents and the ECG. *Advances in physiology education* **41,** 29–37 (2017).

172. Luz, E. J. d. S., Schwartz, W. R., Cámara-Chávez, G. & Menotti, D. ECG-based heartbeat classification for arrhythmia detection: A survey. *Computer methods and programs in biomedicine* **127,** 144–164 (2016).

173. Birnbaum, Y. & Drew, B. J. The electrocardiogram in ST elevation acute myocardial infarction: correlation with coronary anatomy and prognosis. *Postgraduate medical journal* **79,** 490–504 (2003).

174. Zamarayeva, A. M. *et al.* Flexible and stretchable power sources for wearable electronics. *Science advances* **3,** e1602051 (2017).

175. Hua, Q., Sun, J., Liu, H., Bao, R., Yu, R., Zhai, J., Pan, C. & Wang, Z. L. Skin-inspired highly stretchable and conformable matrix networks for multifunctional sensing. *Nature communications* **9,** 1–11 (2018).

176. Wang, Y., Lee, S., Yokota, T., Wang, H., Jiang, Z., Wang, J., Koizumi, M. & Someya, T. A durable nanomesh on-skin strain gauge for natural skin motion monitoring with minimum mechanical constraints. *Science advances* **6,** eabb7043 (2020).

177. Wang, C. *et al.* Continuous monitoring of deep-tissue haemodynamics with stretchable ultrasonic phased arrays. *Nature Biomedical Engineering* **5,** 749–758 (2021).

178. Oh, Y. S. *et al.* Battery-free, wireless soft sensors for continuous multi-site measurements of pressure and temperature from patients at risk for pressure injuries. *Nature communications* **12,** 1–16 (2021).

179. Jiang, Y. *et al.* Topological supramolecular network enabled high-conductivity, stretchable organic bioelectronics. *Science* **375,** 1411–1417 (2022).

180. Choi, Y. S. *et al.* Fully implantable and bioresorbable cardiac pacemakers without leads or batteries. *Nature biotechnology* **39,** 1228–1238 (2021).

181. Lu, W. *et al.* Wireless, implantable catheter-type oximeter designed for cardiac oxygen saturation. *Science advances* **7,** eabe0579 (2021).

182. Yu, Y. *et al.* Biofuel-powered soft electronic skin with multiplexed and wireless sensing for human-machine interfaces. *Science robotics* (2020).

183. Jeong, J.-W. *et al.* Materials and optimized designs for human-machine interfaces via epidermal electronics. *Advanced Materials* **25,** 6839–6846 (2013).

184. Ettinger, P. O., Wu, C. F., De La Cruz Jr, C., Weisse, A. B., Ahmed, S. S. & Regan, T. J. Arrhythmias and the "Holiday Heart": alcoholassociated cardiac rhythm disorders. *American heart journal* **95,** 555–562 (1978).

185. Diercks, D. B., Shumaik, G. M., Harrigan, R. A., Brady, W. J. & Chan, T. C. Electrocardiographic manifestations: electrolyte abnormalities. *The Journal of emergency medicine* **27,** 153–160 (2004).

186. Mallik, A. & Weir, A. Nerve conduction studies: essentials and pitfalls in practice. *Journal of Neurology, Neurosurgery & Psychiatry* **76,** ii23–ii31 (2005).

187. Sakakibara, R., Uchiyama, T., Yamanishi, T. & Kishi, M. Sphincter EMG as a diagnostic tool in autonomic disorders. *Clinical Autonomic Research* **19,** 20–31 (2009).

188. Buckingham, S. C., Campbell, S. L., Haas, B. R., Montana, V., Robel, S., Ogunrinu, T. & Sontheimer, H. Glutamate release by primary brain tumors induces epileptic activity. *Nature medicine* **17,** 1269–1274 (2011).

189. Binnie, C. & Prior, P. Electroencephalography. *Journal of Neurology, Neurosurgery & Psychiatry* **57,** 1308–1319 (1994).

190. Han, J.-S., Bien, Z. Z., Kim, D.-J., Lee, H.-E. & Kim, J.-S. *Human-machine interface for wheelchair control with EMG and its evaluation* in *Proceedings of the 25th annual international conference of the ieee engineering in medicine and biology society (ieee cat. no. 03ch37439)* **2** (2003), 1602–1605.

191. Wagner, F. B. *et al.* Targeted neurotechnology restores walking in humans with spinal cord injury. *Nature* **563,** 65–71 (2018).

192. Yin, Y. H., Fan, Y. J. & Xu, L. D. EMG and EPP-integrated human–machine interface between the paralyzed and rehabilitation exoskeleton. *IEEE Transactions on Information Technology in Biomedicine* **16,** 542–549 (2012).

193. Norton, J. J. *et al.* Soft, curved electrode systems capable of integration on the auricle as a persistent brain–computer interface. *Proceedings of the National Academy of Sciences* **112,** 3920–3925 (2015).

194. Zhang, L. *et al.* Fully organic compliant dry electrodes self-adhesive to skin for long-term motion-robust epidermal biopotential monitoring. *Nature communications* **11,** 1–13 (2020).

195. Fang, Y., Li, Y., Wang, X., Zhou, Z., Zhang, K., Zhou, J. & Hu, B. Cryo-Transferred Ultrathin and Stretchable Epidermal Electrodes. *Small* **16,** 2000450 (2020).

196. Zhou, W., Yao, S., Wang, H., Du, Q., Ma, Y. & Zhu, Y. Gas-permeable, ultrathin, stretchable epidermal electronics with porous electrodes. *ACS nano* **14,** 5798–5805 (2020).

197. Hou, Y., Li, Z., Wang, Z. & Yu, H. Miura-ori structured flexible microneedle array electrode for biosignal recording. *Microsystems & nanoengineering* **7,** 1–8 (2021).

198. Krieger, K. J., Liegey, J., Cahill, E. M., Bertollo, N., Lowery, M. M. & O'Cearbhaill, E. D. Development and Evaluation of 3D-Printed Dry Microneedle Electrodes for Surface Electromyography. *Advanced Materials Technologies* **5,** 2000518 (2020).

199. Sullivan, S. P., Murthy, N. & Prausnitz, M. R. Minimally invasive protein delivery with rapidly dissolving polymer microneedles. *Advanced materials* **20,** 933–938 (2008).

200. Stauffer, F. *et al.* Skin conformal polymer electrodes for clinical ECG and EEG recordings. *Advanced healthcare materials* **7,** 1700994 (2018).

201. Yun, I. *et al.* Stable bioelectric signal acquisition using an enlarged surface-area flexible skin electrode. *ACS Applied Electronic Materials* **3,** 1842–1851 (2021).

202. Matsui, T. & Amagai, M. Dissecting the formation, structure and barrier function of the stratum corneum. *International immunology* **27,** 269–280 (2015).

203. Melissen, H. Densest packings of eleven congruent circles in a circle. *Geometriae Dedicata* **50,** 15–25 (1994).

204. Lucovnik, M., Kuon, R. J., Chambliss, L. R., Maner, W. L., SHI, S.-Q., Shi, L., Balducci, J. & Garfield, R. E. Use of uterine electromyography to diagnose term and preterm labor. *Acta obstetricia et gynecologica Scandinavica* **90,** 150–157 (2011).

205. Garfield, R. E. & Maner, W. L. *Physiology and electrical activity of uterine contractions* in *Seminars in cell & developmental biology* **18** (2007), 289–295.

206. Wu, W. *et al.* Noninvasive high-resolution electromyometrial imaging of uterine contractions in a translational sheep model. *Science translational medicine* **11,** eaau1428 (2019).

207. Wang, H. *et al.* Accuracy of electromyometrial imaging of uterine contractions in clinical environment. *Computers in biology and medicine* **116,** 103543 (2020).

208. Atalay, A., Sanchez, V., Atalay, O., Vogt, D. M., Haufe, F., Wood, R. J. & Walsh, C. J. Batch fabrication of customizable silicone-textile composite capacitive strain sensors for human motion tracking. *Advanced Materials Technologies* **2,** 1700136 (2017).

209. Li, S., Peele, B. N., Larson, C. M., Zhao, H. & Shepherd, R. F. A stretchable multicolor display and touch interface using photopatterning and transfer printing. *Advanced Materials* **28,** 9770–9775 (2016).

210. Cho, D., Park, J., Kim, J., Kim, T., Kim, J., Park, I. & Jeon, S. Three-dimensional continuous conductive nanostructure for highly sensitive and stretchable strain sensor. *ACS Applied Materials & Interfaces* **9,** 17369–17378 (2017).

211. Jin, H., Nayeem, M. O. G., Lee, S., Matsuhisa, N., Inoue, D., Yokota, T., Hashizume, D. & Someya, T. Highly durable nanofiber-reinforced elastic conductors for skin-tight electronic textiles. *ACS nano* **13,** 7905–7912 (2019).

212. Ding, Y., Xu, T., Onyilagha, O., Fong, H. & Zhu, Z. Recent advances in flexible and wearable pressure sensors based on piezoresistive 3D monolithic conductive sponges. *ACS applied materials & interfaces* **11,** 6685–6704 (2019).

213. Li, W. *et al.* A porous and air gap elastomeric dielectric layer for wearable capacitive pressure sensor with high sensitivity and a wide detection range. *Journal of Materials Chemistry C* **8,** 11468–11476 (2020).

214. Li, W., Jin, X., Han, X., Li, Y., Wang, W., Lin, T. & Zhu, Z. Synergy of porous structure and microstructure in piezoresistive material for high-performance and flexible pressure sensors. *ACS Applied Materials & Interfaces* **13,** 19211–19220 (2021).

215. Sun, P., Wu, D. & Liu, C. High-sensitivity tactile sensor based on Ti2C-PDMS sponge for wireless human–computer interaction. *Nanotechnology* **32,** 295506 (2021).

216. Yang, J., Luo, S., Zhou, X., Li, J., Fu, J., Yang, W. & Wei, D. Flexible, tunable, and ultrasensitive capacitive pressure sensor with microconformal graphene electrodes. *ACS applied materials & interfaces* **11,** 14997–15006 (2019).

217. Lee, J., Kim, S., Lee, J., Yang, D., Park, B. C., Ryu, S. & Park, I. A stretchable strain sensor based on a metal nanoparticle thin film for human motion detection. *Nanoscale* **6,** 11932–11939 (2014).

218. Qin, Y. *et al.* Lightweight, superelastic, and mechanically flexible graphene/polyimide nanocomposite foam for strain sensor application. *ACS nano* **9,** 8933–8941 (2015).

219. Amjadi, M., Pichitpajongkit, A., Lee, S., Ryu, S. & Park, I. Highly stretchable and sensitive strain sensor based on silver nanowire–elastomer nanocomposite. *ACS nano* **8,** 5154–5163 (2014).

220. Yamamoto, D., Nakata, S., Kanao, K., Arie, T., Akita, S. & Takei, K. A planar, multi-sensing wearable health monitoring device integrated with acceleration, temperature, and electrocardiogram sensors. *Advanced Materials Technologies* **2,** 1700057 (2017).

221. Ho, D. H., Sun, Q., Kim, S. Y., Han, J. T., Kim, D. H. & Cho, J. H. Stretchable and multimodal all graphene electronic skin. *Advanced Materials* **28,** 2601–2608 (2016).

222. Boutry, C. M. *et al.* A stretchable and biodegradable strain and pressure sensor for orthopaedic application. *Nature Electronics* **1,** 314–321 (2018).

223. Peng, S., Wu, S., Yu, Y., Xia, B., Lovell, N. H. & Wang, C. H. Multimodal capacitive and piezoresistive sensor for simultaneous measurement of multiple forces. *ACS Applied Materials & Interfaces* **12,** 22179–22190 (2020).

224. Kim, N., Kee, S., Lee, S. H., Lee, B. H., Kahng, Y. H., Jo, Y.-R., Kim, B.-J. & Lee, K. Highly conductive PEDOT: PSS nanofibrils induced by solution-processed crystallization. *Advanced materials* **26,** 2268–2272 (2014).

225. Pang, C., Lee, G.-Y., Kim, T.-i., Kim, S. M., Kim, H. N., Ahn, S.-H. & Suh, K.-Y. A flexible and highly sensitive strain-gauge sensor using reversible interlocking of nanofibres. *Nature materials* **11,** 795–801 (2012).

226. Wang, Y., Wu, H., Xu, L., Zhang, H., Yang, Y. & Wang, Z. L. Hierarchically patterned self-powered sensors for multifunctional tactile sensing. *Science advances* **6,** eabb9083 (2020).

227. Farcich, N. J., Salonen, J. & Asbeck, P. M. Single-length method used to determine the dielectric constant of polydimethylsiloxane. *IEEE Transactions on Microwave Theory and techniques* **56,** 2963–2971 (2008).

228. Meyer, J., Arnrich, B., Schumm, J. & Troster, G. Design and modeling of a textile pressure sensor for sitting posture classification. *IEEE Sensors Journal* **10,** 1391–1398 (2010).

229. Vitoratos, E., Sakkopoulos, S., Dalas, E., Paliatsas, N., Karageorgopoulos, D., Petraki, F., Kennou, S. & Choulis, S. A. Thermal degradation mechanisms of PEDOT: PSS. *Organic Electronics* **10,** 61–66 (2009).

230. Zhou, J., Anjum, D. H., Chen, L., Xu, X., Ventura, I. A., Jiang, L. & Lubineau, G. The temperature-dependent microstructure of PEDOT/PSS films: insights from morphological, mechanical and electrical analyses. *Journal of Materials Chemistry C* **2,** 9903–9910 (2014).

231. Pradhan, S. & Yadavalli, V. K. Photolithographically Printed Flexible Silk/PEDOT: PSS Temperature Sensors. *ACS Applied Electronic Materials* **3,** 21–29 (2020).

232. Wang, Y.-F. *et al.* Fully printed PEDOT: PSS-based temperature sensor with high humidity stability for wireless healthcare monitoring. *Scientific reports* **10,** 1–8 (2020).

233. Torchin, H. & Ancel, P. Epidemiology and risk factors of preterm birth. *Journal de gynecologie, obstetrique et biologie de la reproduction* **45,** 1213–1230 (2016).

234. Wang, H. & Wang, Y. Spatial-dependent regularization to solve the inverse problem in electromyometrial imaging. *Medical & biological engineering & computing* **58,** 1651–1665 (2020).

235. Of Health, U. D., Services, H., *et al.* Healthcare disparities in rural areas: Selected findings from the 2004 national health care disparities report. *US Department of Health and Human Services, Agency for Healthcare Research and Quality* (2004).

236. Jeong, H. *et al.* Differential cardiopulmonary monitoring system for artifact-canceled physiological tracking of athletes, workers, and COVID-19 patients. *Science advances* **7,** eabg3092 (2021).

237. Zhu, M., Sun, Z., Zhang, Z., Shi, Q., He, T., Liu, H., Chen, T. & Lee, C. Haptic-feedback smart glove as a creative human-machine interface (HMI) for virtual/augmented reality applications. *Science Advances* **6,** eaaz8693 (2020).